# Subcycle optical nanoscopy with atomic-scale resolution


Dissertation
zur Erlangung des Doktorgrades der Naturwissenschaften
(Dr. rer. nat.)
der Fakultät für Physik der Universität Regensburg

vorgelegt von
Johannes Martin Hayes
aus Pfaffenhofen a. d. Ilm
im Jahr 2025

Das Promotionsgesuch wurde eingereicht am: 30.04.2025.

Die Arbeit wurde angeleitet von: Prof. Dr. Rupert Huber.

| | | |
|---|---|---|
| Prüfungsausschuss: | Vorsitzender: | Prof. Dr. Vladimir Braun |
| | 1. Gutachter: | Prof. Dr. Rupert Huber |
| | 2. Gutachter: | Prof. Dr. Jascha Repp |
| | weiterer Prüfer: | Prof. Dr. Ulrich Höfer |

# Contents

Chapter 1

# Introduction

*All our knowledge has its origins in our perceptions.*

— Leonardo da Vinci

Optical microscopy has revolutionised natural sciences for centuries. It has been at the heart of fundamental discoveries, enabling the visualisation of objects too small for human perception. A pivotal moment in the 17th century was the publication of *Micrographia* by *Robert Hooke* [Hoo65] – the first illustrated book on microscopy – providing unprecedented insights into the microscopic world. Hooke famously discovered biological cells when he observed that cork consists of tiny chambers. His work also contained the first published image of a microorganism, describing mould as being made of what he called *microscopical mushrooms*. Around the same time, *Antoni van Leeuwenhoek* made equally groundbreaking discoveries [Ges04]. He was the first to describe red blood cells, and observed that fertilisation involved sperm entering the egg cell. Perhaps his most revolutionary discovery was that of living bacteria, which he called *animalcules*.

Being able to see directly what biological cells consist of and how they operate revolutionised our understanding of biology and facilitated rapid progress in medicine. Yet, resolving features smaller than $\sim 200\,\mathrm{nm}$ remained out of reach owing to the diffraction limit of light: As first described by *Ernst Abbe* in the late 19th century

[Abb73], a light microscope's resolution is fundamentally limited to approximately half of the employed wavelength.

This resolution can be increased by using shorter wavelengths, sparking the development of x-ray [Fal11], and electron microscopy [Van12]. Nowadays, electron microscopy even allows for atomic resolution. However, the spatial resolution in both techniques is still limited by diffraction and governed by the respective wavelengths. For atomic resolution electron microscopy, kiloelectronvolt (keV) electron energies are necessary. This energy scale is orders of magnitude larger than many fundamental excitations in solids, many of which lie in the few electronvolt (eV) or millielectronvolt (meV) range [Bas11, Che14, Cao18, Wan18]. To investigate these excitations directly on the nanoscale, different techniques are required.

Super-resolved fluorescence microscopy harnesses nonlinear light-matter interaction to achieve sub-diffractional imaging [Hel07], a milestone acknowledged with the 2014 Nobel Prize in Chemistry. One such technique, stimulated emission depletion microscopy, uses light of a specific wavelength to excite a select transition in a fluorescing chemical compound, the fluorophore. Fluorescence can then be suppressed by stimulated emission at the fluorescing wavelength using a doughnut-shaped beam profile. Since the probability of a fluorophore remaining in the excited state decreases nonlinearly with the intensity of the depleting beam, the surviving fluorescence-emitting region is confined to well below the diffraction limit. Scanning this confined fluorescence spot across the sample enables sub-diffractional optical imaging. These methods excel in biological imaging, offering 3D visualization, but rely on fluorescent labels and visible to near-infrared frequencies. For materials where labelling is not an option, label-free imaging and spectroscopy at the nanoscale are necessary.

The diffraction limit can also be overcome by using linear light-matter interaction with non-propagating evanescent fields, which do not adhere to the diffraction limit [Nov12]. This idea gave birth to the field of near-field microscopy [Che19b, Hil25], where light-matter interaction with evanescent fields confined to sub-wavelength sized objects is investigated. Early experiments focused on light transmitted through small apertures. Today, scattering-type scanning near-field optical microscopy (SNOM) based on light confined to nanoscale metallic tips is predominantly used. SNOM provides nanometre spatial resolution irrespective of the employed wavelength, making it ideally suited for low-energy spectroscopy with mid-infrared or terahertz radiation.

This has revolutionised our understanding of light-matter interaction at the nanoscale, granting direct access to phase transitions [Qaz07, Hub16], photochemistry in real working conditions [Mei23], and exotic quasiparticles [Fei12, Che12, Hub17, Hu20, Pla21, Zha21a].

However, reaching these length scales comes with an additional challenge: Dynamics at the nanoscale occur on much shorter time scales than those of macroscopic objects [Zew00, Kra09]. For example, to investigate key molecular dynamics on their intrinsic time scales – such as vibrations of the molecular frame or atomic rearrangements during chemical reactions – a time resolution of $\sim$100 fs or better is needed [Zew00, Kra09]. Thus, pushing optical microscopy not only to the smallest length but also to the shortest time scales is key to establishing a causal link between nanoscopic elementary dynamics and macroscopic functionalities of condensed matter. As the bandwidth of modern electronics is insufficient to detect such ultrafast dynamics, they can only be accessed with ultrashort light pulses.

The birth of ultrafast science is often ascribed to Eadward Muybridge's experiments in the 19th century [Muy29]. Using an array of cameras with extremely short shutter opening time, he demonstrated that, at certain times, all four hooves of a galloping horse are off the ground simultaneously – a detail too fast for human perception. Today, ultrafast experiments build on the same principle, but instead of mechanical shutters, ultrashort light pulses act as a shutter providing femtosecond snapshots of sample properties [LH21].

One of the most fundamental concepts enabling the measurement of such fast dynamics is ultrafast pump-probe spectroscopy. In such experiments, a pump pulse prepares the system in a specific state while a time-delayed probe pulse analyses its evolution. Varying the delay time between the two pulses by changing their relative optical path lengths allows stroboscopic measurements of ultrafast dynamics. Combining pump-probe techniques with subcycle field-resolved measurements by electro-optic and streaking techniques has revolutionised our understanding of light-matter interaction. Directly mapping the time evolution of the carrier wave has provided access to the full classical information of light [Kie04, Lei23] as well as quantum field fluctuations [Rie15, BC19]. These capabilities have shaped strong-field and attosecond science [Cor07, Kra09], providing insights into dynamics faster than a cycle of light – from ultrafast screening [Hub01] and lightwave-driven charge-carrier

acceleration [Wim14, Hoh15, Boo22, Bor23] to electron tunnelling [Sha12, Sai19] and many-body correlations [Fre22]. Subcycle optical information from single atoms, however, has so far remained elusive.

Combining subcycle time resolution with near-field microscopy has granted access to the temporal evolution of the nanoscale dielectric function on combined length and time scales of $\sim 10\,\mathrm{nm}$ and $\sim 10\,\mathrm{fs}$ [Eis14]. Watching the nanocosm in motion has provided fascinating insights, such as revealing local charge transfer dynamics [Pla21], phase transitions [Hub16, Sti18, Sid22], and ultrafast plasmonic responses [Wag14, Ni16, Ang25]. However, in near-field microscopy the spatial resolution is limited by the tip's finite radius of curvature [Nov12], which is typically on the order of tens of nanometres [Hil25].

Tantalising glimpses into ultrafast atomic-scale dynamics have been made possible by lightwave-driven scanning tunnelling microscopy, where the d.c. bias voltage of a scanning tunnelling microscope is replaced with an ultrafast a.c. bias voltage – the oscillating carrier wave of a phase-locked light pulse [Coc16, Pel20, Pel21, Roe24]. Tracing rectified, time-averaged lightwave-driven tunnelling currents in pump-probe experiments has enabled capturing the first ultrafast single-molecule movies [Coc16, Pel20], inspiring a fast-growing research field [Jel17, Luo20, Yos21, Amm21, Pel21, Amm22, Roe24, Jel24]. Yet, measuring the rapid motion of electrons driven on a subcycle time scale remains out of reach.

In this thesis, I will demonstrate how we utilised nonlinear light-matter interaction with tip-confined evanescent fields to promote all-optical microscopy to simultaneous atomic-scale spatial and subcycle time resolution [Sid24]. In this context, we found a novel non-classical near-field response characterised by a $\pi/2$ phase shift with respect to the conventional near fields. This novel signal is emitted from the ultrafast a.c. tunnelling of electrons driven on subcycle time scales. Leveraging this near-field optical tunnelling emission (NOTE) signal, we achieved atomic-scale spatial resolution and directly measured ultrafast tunnelling currents with subcycle time resolution. Surprisingly, we observed finite ultrafast tunnelling currents even for bias voltages within the band gap of a van der Waals semiconductor.

Chapter 2 will provide an overview of two state-of-the-art ultrafast nanoscopy techniques – ultrafast near-field microscopy (section 2.1) and lightwave-driven scanning tunnelling microscopy (section 2.2).

In chapter 3, I will introduce the novel experimental setup that we developed to find out how far we can push the spatial resolution of subcycle terahertz near-field microscopy. For this we combine a megahertz repetition rate, high-power terahertz source (sections 3.1 and 3.2) and field-resolved detection via electro-optic sampling with a commercial low-temperature ultra-high vacuum scanning probe microscope. This microscope is equipped with stiff qPlus atomic-force microscopy sensors, and customised with optical access via two high numerical aperture parabolic mirrors (section 3.3). Operating in such a stable regime allows us to perform near-field measurements at atomic-scale tip-sample separations.

In chapter 4, we observe a novel near-field response that is in phase with the vector potential of the driving field and confined to significantly smaller volumes than the conventional near-field signal. Operating at tapping amplitudes orders of magnitude smaller than customary, we find that this signal decays on atomic length scales (section 4.2). I will show in section 4.3 that this short-ranged signal originates from light emission from ultrafast tunnelling currents. To demonstrate this, we proposed a semiclassical dipole model, and our theory partner *Jan Wilhelm* developed an *ab initio* quantum mechanical model based on time-dependent density functional theory. Both models successfully reproduce the hallmark features of our experimental observations. Section 4.4 presents all-optical atomic-scale resolution microscopy of defects in a Au(111) surface and section 4.5 explores atomic-scale subcycle spectroscopy on a monolayer of tungsten diselenide. By accounting for the complex-valued transfer function from the near field of the tip to the far field and the response function of our detection setup, we can reconstruct the atomic-scale dipole at the apex of the microscope's tip which emits the novel signal. This allows us to retrieve the subcycle tunnelling currents driven between tip and sample directly in the time domain, even within the band gap of a semiconducting van der Waals material (section 4.6).

In chapter 5, I will introduce how we developed a tunable optical pump source at megahertz repetition rates, to improve the capabilities of our experimental setup. We build on optical parametric amplification (section 5.1) to set up a two-stage noncollinear optical parametric amplifier operating at pulse repetition rates of up

to 8.26 MHz (section 5.2). In section 5.3, I will introduce a novel pump modulation scheme, which circumvents modulating the optical power and thus enables measurements without artefacts arising from periodic modulation of the thermal expansion of the tip.
Chapter 6 will summarise the findings presented in this thesis and provide an outlook on future research directions.

Chapter 2

# Ultrafast nanoscopy

The nanocosm is constantly in motion. Single molecules vibrate [Sti98, Mal23] and rotate [Mal23], electronic wave packets evolve [Bre05, Kra09], and chemical reactions unfold on ultrafast time scales [Zew00, Dan24]. In crystalline media, atomic cores oscillate collectively – known as phonons [Cur22] – while quasi-free electrons in metals or electron-hole pairs in semiconductors give rise to collective plasma oscillations, known as plasmons [Noz58]. Electrons and holes can also form hydrogen-like bound states – so-called excitons [Che14]. Interactions between these fundamental excitations shape key physical properties of condensed matter systems. For instance, electron-phonon coupling can lead to superconductivity [Bar57]. When light and matter couple strongly, hybrid light-matter states – called polaritons – can emerge [Bas16, Bas21]. These dynamics occur on a vast range of ultrashort time scales ranging from picoseconds ($10^{-12}$ s) or femto- ($10^{-15}$ s) to attoseconds ($10^{-18}$ s).

To custom tailor the macroscopic functionalities of condensed matter systems, it is essential to understand the intricate interplay of these elementary excitations. In line with the well-known proverb *"seeing is believing"*, watching these dynamics unfold in real space on their intrinsic length and time scales is one of the key challenges of modern science. Thus, ultrafast nanoscopy is rapidly growing into a vibrant research field [Dhi17, Lei23, Hil25, Zha25].

This chapter will provide a short introduction into two of the most advanced ultrafast nanoscopy techniques – ultrafast near-field microscopy (section 2.1) and lightwave-driven scanning tunnelling microscopy (section 2.2).

## 2.1 Ultrafast scanning near-field optical microscopy

Scanning near-field optical microscopy (SNOM) [Nov12, Che19b, Hil25] uses linear light-matter interaction with evanescent fields[1] confined to nanoscale metallic objects to overcome the diffraction limit. This technique has become a powerful tool for investigating the nanoworld, offering insights into phase transitions [Qaz07, Hub16], as well as quasiparticles such as Dirac plasmons in graphene [Fei12, Che12, Lun17, Zha21b, Don21, Ang25], topological polaritons in molybdenum trioxide [Hu20] and hyperbolic polaritons [Zha21a]. Additionally, SNOM has provided access to photochemistry [Mei23], and light-matter interaction in quantum materials [Sun18].

The concept of SNOM was first proposed by *Edward Synge* in 1928 [Syn28]. He suggested illuminating a sub-wavelength-sized hole (diameter: 10 nm) from one side, allowing the light to pass through the aperture and interact with a sample placed in direct proximity on the other side. The transmitted light would then be detected, enabling optical measurements beyond the diffraction limit, promising a spatial resolution of a few nanometres. This idea was experimentally realised in the second half of the 20th century [Ash72, Lew84, Poh84].

Nowadays, in near-field microscopy, light is typically focused onto the apex of a sharp metallic tip of an atomic force microscope (AFM) positioned above a sample (Fig. 2.1**a**). The tip confines the light field spatially, significantly enhancing the local field strength. This efficiently generates localised evanescent fields beneath the tip that probe the sample's optical response at the nanoscale. As a result, the scattered light carries information about the sample's local dielectric properties. This scattered signal is detected and analysed in the far field. By scanning the sample laterally and detecting the scattered light for each position, near-field microscopy enables mapping the sample's local dielectric function with a spatial resolution determined by the radius of curvature of the tip's apex, which usually is in the range of a few tens of nanometres [Hil25].

[1] Evanescent fields are non-propagating electromagnetic waves that decay exponentially away from interfaces.

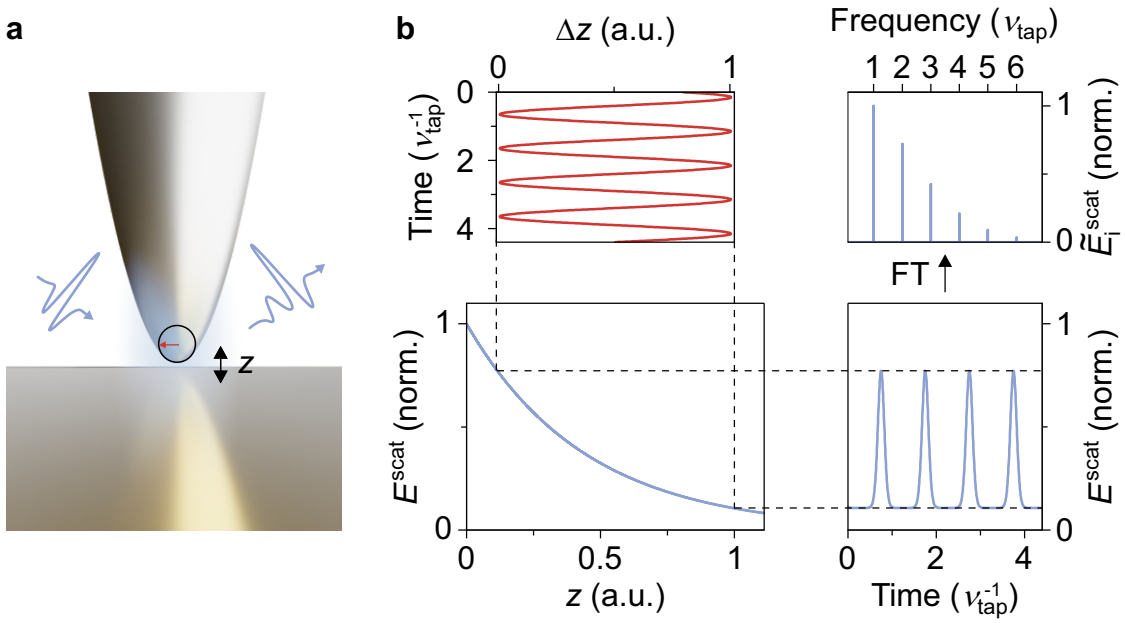


**Figure 2.1 |** Scanning near-field optical microscopy. **a**, A transient electric field waveform is coupled to the apex of a sharp metallic tip (apex radius of curvature $r_{\mathrm{tip}}$, indicated by the circle and red arrow) and the scattered radiation, containing information on the nanoscale dielectric function, is detected. **b**, The scattered field $E^{\mathrm{scat}}$ features a nonlinear tip-sample distance ($z$) dependence (bottom left). Thus, when periodically modulating the relative tip-sample distance ($\Delta z$) at the tapping frequency $\nu_{\mathrm{tap}}$ (top left), the scattered signal features bursts at each point of closest approach in the tapping cycle with period $\nu_{\mathrm{tap}}^{-1}$ (bottom right). Performing a Fourier transform (FT) reveals the harmonic constituents $\tilde{E}_{\mathrm{i}}^{\mathrm{scat}}$ of the scattered signal (top right), which allow for separating the near-field and far-field signals, and thus grant access to nanoscale spatial resolution.

**Isolating the scattered light.** The volume in which near-field interaction occurs in SNOM is determined by the size of the tip's apex [Moo20] ($\sim 1 \times 10^{-24}\,\mathrm{m}^3$ for a tip-apex radius of curvature of $r_{\mathrm{tip}} = 10\,\mathrm{nm}$). Specifically for long wavelengths, as in the terahertz (THz) spectral range, this volume is several orders of magnitude smaller than a diffraction-limited focal spot size ($\sim 3 \times 10^{-12}\,\mathrm{m}^3$ for 1 THz). Therefore any optical signal collected will be dominated by the far-field signal consisting mostly of the specular reflection off the sample's surface.
However, one can make use of the fact that the near-field interaction features a nonlinear tip-sample distance dependence (Fig. 2.1**b**, equation 2.4), owing to its evanescent nature, whereas the far field does not. When tapping the AFM tip sinusoidally at a frequency $\nu_{\mathrm{tap}}$ [Kno99, Hil25], the scattered field $E^{\mathrm{scat}}$ is modulated: Periodic bursts occur each time the tip reaches the point of closest approach (bottom right in Fig. 2.1**b**). By performing a Fourier transform of this signal, we find that it contains higher harmonics of the tapping frequency $\nu_{\mathrm{tap}}$ (top right), which arise owing to the nonlinear tip-sample distance dependence of the near fields. Spurious far-field signals, originating e.g. from scattering at the oscillating tip shaft, might contaminate the signal. This contribution can be suppressed by measuring at higher harmonics or smaller tapping amplitudes [Hil25]. Thus, to isolate the near-field signal, we use lock-in detection and demodulate at integer multiples of $\nu_{\mathrm{tap}}$, which provides access to the sample's local dielectric response.

**The point-dipole model.** Over the years, various methods have been developed to model the near-field interaction, including sophisticated finite element simulations [Moo20]. However, the first approach to model the near-field interaction in the quasi-electrostatic limit – an analytical point dipole model [Kno99, Kno00, Che19b] – already provides a remarkably good description. In this model, the carrier wave of light transiently displaces electrons within the tip, forming a time-dependent dipole within its apex with a strongly confined near field. This near field interacts with the charges in the sample, inducing a polarisation that depends on the sample's local dielectric function. The sample's response is approximated by an image dipole whose field, in turn, modifies the tip dipole. The oscillating tip dipole thus encodes information on the sample's local dielectric function into the scattered light.

In the point-dipole model, the tip is approximated as a sphere with a radius equal to the tip's apex radius of curvature $r_{\text{tip}}$. Its polarisability $\alpha$ is given by [Kno00]

$$\alpha = 4\pi r_{\text{tip}}^3 \frac{\epsilon_{\text{tip}} - 1}{\epsilon_{\text{tip}} + 2}, \tag{2.1}$$

where $\epsilon_{\text{tip}}$ is the dielectric function of the tip. The centre of the spherical tip is positioned at a distance $d$ above a sample which fills the infinite half-space beneath the tip. When an external electric field $E$ which is polarised perpendicular to the sample's surface is applied, it induces a dipole moment $p$ within the spherical tip given by

$$p = \alpha E. \tag{2.2}$$

The electric field of this dipole polarises the sample, and the sample's response can be described by an image dipole $p' = \beta p$ located at a distance of $2d$ from the centre of the spherical tip. $\beta = \frac{\epsilon_{\text{sample}}-1}{\epsilon_{\text{sample}}+1}$ is the sample's reflection coefficient and $\epsilon_{\text{sample}}$ the sample's dielectric function. This image dipole acts back on the tip dipole which is modified to [Kno00]

$$p = \alpha(E + \frac{p'}{16\pi d^3}) = \alpha_{\text{eff}} E. \tag{2.3}$$

Here, the effective polarisability $\alpha_{\text{eff}}$ is given by [Kno00]

$$\alpha_{\text{eff}} = \frac{\alpha}{1 - \frac{\alpha\beta}{16\pi d^3}}. \tag{2.4}$$

The oscillating time-dependent dipole in the tip, according to Maxwell's equations, emits light which can be detected in the far field. There, the amplitude of the scattered electric field $E^{\text{scat}}$ scales with

$$E^{\text{scat}} \propto \alpha_{\text{eff}} E, \tag{2.5}$$

and contains information on $\epsilon_{\text{sample}}$.

**Ultrafast scanning near-field optical microscopy.** Thanks to the all-optical nature of SNOM, it can leverage the full potential of ultrafast optics. Combining SNOM with ultrafast excitation and probing has allowed it to trace the femtosecond

time evolution of the nanoscale dielectric function [Eis14, Wag14, Hub16, Hub17, Jia19, Pla21, Ste21], providing e.g. access to the ultrafast insulator-to-metal phase transition of vanadium dioxide on nanometre length scales [Hub16], and enabling femtosecond nano-videography of interface polaritons excited by photo-induced interband transitions in black phosphorus heterostructures [Hub17].

In combination with subcycle field resolution via electro-optic sampling, SNOM in the mid-infrared spectral range has enabled the study of local photoinduced carrier dynamics in single indium-arsenide nanowires [Eis14]. Subcycle field-resolved THz-SNOM [Moo12, Sti18, Jin21, Pla21, Kim23, Ziz24] traces ultrafast changes in the sample's polarisability. This makes it sensitive to all charge carriers, independent of selection rules. Subcycle THz-SNOM has proven to be an extremely useful and versatile tool, providing insights into charge-transfer processes in transition metal dichalcogenide (TMDC) heterostructures on nanometre length scales [Pla21]. Furthermore, probing the ultrafast nonequilibrium dynamics of excitons – bound electron-hole pairs – in monolayers and bilayers of TMDCs with nanometre spatial resolution has revealed nanoscale variations in the excitonic Mott transition – a transition from an excitonic gas to an electron-hole plasma [Sid22]. Recently, THz-SNOM has provided nanoscale insights into carrier dynamics in metal halide perovskites [Kim22, Ziz24], which are promising new solar cell materials [Gre14, Zuo16, Ron18]. There, by analysing deep-subcycle time shifts, the interplay of nanoscale variations in structure and chemical composition with ultrafast carrier transport has been investigated [Ziz24]. Together with a tunable optical pump source, subcycle THz-SNOM was employed to gain insights into the ultrafast dielectric response of quasi-one-dimensional excitons in monolayers of the van-der-Waals magnet CrSBr [Mei24]. Recently, dynamics of surface plasmon polaritons in graphene were imaged directly in space and time [Ang25]. There, the polariton propagation was even controlled on a subcycle time scale using optical pump pulses.

Even though SNOM has provided fascinating insights into the nanocosm in motion, so far, the spatial resolution of SNOM is limited by the nanometre size of the tip's apex, preventing it from achieving atomic resolution. However, a first glimpse into femtosecond atomic-scale dynamics has been provided by the recent invention of lightwave-driven scanning tunnelling microscopy, which will be detailed in the next section.

## 2.2 Lightwave-driven scanning tunnelling microscopy

Scanning tunnelling microscopy (STM) [Bin82, Bin83] revolutionised surface science by visualising single atoms. Owing to this success, *Gerd Binnig* and *Heinrich Rohrer* received the Nobel Prize in Physics in the year 1986, sharing it with *Ernst Ruska* who was honoured for his contributions to electron microscopy. Today, STM allows to visualise the local density of states of surfaces with sub-atomic precision and even enables the visualisation of quantum mechanical wave functions of single molecular orbitals [Rep05, Lil07, Gro11].
Building on these capabilities, the advent of lightwave-driven STM has offered first insights into ultrafast atomic-scale dynamics. Starting with nanometre-scale resolution [Coc13], it soon achieved atomic spatial resolution and state-selective tunnelling [Coc16]. This rapidly established lightwave-STM as a vibrant and fast-growing research field [Jel17, Luo20, Mül20, Pel20, Pel21, Amm21, Yos21, Amm22, Ara22, Roe24, Jel24]. This section will explain the working principle of both d.c. STM, based on reference [Che21], and lightwave-STM.

**Scanning tunnelling microscopy.** In STM, an atomically sharp metallic tip, usually made of tungsten or platinum-iridium, is brought into atomic-scale proximity of a conducting surface (see Fig. 2.2**a**). Despite being separated by a vacuum barrier, the electronic wave functions of tip and sample overlap, allowing tunnelling currents to flow between them. Since the wave functions decay exponentially into the vacuum barrier, these tunnelling currents depend strongly on the tip-sample separation – for metals, the tunnelling current typically decays by about one decade per angstrom. Via piezo actuators, the tip or sample can be scanned in $x$, $y$ and $z$, enabling mapping of these tunnelling currents with sub-angstrom precision. The potential landscape of such a tunnelling junction is shown in Fig. 2.2**b**. There, the local density of states of the sample (s) and tip (t) are filled to their respective Fermi energies $E_{\mathrm{F,s}}$ and $E_{\mathrm{F,t}}$. Tip and sample are separated by a vacuum barrier of the height of the work function $\phi$, which is assumed to be the same for sample and tip for simplicity. Panel **c** shows what happens when a d.c. bias voltage $V$ is applied between tip and sample: The potential landscape is tilted. Now there are free states in the

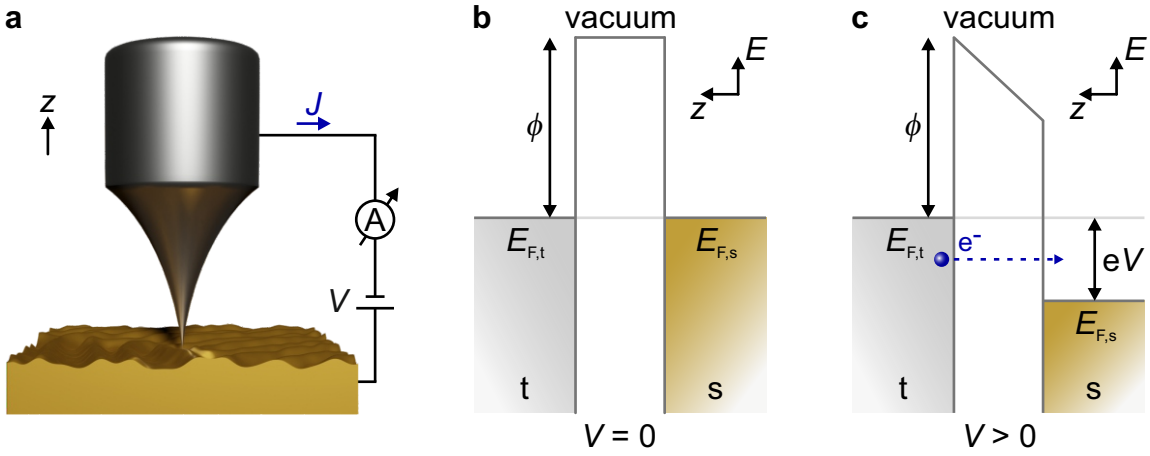


**Figure 2.2 |** Scanning tunnelling microscopy. **a**, An atomically sharp metallic tip is placed in atomic-scale proximity above a conducting sample. When applying a d.c. bias voltage $V$ between tip and sample, a directed tunnelling current $J$ flows which is measured with the readout electronics. Panel **b** shows the potential landscape of the tunnelling junction in an unbiased case. Sample (s) and tip (t) states are filled to their Fermi energies $E_{\mathrm{F,s}}$ and $E_{\mathrm{F,t}}$, respectively. **c**, Applying a bias voltage tilts this potential landscape. Now there are free states in the sample at energies which are occupied in the tip, allowing a directional tunnelling current to flow. $\phi$: Work function, $E$: Energy, e: Elementary charge.

sample at energies which are occupied in the tip, allowing a directed tunnelling current to flow from the tip to the sample. This tunnelling current $J$ is measured electronically (readout electronics depicted schematically in Fig. 2.2**a**) and can be used for atomic-scale imaging. There are two main measurement modes: constant height and constant current. Recording the tunnelling current $J$ while scanning the tip laterally across the sample, i.e. in $x$ and $y$, at a constant height maps out the local electronic structure. In constant-current mode, the current is used as an input for a feedback loop (typically a PID controller), which adjusts the tip height to maintain the tunnelling current at a fixed value. Simultaneously recording the $z$ position of the tip maps out the sample's apparent topography.

Assuming a low temperature, a constant local density of states in the tip over the energy interval from the sample's Fermi energy $E_{\mathrm{F,s}}$ to $E_{\mathrm{F,s}} + \mathrm{e}V$, and a spherically

symmetric tip, the tunnelling current can be approximated as [Che21]

$$J \propto \int_0^{\mathrm{e}V} \rho_{\mathrm{s}}(E_{\mathrm{F,s}} + \varepsilon, \boldsymbol{r})\mathrm{d}\varepsilon. \tag{2.6}$$

Here, $\rho_{\mathrm{s}}$ denotes the sample's local density of states, and $\boldsymbol{r}$ represents the position of the tip. Differentiating this equation yields

$$\frac{\mathrm{d}J}{\mathrm{d}V} \propto \rho_{\mathrm{s}}(E_{\mathrm{F,s}} + \mathrm{e}V, \boldsymbol{r}). \tag{2.7}$$

Thus measuring the differential conductance $\mathrm{d}J/\mathrm{d}V$ provides access to the sample's local density of states. This technique is known as scanning tunnelling spectroscopy.

**The strong-field regime.** To make STM ultrafast, the d.c. bias can be replaced with the fastest controllable bias: the oscillating carrier wave of a phase-locked single-cycle light pulse which confines the tunnelling current to a femtosecond time window [Coc13, Coc16]. Yet, light-matter interaction at an STM tunnelling junction can occur in two fundamentally different regimes: (i) the **(multi-)photon absorption regime**, and (ii) the **strong-field regime**, where the oscillating electric field acts like a classical quasi-static bias field. To ensure operation in the latter regime, the **Keldysh parameter** $\gamma$ serves as a figure of merit to distinguish between these regimes [Kel65]:

$$\gamma = \sqrt{\frac{\epsilon}{2U_{\mathrm{p}}}} = \omega\frac{\sqrt{2m_{\mathrm{e}}\epsilon}}{\mathrm{e}E}. \tag{2.8}$$

The Keldysh parameter compares the system's excitation energy $\epsilon$ with the ponderomotive energy $U_{\mathrm{p}} = \frac{\mathrm{e}^2E^2}{4m\omega^2}$ – the cycle-averaged kinetic energy of an electron performing a quiver motion from acceleration within an oscillating electric field. $m_{\mathrm{e}}$ denotes the electron mass, e the elementary charge, $\omega$ the angular frequency of the incident lightwave, and $E$ the electric field amplitude. For $\gamma \gg 1$, i.e. high frequencies and low field strengths, the ponderomotive energy gained by electrons accelerated by the light's carrier wave is much lower than the excitation energy. Here, the excitation is dominated by absorption of one or multiple photons. Conversely, for $\gamma < 1$, i.e. high electric field strengths and low frequencies, field-driven effects

dominate. Here, the carrier wave of light acts as a classical field which dynamically alters the potential landscape.
Many relevant excitation energies, such as interband excitations in semiconductors [Cos16, Wan18], molecular resonances [Rep05, Lil07], or work functions of metals [Che21] lie in the range of electronvolts. To reach the field-driven regime, intense light fields with photon energies significantly lower than the relevant excitation energies are required. For this purpose, light in the terahertz[2] (THz) to mid-infrared[3] spectral range is often used. On the one hand, the comparatively low photon energies (∼4 meV to 250 meV) are typically far from the relevant excitation energies. On the other hand, the oscillation half-cycles with durations in the range of femtoseconds remain short enough to resolve many fundamental ultrafast processes.
Operating in the field-driven regime has led to the emergence of the field of lightwave electronics [Bor23, Kir25], where the carrier wave of light is harnessed to dynamically steer charge carriers faster than a cycle of light [Sch14, Hoh15, Lan16, Rei18, Bor20, Sch21, Fre22]. These advances even hold the potential for computing at clock rates in the petahertz range.

**Lightwave-driven scanning tunnelling microscopy.** Combining the concept of lightwave electronics with STM has led to the development of lightwave-driven STM. This technique was first demonstrated in an ambient-air STM [Coc13] and later promoted to atomic resolution and state selective tunnelling using an ultra-high vacuum low-temperature STM [Coc16, Pel20, Pel21].
Figure 2.3**a** shows schematically the experimental setup. A single-cycle waveform is coupled to the apex of an STM tip which is positioned above a conductive sample. Any time-averaged current $J$ flowing between tip and sample can be measured with the STM's readout electronics. An exemplary d.c. tunnelling conductance, i.e. $J$-$V$ curve, of a Au(111) surface is shown in Fig. 2.3**b**. A phase-locked single-cycle electric field waveform (Fig. 2.3**a**,**c**) acts as an ultrafast transient bias voltage which drives an a.c. tunnelling current $J_{\mathrm{lw}}$ between tip and sample. In the approximation of instantaneous tunnelling, at any point in time, the instantaneous lightwave bias drives a current proportional to the d.c. tunnelling conductance evaluated at the

[2] ∼1 THz to 10 THz
[3] ∼10 THz to 60 THz

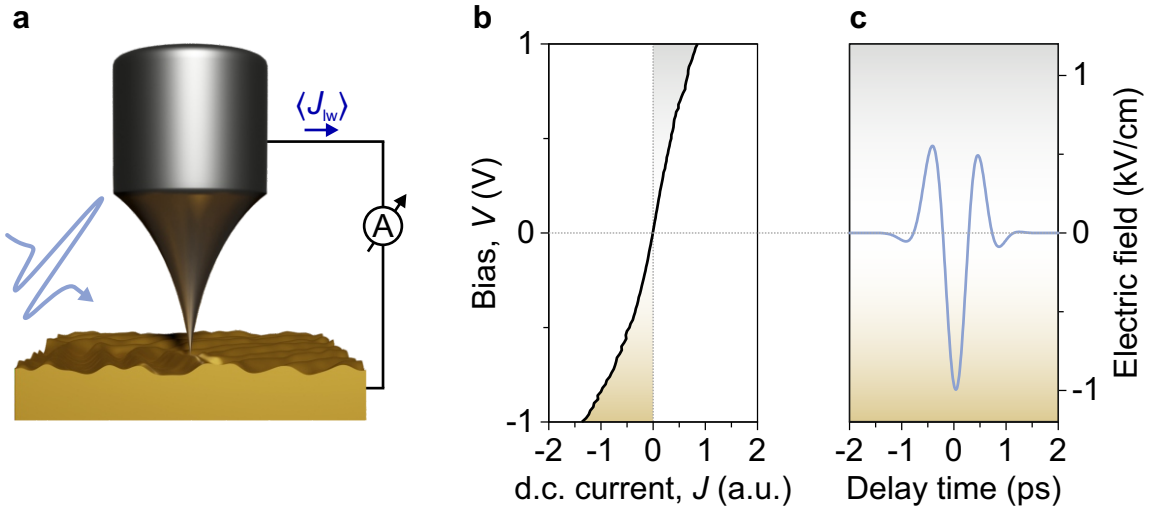


**Figure 2.3 |** Lightwave-driven scanning tunnelling microscopy. **a**, An electric field waveform (light blue) replaces the DC bias voltage in an STM, confining the tunnelling current in time. Depending on the sample's conductance, i.e. the $J$-$V$ curve (**b**), and the exact shape of the electric field waveform (**c**), more electrons might tunnel to one side (gold coloured) than the other (silver coloured) within one pulse. This leads to a rectified time-averaged current $\langle J_{\mathrm{lw}} \rangle$ which can be detected with the STM's readout electronics.

respective voltage. If more electrons tunnel to one side than the other within one pulse, a time-averaged lightwave-driven tunnelling current $\langle J_{\mathrm{lw}} \rangle$ can be measured with the STM preamplifier. Such a time-averaged lightwave-driven tunnelling current originates from asymmetries in the sample's $J$-$V$ characteristics, which rectify the ultrafast tunnelling currents. For instance, in the case shown in Fig. 2.3**b**,**c**, the time-averaged tunnelling current would be negative, as the largest half-cycle of the THz waveform is negative, and the tunnelling conductance at negative bias voltages outweighs that at positive bias voltages. The time-averaged rectified tunnelling current is given by

$$\langle J_{\mathrm{lw}} \rangle = \nu_{\mathrm{rep}} \, N_{\mathrm{rectified}} \, \mathrm{e}, \tag{2.9}$$

where $\nu_{\mathrm{rep}}$ is the pulse repetition rate of the laser, $N_{\mathrm{rectified}}$ is the number of electrons rectified per pulse and e is the elementary charge.

State-selective tunnelling can be achieved by using asymmetric electric field waveforms and energetically localised states, such as a lowest unoccupied molecular orbital of a

pentacene molecule [Coc16]. When tuning the electric field strength, such that only the peak of the largest half-cycle reaches the tunnelling resonance, selective single-electron tunnelling via this state is possible. As a result, the tunnelling current is confined to just a fraction of the transient bias waveform, enabling $\sim$100 fs snapshots of molecular orbitals for a centre frequency of $\sim$1 THz [Coc16]. Employing a THz pump—THz probe measurement scheme, state-selective lightwave-STM realised the dream of watching the coherent motion of a single molecule moving on its intrinsic length and time scales [Coc16].

These advancements have prompted a vibrant research field exploring the nanoworld in motion on atomic length scales: The carrier wave in the near field of the tunnelling junction, acting as a femtosecond atomic-scale force, has been used to coherently control the motion of a single-molecule switch [Pel20]. Using such a switch as a local bias gauge, the tip-confined THz-induced near-field waveform was sampled with subcycle temporal and atomic-scale spatial resolution directly in the tunnelling junction [Pel21]. Lightwave-STM combined with optical pumping enabled the direct observation of the picosecond spreading dynamics of electrons optically excited into the lowest unoccupied molecular orbital of a $C_{60}$ molecular film [Yos21]. Recently, ultrafast lightwave-driven scanning tunnelling spectroscopy was demonstrated [Roe24], combining angstrom spatial, femtosecond temporal and meV energy resolution. In this work, sweeping the THz bias voltage and recording the rectified tunnelling current provided access to ultrafast changes in the local density of states. THz pump—THz probe experiments on single-atom defects in a transition metal dichalcogenide monolayer within the same study revealed effects of electron-phonon coupling at the atomic scale.

Lightwave-STM has revolutionised our access to and understanding of physics at the ultimate time and length scales. It excels in systems with isolated energy levels, where ultrafast tunnelling can be approximated as unidirectional. Yet in more complex systems, lightwave-STM may not capture all relevant dynamics, as it only provides access to the time-integrated action of the entire driving light pulse. The dynamics in the tunnelling junction of a lightwave-STM are extremely far from equilibrium, with tunnelling conductances that differ drastically from the steady state [Jel17]. These ultrafast tunnelling currents are governed by multiple competing nonlinearities, which depend on the specific conditions of ultrafast tunnelling and

dynamics within the sample. For instance, as seen in references [Pel21, Roe24], tunnelling of a single electron already alters the potential landscape for subsequent electrons. Consequently, the reconstruction of ultrafast tunnelling currents requires model assumptions that are only reliable under the most well-defined conditions. Subcycle resolution at atomic length scales, potentially even of ultrafast tunnelling currents, could be crucial for understanding the complex interplay of competing nonlinearities at these ultimately short time and length scales.

This raises the central question: *Can we combine the strengths of lightwave-STM and subcycle near-field microscopy to access subcycle dynamics at atomic length scales?* To address this challenge, we developed a novel THz-SNOM that integrates the key advantages of both techniques. (i) It has access to the subcycle time scale by tracing the scattered electric field waveforms in electro-optic sampling, and (ii) operates in the most stable conditions with picometre-precise piezo positioning in a low-temperature and UHV environment. The next chapter provides a detailed description of this experimental setup.

Chapter 3

# A low-temperature subcycle near-field microscope

*This chapter details the experimental setup of our low-temperature SNOM. During the first years of my PhD, I focused on developing the optical setup described in this chapter, together with Master's and Bachelor's students Peter Menden and Sonja Lingl, under the guidance of Rupert Huber, and with contributions from the other authors in reference* [Sid24]. *The development of the low-temperature ultra-high vacuum scanning probe microscope was primarily led by Fabian Sandner, Felix Schiegl, Thomas Siday, Yaroslav Gerasimenko & Rupert Huber with contributions from all authors in reference* [Sid24].

SNOM measures light scattered from nanoscale metallic tips to provide information on the nanoscale dielectric function. Unlike lightwave-STM, which is limited to conductive samples and lacks subcycle temporal resolution, SNOM does not require electrically conductive samples and offers direct subcycle time resolution. Thus, promoting SNOM to atomic length scales would significantly broaden the range of material systems accessible on atomic length and ultrafast time scales, while even granting access to phenomena occurring on subcycle time scales.

To push the spatial resolution limits of SNOM, we promote subcycle near-field microscopy to the most stable configurations: An ultra-high-vacuum (UHV) envi-

ronment (pressure $\approx 10^{-10}$ mbar) at temperatures down to 10 K, together with a milliwatt-level phase-stable THz source operating at MHz pulse repetition rates.
This chapter details the development of our novel experimental setup. Section 3.1 will provide an overview of the experimental setup, including the employed laser, the THz generation, the microscope and the optical detection. In section 3.2, I will explain the details of the THz generation setup based on tilted-pulse-front optical rectification and the field-resolved detection via electro-optic sampling (EOS). Finally, I will outline the key aspects of our low-temperature UHV scanning probe microscope which set it apart from the AFMs used in conventional SNOMs (section 3.3).

## 3.1 Terahertz scanning near-field optical microscopy at cryogenic temperatures

The key to our approach is to use a commercial low-temperature ultra-high vacuum combined STM/AFM with a customized high numerical aperture optical access and couple this with a high-power, high pulse repetition rate phase-locked THz source.
Our experimental setup is sketched in Fig. 3.1. We start with a commercial high-power ytterbium-fibre amplifier which provides pulses in the near-infrared (NIR) spectral range with a centre wavelength of 1030 nm and a pulse duration of 260 fs at an average power of 50 W. The pulse repetition rate can be tuned to integer divisions of the oscillator repetition rate of 41.3 MHz, with a maximum pulse energy of 40 µJ reached at 1.25 MHz. These pulses are used for THz generation via optical rectification in a lithium niobate ($LiNbO_3$) crystal. Phase matching is achieved by tilting the near-infrared pulse's intensity fronts (details in section 3.2.2), which we realise by imaging a diffraction grating into the crystal.
A custom-designed Teflon lens ensures that both the horizontal and the vertical axes of the THz beam are focused onto the incoupling parabolic mirror of the microscope, which subsequently focuses the THz pulses onto an atomically sharp tungsten tip. This tip is mounted to a stiff qPlus sensor (section 3.3 & Fig. 3.7), allowing for atomic-scale tapping amplitudes at the tapping frequency $\nu_{\mathrm{tap}} \approx 20$ kHz. $\nu_{\mathrm{tap}}$ is orders of magnitude lower than the laser's pulse repetition rate. This ensures that heat is deposited onto the tip in a quasi-continuous manner, avoiding artefacts arising

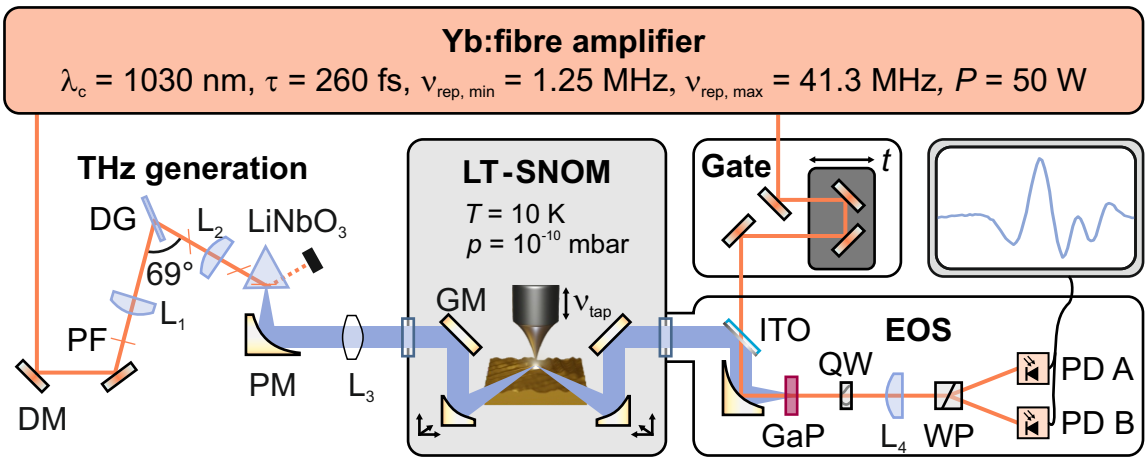


**Figure 3.1** | Experimental setup. An ytterbium-fibre amplifier provides pulses with a centre wavelength of $\lambda_c = 1030\,\mathrm{nm}$, a pulse duration of $\tau = 260\,\mathrm{fs}$, a pulse repetition rate tunable between $\nu_{\mathrm{rep,\,min}} = 1.25\,\mathrm{MHz}$ and $\nu_{\mathrm{rep,\,max}} = 41.3\,\mathrm{MHz}$ at an average power of $P = 50\,\mathrm{W}$. The majority of the laser's output is used to seed the THz generation, where the THz probe pulses are generated via optical rectification in lithium niobate ($LiNbO_3$) in the tilted-pulse-front phase-matching condition. The pulse-front (PF) tilt is induced by a diffraction grating (DG) and imaged into the $LiNbO_3$ crystal via an imaging lens ($L_2$). The first lens ($L_1$) sets the peak intensity within the $LiNbO_3$ crystal and a parabolic mirror (PM) collimates the THz radiation. Owing to the anisotropic THz generation geometry and the inherent diffraction-induced divergence, a half-cylindrical, half-spherical Teflon lens ($L_3$) is used to refocus the THz beam onto the first LT-SNOM parabolic mirror. This mirror focuses the THz radiation onto the tip, which is mounted on a stiff qPlus sensor that can oscillate at the tapping frequency $\nu_{\mathrm{tap}}$. The second LT-SNOM parabolic collects the scattered radiation which is then detected via electro-optic sampling (EOS). ITO: Quartz window covered with a layer of indium-tin oxide, DM: Dielectric mirror, GM: Gold mirror, GaP: ⟨110⟩-oriented gallium phosphide crystal, QW: Quarter-wave plate, WP: Wollaston polariser, PD: Photodiode.

from thermal expansion bursts during the tapping cycle. The qPlus sensor's electrical contacts enable tunnelling-current measurements through the STM preamplifier, allowing us to perform lightwave-STM measurements. Both tip and sample are mounted in a vibration-isolated fashion in a UHV chamber with pressures of about $10^{-10}$ mbar and cooled to temperatures down to 10 K via a liquid-helium cryostat. For SNOM, a second parabolic mirror collects the scattered radiation. The coherently scattered light is detected with subcycle resolution via electro-optic sampling (section 3.2.3), using the laser fundamental as gate pulses. The entire THz beam path outside of the UHV chamber is purged with gaseous nitrogen to circumvent water vapour absorbing the THz radiation.

## 3.2 A high-repetition-rate high-power terahertz source

This section provides a detailed explanation of the THz generation process, expanding on the previous section. I begin by outlining the fundamental requirements for our light source: It has to be in the THz spectral range, have a stable carrier-envelope phase, and it must operate at high average powers at high pulse repetition rates.

**THz spectral range.** Operating at THz frequencies brings unique advantages, as charge carriers in semiconductors exhibit distinct signatures in this spectral range [Hub01, Ulb11, Dhi17, Lei23]. Ultrafast THz-SNOM provides contact-free, non-invasive access to fundamental properties such as charge carrier densities, mobilities, and recombination dynamics – independent of selection rules – while achieving nanoscale spatial resolution [Pla21, Sid22, Ziz24, Mei24, Ang25]. Moreover, the combination of strong fields and low photon energies in the THz spectral range places light-matter interaction in a predominantly field-driven regime, where dynamics are dictated by the instantaneous electric field rather than by (multi-)photon absorption. Operating in this regime could also potentially provide insight into whether lightwave-driven tunnelling currents – such as those in lightwave-STM (section 2.2) – contribute to near-field signals.

**A stable carrier-envelope phase.** To achieve subcycle time resolution, it is imperative that the phase between the maximum of the pulse's intensity envelope and the maximum of the carrier wave – known as the carrier-envelope phase – remains constant. In other words, the waveform must be identical for each light pulse. Only with a stable carrier-envelope phase do the coherent dynamics driven by the light pulse's carrier wave remain identical from shot to shot, allowing for their stroboscopic detection.

**High average powers at high pulse repetition rates.** Since the probing volume in near-field microscopy is orders of magnitude smaller than in far-field experiments, the signal-to-noise ratio is significantly reduced. To compensate this, it is essential to use light sources with high average powers at high pulse repetition rates in the MHz range. This becomes even more crucial when working with atomically sharp tips in a cryogenic-temperature and UHV environment and with atomic-scale tapping amplitudes, where the probing volume could potentially be even smaller. Additionally, being able to drive tunnelling currents between tip and sample would be desirable, as it could potentially offer insights into how tunnelling affects near-field signals. In steady-state STM, bias voltages on the order of volts are employed to reach specific sample resonances [Rep05, Lil07]. Given THz field-enhancement factors on the order of $10^5$ [Pel21], to achieve field strengths in the range of $1\,\mathrm{V\,Å^{-1}}$ at the tunnelling junction, field strengths of approximately $1\,\mathrm{kV\,cm^{-1}}$ are required in the far field.

THz generation via tilted-pulse-front optical rectification of femtosecond NIR pulses in a lithium niobate crystal meets all these requirements. I will explain this procedure in detail in the following two sections. Section 3.2.1 provides an introduction to nonlinear optics, focusing on optical rectification. The concept of tilted-pulse-front optical rectification and the specificities of our THz generation setup are explained in section 3.2.2, and section 3.2.3 will describe how we measure the generated THz waveforms via electro-optic sampling.

### 3.2.1 Nonlinear optics

*The explanation in this section follows that of reference* [Boy08].
Linear optics describes everyday phenomena such as refraction, reflection and transmission, and assumes that the response of a medium to the electric field of light $\boldsymbol{E}$ is linear. In this case, the material's polarisation $\boldsymbol{P}$ is approximated as

$$\boldsymbol{P} \approx \boldsymbol{P}^{(1)} = \epsilon_0 \chi^{(1)} \boldsymbol{E}, \tag{3.1}$$

where $\boldsymbol{P}^{(1)}$ is the linear polarisation, $\epsilon_0$ is the vacuum permittivity and $\chi^{(1)}$ is the linear susceptibility of the medium. However, with the advent of ultrafast lasers, the achievable electric field strengths have increased significantly. At these higher field strengths, the linear approximation no longer holds and one has to take higher orders into account. The polarisation can then be described by a power series expansion of the form

$$\boldsymbol{P} = \epsilon_0 \sum_{n=1}^{\infty} \chi^{(n)} \boldsymbol{E}^n \equiv \sum_n \boldsymbol{P}^{(n)}, \tag{3.2}$$

where $\boldsymbol{P}^{(n)}$ denotes the $n$-th order polarisation and $\chi^{(n)}$ are the nonlinear susceptibilities which are tensors of rank $n+1$.
The first correction to the linear approximation appears at the second order of polarisation, which arises only in non-centrosymmetric crystals, where $\chi^{(2)}$ does not vanish:

$$\boldsymbol{P}^{(2)} = \epsilon_0 \chi^{(2)} \boldsymbol{E}^2. \tag{3.3}$$

When considering an electric field consisting of two different frequencies $\omega_1$ and $\omega_2$, i.e.,

$$\boldsymbol{E}(t) = \boldsymbol{E}_1 e^{-i\omega_1 t} + \boldsymbol{E}_2 e^{-i\omega_2 t} + \text{c.c.}, \tag{3.4}$$

the resulting second-order polarisation is given by

$$\begin{aligned} \boldsymbol{P}^{(2)} = \epsilon_0 \chi^{(2)} \Big[ & \boldsymbol{E}_1^2 e^{-2i\omega_1 t} + \boldsymbol{E}_2^2 e^{-2i\omega_2 t} + 2\boldsymbol{E}_1 \boldsymbol{E}_2 e^{-i(\omega_1+\omega_2)t} \\ & + 2\boldsymbol{E}_1 \boldsymbol{E}_2^* e^{-i(\omega_1-\omega_2)t} + \text{c.c.} \Big] + 2\epsilon_0 \chi^{(2)} \left( \boldsymbol{E}_1 \boldsymbol{E}_1^* + \boldsymbol{E}_2 \boldsymbol{E}_2^* \right). \end{aligned} \tag{3.5}$$

This contains multiple terms oscillating at newly generated frequencies. The terms oscillating at $2\omega_1$ and $2\omega_2$ are called *second-harmonic generation* (SHG). Whereas *sum-frequency generation* (SFG) and *difference-frequency generation* (DFG) re-

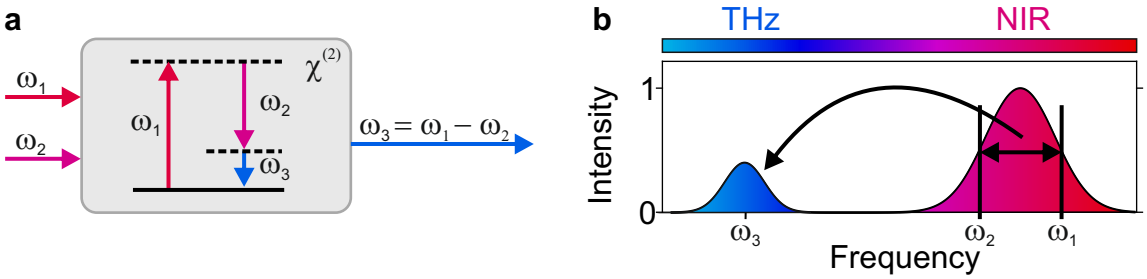


**Figure 3.2 |** Optical rectification of ultrashort near-infrared pulses. **a**, In the photon picture of difference-frequency generation and optical rectification, two photons with frequencies $\omega_1$ and $\omega_2$ interact in a $\chi^{(2)}$ nonlinear medium. There, the higher frequency photon $\omega_1$ splits into two photons, one with the frequency $\omega_2$ and the other at the difference frequency $\omega_3 = \omega_1 - \omega_2$. **b**, An ultrafast NIR pulse features a Gaussian spectral intensity (red). Any two frequencies $\omega_1$ and $\omega_2$ contained in this spectrum can mix to generate a low-frequency component at $\omega_3$ in the THz spectral range.

fer to those oscillating at $\omega_1 + \omega_2$ and $\omega_1 - \omega_2$, respectively. The constant term, $2\epsilon_0\chi^{(2)}\,(\boldsymbol{E}_1\boldsymbol{E}_1^* + \boldsymbol{E}_2\boldsymbol{E}_2^*)$, resulting from $\omega_1 - \omega_1$ and $\omega_2 - \omega_2$ is known as **optical rectification**.

When using ultrafast lasers, the spectral intensity of a light pulse contains a range of frequencies (Fig. 3.2**b**). In this case, optical rectification can be understood as intra-pulse difference-frequency generation, and can generate low-frequency components in the THz or MIR spectral range. Since the phase term vanishes in optical rectification (see equation 3.5), this process generates inherently phase-locked pulses[1]. In the photon picture (Fig. 3.2**a**), (intra-pulse) DFG can be understood as a high-frequency photon, with frequency $\omega_1$, exciting a virtual energy level. The presence of photons with the frequency $\omega_2$ stimulates the emission of two lower-frequency photons with frequencies $\omega_2$ and $\omega_3$. There, energy conservation is automatically satisfied, since $\hbar\omega_1 = \hbar\omega_2 + \hbar\omega_3$. Yet, simultaneous momentum conservation is not a given.

**Phase matching.** In nonlinear optical processes, momentum conservation can be expressed in the photon picture as the requirement that the total momentum of all

[1]The carrier-envelope phase does not change from pulse to pulse, independent of the carrier-envelope phase of the generating NIR pulse.

photons before the interaction must equal the total momentum of all photons after the interaction. This can be expressed mathematically as

$$\hbar\Delta\boldsymbol{k} = \hbar\left(\sum_m \boldsymbol{k}_m^{\text{before}} - \sum_n \boldsymbol{k}_n^{\text{after}}\right) = 0, \tag{3.6}$$

where $\hbar\Delta\boldsymbol{k}$ is the net change in photon momentum and $k = \frac{2\pi}{\lambda}$ is the magnitude of the wave vector $\boldsymbol{k}$ with the wavelength $\lambda$. In the case of (intra-pulse) difference-frequency generation, this condition becomes

$$\Delta\boldsymbol{k} = \boldsymbol{k}_1 - (\boldsymbol{k}_2 + \boldsymbol{k}_3) = 0. \tag{3.7}$$

In the wave description of light, momentum conservation corresponds to constructive interference of the elementary waves generated at different points in space and time, leading to maximal conversion efficiency. The art of achieving this condition is called **phase matching**.

The main obstacle to phase matching is dispersion, i.e. the frequency dependence of the refractive index $n$, which modifies the wave vector via

$$k = \frac{2\pi}{\lambda} = \frac{2\pi n}{\lambda_0} = \frac{\omega n}{c}, \tag{3.8}$$

where $\lambda_0$ is the wavelength in vacuum, $c$ the speed of light and $\omega$ the angular frequency. In many materials, normal dispersion occurs, meaning that the refractive index increases as a function of frequency. This makes simultaneous phase matching, equation 3.7, and energy conservation challenging. To overcome this challenge, several techniques have been developed – most notably quasi-phase matching and critical phase matching. In quasi-phase matching [Bla07, Neg11, Hek20], the crystal length is chosen such that the phase difference between the generated waves is small enough to allow for constructive interference over the entire crystal length. Critical phase matching [Hub00, Sel08] relies on the polarisation dependence of the refractive index in birefringent crystals. This allows to tune the phase-matching condition by tilting the crystal axes with respect to the propagation direction.

To meet all of the criteria for our source, i.e. generating carrier-envelope-phase stable THz pulses with high average power at MHz repetition rates, we employ a different

phase-matching technique – tilted-pulse-front optical rectification in lithium niobate ($LiNbO_3$) – which has proven to be the most efficient approach for THz generation at MHz repetition rates and microjoule pulse energies [Mey20].

### 3.2.2 Tilted-pulse-front optical rectification

In critical phase matching [Hub00, Sel08], the group velocity of the generating NIR pulse is matched to the phase velocity of the generated THz pulses. However, this requirement cannot be fulfilled in certain $\chi^{(2)}$ nonlinear crystals owing to a significant velocity mismatch. In specific materials – most prominently in lithium niobate ($LiNbO_3$) – tilted-pulse-front optical rectification [Heb02, Ste03, Heb04, L'h07a, L'h07b] offers an effective alternative. Lithium niobate is particularly suited for optical rectification due to its large nonlinear coefficient of $168\,\mathrm{pm\,V^{-1}}$ and high damage threshold exceeding $100\,\mathrm{GW\,cm^{-2}}$ [Fül20]. The essential requirement for tilted-pulse-front optical rectification is that the phase velocity of the generated THz pulses, $v_{\mathrm{ph,THz}}$, is lower than the group velocity of the generating NIR pulses, $v_{\mathrm{gr,NIR}}$. When a NIR light pulse travels through such a $\chi^{(2)}$ crystal, THz elementary waves (blue dashed lines in Fig. 3.3) are generated. The THz phase fronts (blue lines), formed by the superposition of the elementary waves emitted at different instants in time (red dashed lines), interfere destructively both in the propagation direction of the NIR pulse (Fig. 3.3**a**) and along the direction defined by the angle $\gamma$ with respect to $\boldsymbol{v}_{\mathrm{gr,NIR}}$ (Fig. 3.3**b**). Here, $\gamma$ is the Cherenkov angle, which is given by

$$\cos\gamma = \frac{v_{\mathrm{ph,THz}}}{v_{\mathrm{gr,NIR}}}. \tag{3.9}$$

Reducing the NIR beam waist to below the THz wavelength decreases the maximal phase difference $\varphi$ between the phase fronts propagating at the angle $\gamma$ to below $2\pi$. This suppresses destructive interference, allowing a THz wavefront to propagate in this direction (Fig. 3.3**c**). This configuration is known as Cherenkov THz generation [Ste05, Bak07, L'h07a, L'h07b]. Yet the tight focusing required for this technique limits the usable NIR pulse energies. Additionally, owing to the symmetry of the Cherenkov generation geometry, only half of the generated THz power is coupled out to one side.

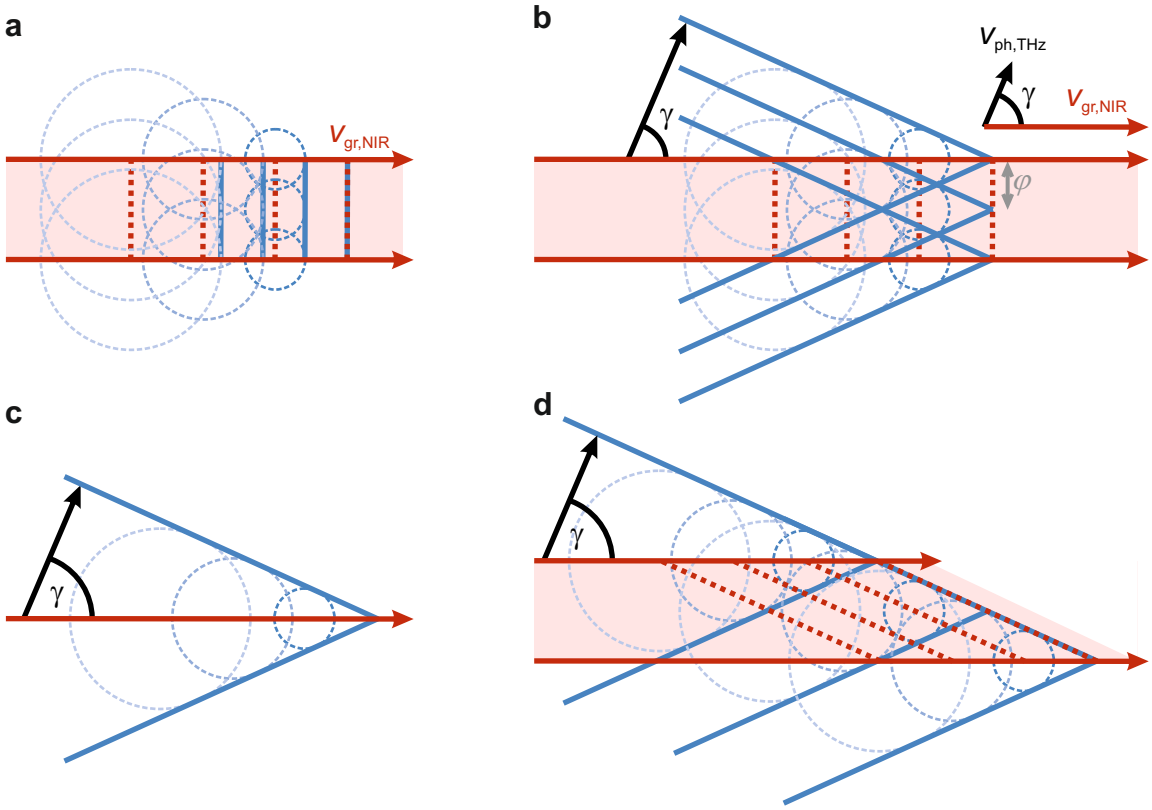


**Figure 3.3 |** Tilted-pulse-front optical rectification. **a**, In a $\chi^{(2)}$ nonlinear crystal where the group velocity at NIR frequencies $\boldsymbol{v}_{\mathrm{gr,NIR}}$ significantly exceeds the THz phase velocity $\boldsymbol{v}_{\mathrm{ph,THz}}$, the generated THz phase fronts (blue lines) formed by the superposition of elementary waves (blue dashed lines) generated at different instants in time (red dashed lines) interfere destructively along the propagation direction of the NIR pulses. **b**, Additional THz phase fronts propagate at an angle $\gamma$ relative to the NIR propagation direction. Owing to the finite beam waist of the generating NIR pulses (pale red), these phase fronts accrue a phase difference $\varphi$ during propagation. This also leads to destructive interference along this propagation direction. **c**, Reducing the NIR beam waist to below the THz wavelength decreases $\varphi$, preventing complete destructive interference, and allowing a THz wavefront to propagate in this direction. This is referred to as the Cherenkov generation geometry. **d**, To direct the generated THz intensity to one side and allow for larger generation cross sections, the NIR pulses' intensity front (red dashed lines) is tilted. This leads to constructive interference of all the THz phase fronts generated within the NIR beam waist along the $\gamma$-direction on one side (top) and destructive interference on the other side (bottom).

It is possible to circumvent the limitations of the Cherenkov geometry by aligning the NIR intensity fronts with the THz phase fronts. This can be achieved by tilting the NIR pulse's intensity fronts by the angle $\gamma$, as shown in Fig. 3.3**d**. This leads to constructive interference on one side (top) where the generated THz phase fronts propagate at an angle $\gamma$ relative to $\boldsymbol{v}_{\mathrm{gr,NIR}}$, whereas on the other side (bottom), the THz elementary waves interfere destructively. By transferring energy only to one propagation direction and allowing for generation along larger cross-sections and thus with higher pulse energy, this generation scheme, called tilted-pulse-front optical rectification, is extremely efficient. With millijoule pump-pulse energies, conversion efficiencies of up to 3.8% have been reported in cryogenically cooled lithium niobate [Hua13, Fül20]. Cryogenic cooling reduces the THz absorption in lithium niobate [Pál05], enhancing the conversion efficiency. Even at MHz repetition rates and microjoule pulse energies, a record 66 mW from a few-cycle source driven by a table-top laser was reported [Mey20].

In our experiment, we perform tilted-pulse-front optical rectification as shown in Figs. 3.4 and 3.1 (**THz generation** panel). To tilt the NIR pulse front, we make use of the fact that angular dispersion generates a pulse-front tilt [Heb96]. We obtain the angular dispersion by using a transmissive diffraction grating (grating constant: $1600\,\mathrm{mm}^{-1}$) operating at an incidence angle of $\alpha = 55.5°$, which transmits 94% of optical power into the first diffraction order at an angle of 55.5°. If a diffraction grating is operated in Littrow configuration, where the incoupling angle $\alpha$ equals the outcoupling angle, the pulse-front tilt generated by the grating, $\gamma_{\mathrm{grating}}$, is given by [Tót23]

$$\tan(\gamma_{\mathrm{grating}}) = 2\tan(\alpha). \tag{3.10}$$

For our grating, this equates to a pulse-front tilt of $\gamma_{\mathrm{grating}} = 71°$. As angular dispersion also introduces a group velocity dispersion, the grating has to be imaged into the crystal, such that all spectral components overlap in space and time within the crystal, in the so-called colour focus. After magnification with a magnification factor $M$, and diffraction at the lithium niobate crystal's surface, the pulse-front tilt $\gamma$ within the crystal is calculated as [Tót23]

$$\gamma = \tan^{-1}\left(\frac{1}{M n_{\mathrm{gr,NIR}}}\tan(\gamma_{\mathrm{grating}})\right), \tag{3.11}$$

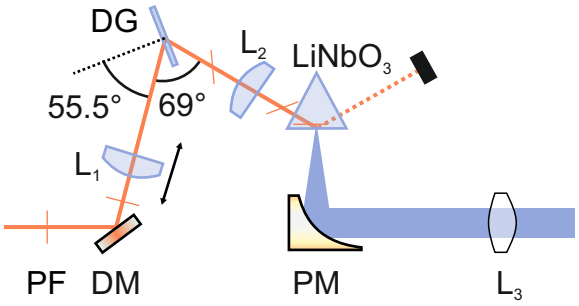


**Figure 3.4 |** Experimental realisation of tilted-pulse-front optical rectification. The pulse front (PF) of the NIR pulses (orange) is tilted by a diffraction grating (DG) and imaged via a lens ($L_2$) into the lithium niobate crystal ($LiNbO_3$), where optical rectification generates THz pulses (blue). The first lens ($L_1$) can be translated to set the peak intensity inside the crystal. Via a parabolic mirror (PM) and a custom Teflon lens ($L_3$) the THz pulses are first collimated and then focused onto the incoupling parabolic of the microscope (see Fig. 3.1). DM: Dielectric mirror.

where $n_{\mathrm{gr,NIR}}$ is the NIR group refractive index in the lithium niobate crystal. To match the pulse-front tilt with the phase matching condition (equation 3.9), we choose $M = 0.67$. We obtain this magnification factor by using a lens with a focal length of $f = 50\,\mathrm{mm}$ to image the grating (object distance: 124.6 mm) into the crystal (image distance: 83.5 mm). This yields the desired condition of $\gamma = 63°$.

The crystal consists of stoichiometric lithium niobate with a magnesium oxide doping of 1%, which reduces photorefractive effects and increases the damage threshold [Pál04], and it is tailored for high-power applications: It is cut such that all transmissions occur perpendicular to the crystal's surfaces. Due to the noncollinear nature of the THz generation process, the THz radiation can exit the crystal while the residual NIR light experiences total internal reflection before being directed to a beam dump after exiting the $LiNbO_3$ prism. Both surfaces through which the NIR pulses are transmitted have an anti-reflection coating.

We cool the crystal to liquid nitrogen temperatures, allowing us to generate THz with the full 50 W of the laser fundamental and increasing the conversion efficiency. We tune the focusing conditions (by translating $L_1$ as indicated in Fig. 3.4) to achieve a peak intensity of $\sim 8\,\mathrm{GW\,cm^{-2}}$, which was shown to be optimal at MHz repetition rates and microjoule pulse energies [Mey20]. At a repetition rate of 5 MHz, we achieved an average THz power of $\sim 20\,\mathrm{mW}$.

Owing to the anisotropy of the THz generation process, where the generation only acts like a point source in the vertical axis, a single parabolic mirror is insufficient for collimation of the THz radiation. To correct for this, we employ a custom-designed Teflon lens, which is cylindrical on the entrance side with a radius of curvature of 935.25 mm, collimating the horizontal axis of the beam, and spherical on the exit side with a radius of curvature of −326.25 mm. This focuses the THz radiation onto the incoupling parabolic mirror of the microscope (see Fig. 3.1).

### 3.2.3 Field-resolved detection

To trace the coherently scattered electric field waveforms with subcycle resolution, we use **electro-optic sampling** (EOS, Fig. 3.5 & bottom right panel in Fig. 3.1). Acting as an "oscilloscope for light", EOS is routinely employed to sample THz to mid-infrared waveforms [Wu95, Hub00, Küb04, Kam07, Kno18] and has recently even been extended into the near-infrared and visible spectral regions [Kei16, Rid22]. EOS stroboscopically samples phase-locked electric field waveforms with even shorter, so-called gate pulses. Both pulses are spatially and temporally overlapped in a $\chi^{(2)}$ nonlinear crystal – in our case a $\langle 110 \rangle$-cut gallium phosphide (GaP) crystal with a thickness of 2 mm. This gives rise to the Pockels effect, also known as the linear electro-optic effect. Through the Pockels effect, the refractive index of a $\chi^{(2)}$ crystal changes linearly with an applied electric field – here, the electric field of the THz pulse. This induces a birefringence in the electro-optic crystal which is imprinted onto the polarisation state of a near-infrared gate pulse. Alternatively, this process can be understood as a combination of sum- and difference-frequency generation between the THz and gate pulses, which oscillate at the frequencies $\nu_{\mathrm{THz}}$ and $\nu_{\mathrm{gate}}$, respectively. There, new photons at the frequencies $\nu_{\mathrm{gate}} \pm \nu_{\mathrm{THz}}$ with a polarisation perpendicular to the gate pulses are generated. This induces ellipticity in the polarisation state of the NIR gate pulses.

To detect the THz-induced ellipticity of the gate pulse's polarisation with high sensitivity, we employ a balanced detection scheme. This consists of a quarter-wave plate, a Wollaston prism and two photodiodes. The quarter-wave plate sets the gate polarisation to be circular in the absence of a THz field, such that the two polarisation components split by the Wollaston prism and detected by the photodiodes

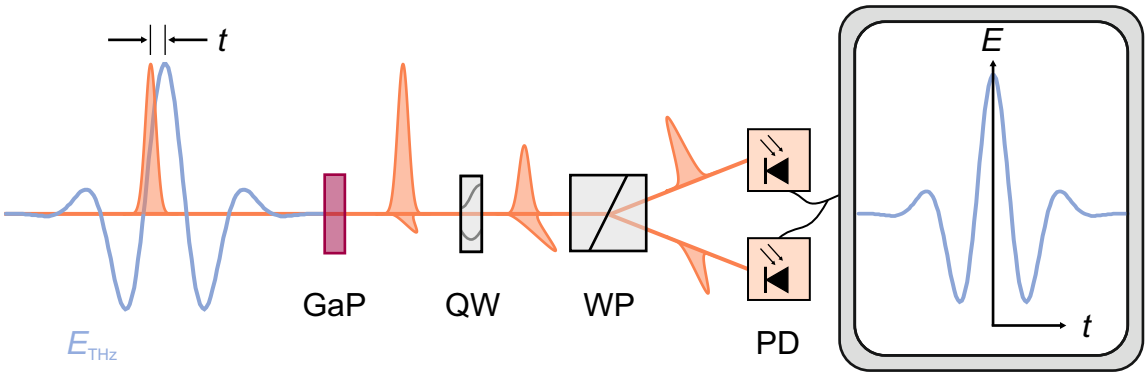


**Figure 3.5 |** Electro-optic sampling. A THz electric field waveform ($E_{\mathrm{THz}}$) and a NIR gate pulse (orange) are overlapped in a $\chi^{(2)}$ nonlinear crystal, gallium phosphide (GaP). Via the Pockels effect, the instantaneous field strength of $E_{\mathrm{THz}}$ is imprinted onto the polarisation of the gate pulse which is read out via a quarter-wave plate (QW), a Wollaston prism (WP) and two balanced photodiodes (PD). Changing the delay time $t$ between both pulses while measuring the differential signal on the PDs reveals the electric field waveform $E_{\mathrm{THz}}(t)$.

are balanced. By measuring the differential signal between the two photodiodes, we detect THz-induced changes in the polarisation while suppressing common noise. Since the $\chi^{(2)}$ nonlinearity responds instantaneously and the gate pulses are much shorter than an oscillation cycle of the THz pulses, we can stroboscopically sample the THz electric field waveform by varying the delay time between the THz and gate pulses. We achieve this by translating a mechanical delay stage in the gate beam path (**Gate** panel in Fig. 3.1), changing the relative timing between THz and gate pulses. Depending on the experiment, we either mechanically chop the THz pulses or modulate the scattered light via the tapping tip. Using a lock-in detection scheme, such a setup allows to routinely achieve signal-to-noise ratios limited by the shot noise.

To detect the generated far-field THz transients we mechanically chop the THz beam for lock-in detection and perform electro-optic sampling. The recorded far-field THz waveform is depicted in Fig. 3.6**a**, featuring a pulse duration of 0.7 ps (measured as the full width at half maximum, FWHM, of the intensity envelope). Via Fourier transform, we retrieve the spectral amplitude (Fig. 3.6**b**) with a centre frequency of 0.94 THz, a FWHM bandwidth of 0.98 THz and measurable spectral components

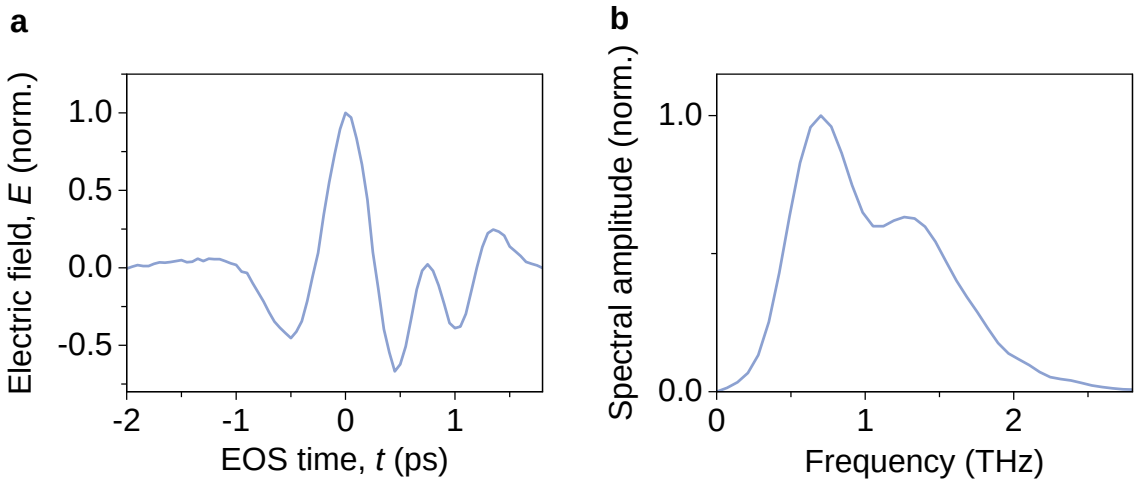


**Figure 3.6 | a**, THz transient generated via tilted-pulse-front optical rectification in a cryogenically cooled lithium niobate crystal, and electro-optically detected in a ⟨110⟩-cut GaP crystal with a thickness of 2 mm. It features a pulse duration (FWHM of the intensity envelope) of 0.7 ps. **b**, The spectral amplitude reaches its maximum at 0.7 THz, with another kink at 1.26 THz. It reaches a bandwidth of 0.98 THz (FWHM of the spectral amplitude) at a centre frequency of 0.94 THz. Figure adapted from [Sid24].

ranging from 0.1 THz to 2.6 THz. The spectral amplitude reaches its maximum at 0.7 THz with a second peak at 1.26 THz.

## 3.3 A customized low-temperature, ultra-high vacuum scanning probe microscope

To bring SNOM to the most stable configuration, we adapted the scan head design of a commercially available tip-enhanced Raman spectroscopy microscope, which operates at cryogenic temperatures down to 10 K, and in a UHV environment at pressures of about $10^{-10}$ mbar. In collaboration with the manufacturer, we optimised the vibration-isolated scan head for optical coupling by integrating custom parabolic mirrors with a large numerical aperture (NA = 0.4), which allow us to obtain atomically strong THz fields in the tip-sample junction.

In conventional SNOM, metal-coated silicon cantilevers are typically used [Che19b, Hil25]. These cantilevers lack the stiffness required for atomic-resolution AFM and

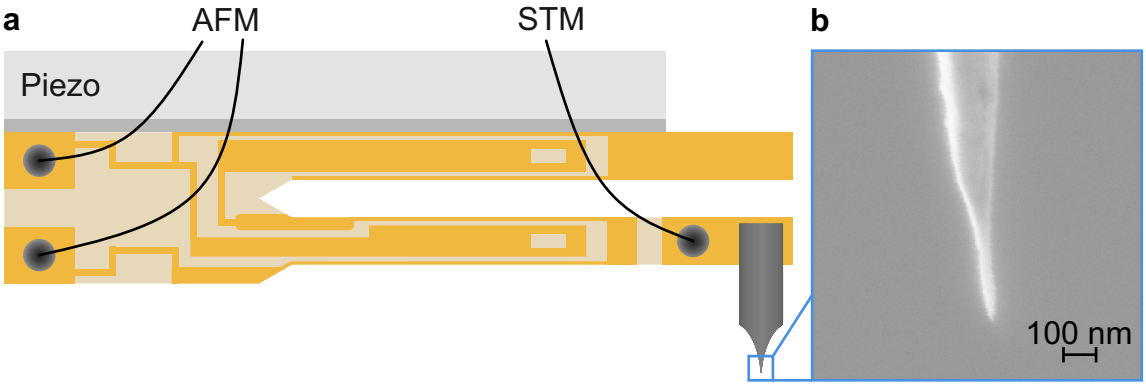


**Figure 3.7** | qPlus AFM sensor with tungsten tip. **a**, A qPlus sensor consists of a stiff quartz tuning fork (beige) which is driven vertically by an excitation piezoelectric crystal (light grey) that is separated from the tuning fork by an insulating layer (grey). The electrical contacts (golden) allow for simultaneous AFM and STM operation. An electrochemically etched tungsten tip (dark grey) is glued to the free-standing prong of the tuning fork. **b**, Scanning electron microscopy image of the apex of the tungsten tip.

do not allow for STM experiments. For simultaneous atomic-scale AFM and STM measurements, we employ qPlus sensors [Gie03, Gie19]: A tungsten tip is attached to the end of the free prong of a stiff quartz tuning fork glued to an insulating layer (Fig. 3.7**a**). An excitation piezo is driven to shake the sensor vertically, resonantly driving a tip-tapping motion (resonance frequency: $\sim$20 kHz), which is read out via the AFM contacts on the piezoelectric tuning fork. Forces acting on the tip alter the sensor's resonance frequency while a phase-locked loop ensures resonant driving. The shift of the resonance frequency serves as a measure of force and thus can be used as a feedback parameter for AFM imaging. The tapping amplitude is maintained at a constant value by a second control loop. The high stiffness of the quartz tuning fork allows for exceptionally small tapping amplitudes in the picometre range, enabling atomic-resolution AFM. An STM contact wire is fixed directly next to the tip. The wire is connected to the STM preamplifier, enabling the measurement of tunnelling currents flowing between tip and sample. For AFM and STM imaging, the sample is scanned via a piezo actuator, which allows for picometre-precise positioning.

Achieving high-resolution STM and AFM measurements requires atomically sharp tips. To fabricate such tips with a small apex radius of curvature, we start with

tungsten wires with a thickness of 125 µm and use electrochemical etching, following the procedure described in reference [Kul03]. This process produces tips like the one shown in Fig. 3.7**b**, which depicts a scanning electron microscopy image of a tip apex. For an electron microscopy image of the macroscopic tip shape, please refer to Fig. 4.14**b**. To remove any tungsten oxide on the tip's surface, we briefly dip it into highly concentrated hydrofluoric acid before immediately transferring it to the UHV environment to prevent further oxidation.

At the end of section 2.2, I posed the question whether we can achieve subcycle atomic-scale resolution by combining the strengths of lightwave-STM and subcycle SNOM. We are now in the unique position to answer this question, since we (i) developed a state-of-the-art high-power THz source operating at MHz repetition rates using tilted-pulse-front optical rectification in lithium niobate and (ii) have high-NA optical access to a low-temperature UHV scanning probe microscope which allows for picometre-precise control over the tip-sample separation.
The next chapter explores the limits of spatial resolution in SNOM by harnessing the capabilities of this unique setup. I will show that, in the limit of atomic-scale tapping amplitudes and atomic-scale tip-sample separations, the transient electric field of the THz waveform drives tunnelling currents which lead to the emission of coherent light. Detecting this light with EOS allows us to trace atomically confined, subcycle tunnelling currents directly in the time domain.

Chapter 4

# Near-field optical tunnelling emission microscopy

*This chapter encompasses the results published in* Thomas Siday*, Johannes Hayes*, Felix Schiegl* *et al.*, "All-optical subcycle microscopy on atomic length scales", Nature **629**, 329–334 (2024). (*These authors contributed equally.) *The results shown here are the outcome of a group effort together with Thomas Siday, Felix Schiegl, Fabian Sandner, Peter Menden, Valentin Bergbauer, Martin Zizlsperger, Svenja Nerreter, Sonja Lingl, Jascha Repp, Jan Wilhelm, Markus Huber, Yaroslav Gerasimenko & Rupert Huber. For a detailed breakdown of individual contributions, please refer to the original publication, hereafter cited as reference* [Sid24].

Macroscopic functionalities of condensed matter systems arise from a complex interplay of microscopic elementary dynamics. This has driven the persistent pursuit of optical microscopy at the ultimate time and length scales. The fundamental limit of conventional optical microscopy, the diffraction limit, can be circumvented by exploiting optical nonlinearities, which is the fundamental concept of super-resolution microscopy [Hel07]. Near-field microscopy (section 2.1) uses linear light-matter interaction with tip-confined evanescent light fields [Bet92, Zen95, Kno99]. This has enabled a spatial resolution of a few nanometres irrespective of the illumination wavelength, providing access to the nanoworld in motion [Qaz07, Fei12, Che12, Eis14, Lun17, Hub17, Sun18, Jia19, Esm19, Hu20, Zha21b, Don21, Zha21a, Ste21, Pla21,

Sid22, Mei23, Mei24, Ziz24, Ang25]. Yet the atomic scale has remained out of reach owing to the nanometre size of the tip apex radius of curvature [Nov12].
This chapter details how we exploit angstrom-scale nonlinearities in tip-confined fields to promote optical near-field microscopy to atomic-scale spatial resolution while retaining subcycle femtosecond time resolution. In section 4.1, I will outline how we discovered an entirely unforeseen non-classical near-field response, which oscillates in phase with the vector potential of light, and is confined to significantly smaller spatial dimensions than the conventional near-field signal. This ultrafast signal, characterised by an optical phase delay of $\sim\pi/2$ with respect to the conventional near fields, decays on picometre length scales (section 4.2). Using both a semiclassical and a quantum model based on time-dependent density functional theory, we show that this signal originates from a polarisation formed by ultrafast a.c. tunnelling currents driven by the optical near fields (section 4.3).
I highlight the capabilities of our novel optical concept in section 4.4 by showcasing how we image nanometre-sized defects which are hidden from atomic force microscopy. To the best of our knowledge, our new technique is the first to provide access to subcycle atomic-scale spectroscopy (section 4.5) and it even allows us to clock atomically-confined ultrafast current transients on a semiconducting van der Waals material directly in the time domain (section 4.6). Our results open the door to exploring quantum light–matter interaction and electronic dynamics on the shortest possible length and time scales in conducting and even insulating quantum materials.

## 4.1 Near-field microscopy at atomic-scale tip-sample distances

Atomic protrusions at the scanning probe's apex (inset in Fig. 4.1) are key to the extreme spatial resolution of both atomic force microscopy (AFM) [Bin86, Gie03] and scanning tunnelling microscopy (STM) [Bin82, Che21]. In tip-based scattering near-field optical microscopy (section 2.1), however, the spatial resolution is governed by the size of the dipole induced within the tip's apex. The extent of this dipole is on the order of the tip-apex radius of curvature [Nov12]. Typically, this radius is found to be in the tens of nanometres, raising the question: *Why does the radius of curvature*

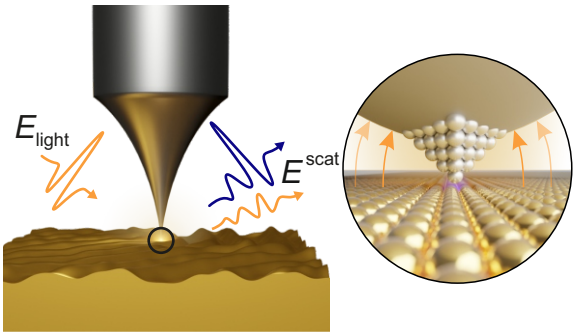


**Figure 4.1 |** Near-field microscopy at angstrom-scale tip-sample distances. We couple THz waveforms $E_{\text{light}}$ to the apex of an atomically sharp tungsten tip placed above an atomically clean Au(111) surface and record the scattered waveforms $E^{\text{scat}}$ with subcycle resolution via EOS. We focus on the key question, how the atomic-scale features of the tip's apex (inset) affect the scattered radiation. Figure adapted from [Sid24].

*not correspond to the radius of the most frontier atom of the tip, which would enable atomic resolution?* In near-field microscopy, the role of atomic protrusions remains poorly understood, in particular, how tunnelling electrons could potentially alter the recorded near-field signals. We set out to explore these questions with our novel experimental setup described in chapter 3. The key here is that using the stiff qPlus AFM sensor [Gie03, Gie19] with a sharp tungsten tip, we can control the tip-sample separation with picometre precision. To be able to exploit this level of control, we operate in UHV and at cryogenic temperatures.

To explore atomic-scale nonlinearities, we couple the strong THz waveforms $E_{\text{light}}$ shown in Fig. 3.6 to the apex of our sharp tungsten tip (Fig. 4.1) which is placed above an atomically flat and clean Au(111) surface. With EOS, we record the scattered waveforms $E^{\text{scat}}$ with subcycle resolution. To achieve high signal-to-noise ratios while keeping peak THz field strengths on the order of $1\,\text{kV}\,\text{cm}^{-1}$, we tune the pulse repetition rate of our laser to 13.7 MHz.

We begin by examining whether the frontier atoms of our tip can influence near-field scattering when brought within a few angstroms above the flat Au(111) surface. To test this, we tap the tip with an amplitude of $A = 25\,\text{nm}$ and trace the scattered waveforms demodulated at the second harmonic of the tip-tapping frequency $\nu_{\text{tap}}$. As we approach the tip to the sample, we first observe a typical near-field response, with the amplitude of the scattered light increasing exponentially with decreasing tip-sample separation (Fig. 4.2**a**). The peak of the scattered waveforms $\hat{E}_2^{\text{scat}}$ is plotted

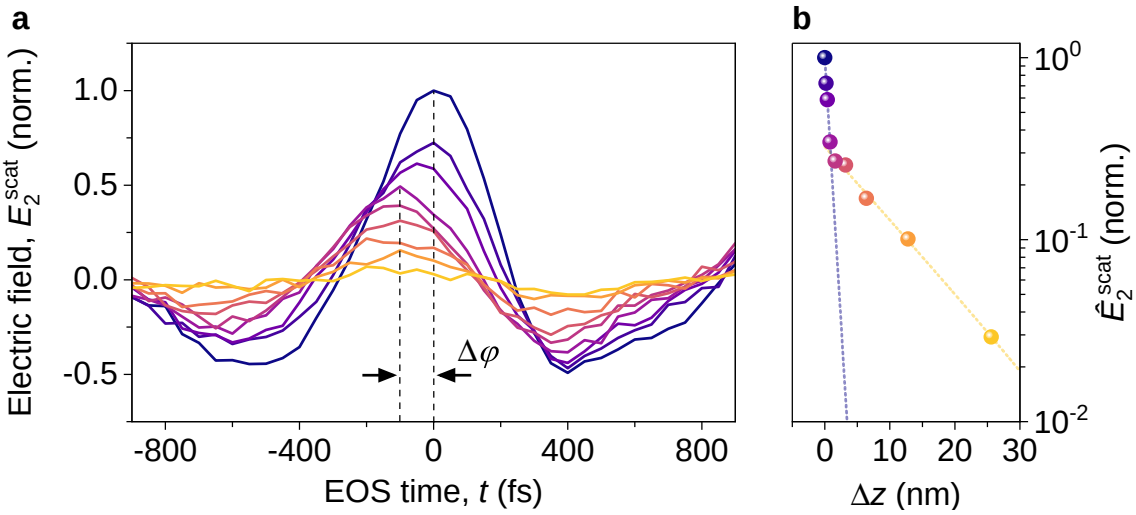


**Figure 4.2 |** Near-field microscopy at angstrom-scale tip-sample distances. **a**, Scattered waveforms demodulated at the second harmonic of the tip-tapping frequency $E_2^{\mathrm{scat}}$, measured while approaching the tip to the sample (the relative tip-sample separation $\Delta z$ is colour-coded and shown in **b**). Panel **b** shows the peak of the scattered waveforms $\hat{E}_2^{\mathrm{scat}} = E_2^{\mathrm{scat}}(t = 0\,\mathrm{fs})$ as a function of $\Delta z$. At large $\Delta z$, the amplitude of the scattered waveforms increases exponentially with decreasing $\Delta z$, exhibiting a decay constant typical for SNOM (dashed yellow line in **b**). When approaching to $\Delta z \leq 1\,\mathrm{nm}$, $E_2^{\mathrm{scat}}$ accrues a distinct phase shift $\Delta\varphi$ of almost $\pi/2$. The much shorter decay constant (blue dashed line in **b**) indicates a new regime of light-matter interaction. The dashed lines represent independent exponential fits for the decay of the near field, as well as the atomic-scale contribution to the measured signal. Tapping amplitude: 25 nm. Incoupled peak far-field electric field strength: $\hat{E}_{\mathrm{light}} = 1.3\,\mathrm{kV\,cm^{-1}}$. At closest approach, on average about 900 electrons per pulse are rectified. Figure adapted from [Sid24].

in Fig. 4.2**b** as a function of the relative tip-sample separation $\Delta z$ (see footnote [1]). There, the initial decay constant at $\Delta z \geq 1\,\mathrm{nm}$ lies in the tens of nanometres (yellow dashed line: exponential fit), as expected for SNOM [Nov12, Moo20]. Yet, when approaching the tip to the sample very closely ($\Delta z \leq 1\,\mathrm{nm}$), the amplitude of the scattered signal is significantly boosted and the scattered waveforms accrue a distinct phase shift $\Delta\varphi$ of almost $\pi/2$. When tracing the peaks of these transients (Fig. 4.2**b**), we observe a much shorter decay constant (blue dashed line: independent exponential fit). This strikingly different behaviour indicates that we have entered a completely new regime of light-matter interaction and that this signal might stem from an entirely different source.

**Dependence of scattered near fields on the demodulation order.** In SNOM, the decay of the scattered signal as a function of $\Delta z$ depends on the demodulation order [Kno00, Moo20]: Owing to the fact that the near-field interaction features a non-linear distance dependence, the decay length decreases with increasing demodulation order.

We now compare the scattered waveforms recorded at different demodulation orders (Fig. 4.3) but measured simultaneously with Fig. 4.2. Demodulating at the tapping frequency $\nu_{\mathrm{tap}}$ (Fig. 4.3**a**) results in a more gradual signal increase as a function of the relative tip-sample separation $\Delta z$ in comparison with Fig. 4.2**a**, and the phase only shifts by a fraction of the shift observed before. In contrast, when demodulating at $3\nu_{\mathrm{tap}}$ (Fig. 4.3**b**), the phase shift already occurs at larger $\Delta z$ and the scattered field's amplitude changes more drastically over the range of tip-sample distances.

We can explain this behaviour in the following way: The scattered fields consist of two distinct contributions: (i) a conventional mesoscopic near field, and (ii) a novel short-ranged interaction. The conventional near field exhibits a weaker nonlinear distance dependence compared to the novel signal. Consequently, their relative contributions to the different harmonic constituents evolve differently. A stronger nonlinearity increases the relative contributions of the higher harmonics (compare Fig. 2.1**b**). Thus, the signal demodulated at $3\nu_{\mathrm{tap}}$ is primarily formed by the novel short-ranged signal. This is evident in two ways. First, a pronounced phase shift

[1] $\Delta z$ refers to the relative tapping-cycle-averaged tip position. Note that $\Delta z = 0$ corresponds to the closest approach in the respective measurement and does not indicate a point contact.

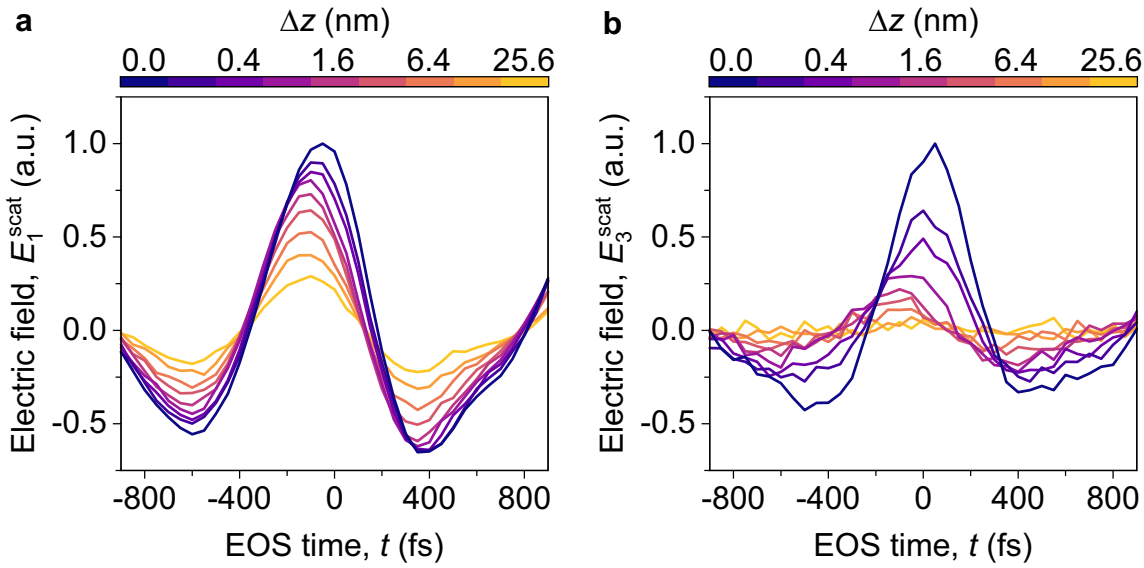


**Figure 4.3** | Scattered waveforms demodulated at $\nu_{\mathrm{tap}}$ (**a**) and $3\nu_{\mathrm{tap}}$ (**b**) measured simultaneously with Fig. 4.2. Demodulating at the tapping frequency $\nu_{\mathrm{tap}}$ leads to a more gradual increase in signal amplitude as a function of the tapping-cycle-averaged tip-sample separation $\Delta z$, compared to Fig. 4.2**a**, and the corresponding phase shift is significantly smaller. In contrast, when demodulating at $3\nu_{\mathrm{tap}}$, the phase shift occurs at larger tip-sample distances, and the scattered field's amplitude exhibits a more pronounced variation over the measured range. Figure adapted from [Sid24].

is observed already at relatively large $\Delta z$, indicating that the novel short-ranged contribution dominates the signal early on. Second, because this novel signal is confined to very small tip-sample separations, its amplitude rapidly diminishes as $\Delta z$ increases, leaving only a weak conventional near-field signal at larger distances. In contrast, measurements at $\nu_{\mathrm{tap}}$ are dominated by the conventional near field, as reflected by the minimal phase variation across the same range of $\Delta z$.
This further highlights the highly nonlinear distance dependence of our new signal, supporting the hypothesis that this could be a new regime of light-matter interaction.

## 4.2 Picometric near-field decays

The large tapping amplitude of $A = 25\,\mathrm{nm}$ used in section 4.1 inevitably mixes both mesoscopic and atomic-scale contributions to the near-field signal as it spans several orders of magnitude in tip-sample separation over a single tapping cycle. Nevertheless, the optical phase is clearly influenced when the tip apex approaches atomic proximity to the sample surface.
To investigate this extremely short-ranged interaction at its intrinsic length scale, we reduce the tapping amplitude to 1 nm and approach the surface again. A reduced tapping amplitude alters the relative contributions of the two signal sources. Conventional near fields decay on the length scale of the tip's apex radius of curvature ($\sim 10\,\mathrm{nm}$). Thus, by tapping the tip at an amplitude significantly smaller than the tip radius, the modulation of the near fields is reduced and their impact on the measured signal is suppressed. Yet, considering the short decay length of the novel phase-shifted signal obtained in Fig. 4.2**b**, this signal should still be modulated with such a small tapping amplitude.
As we approach the tip sufficiently close to the sample, a strong transient signal emerges in all three measured harmonics (blue spheres, Fig. 4.4), despite the tapping amplitude being orders of magnitude smaller than in conventional near-field microscopy. Remarkably, at the shortest tip-sample separation, a current emerges even without any static bias voltage applied. This current originates from electrons driven by the ultrafast bipolar transient bias of the THz pulse. The THz bias drives electron tunnelling back and forth through the tunnelling barrier between tip and sample when the frontier atoms of the tip are brought close enough to the sample for tunnelling to

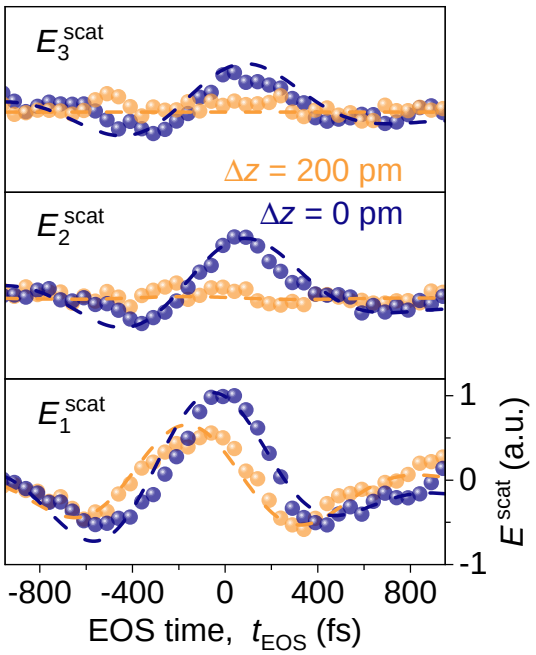


**Figure 4.4 |** Scattered transients at the first three harmonics measured at a tapping amplitude of 1 nm. The dark blue curves show the case of an approached tip, where on average 140 electrons are rectified per pulse ($\Delta\nu_{tap} = -4.8$ Hz, in-coupled electric field strength $\hat{E}_{light} = 1.3\,\mathrm{kV\,cm^{-1}}$). The orange curves show the scattered signal after retracting the tip by 200 pm from the sample. The semiclassical model detailed in section 4.3 predicts the dashed curves which are overlaid. Figure adapted from [Sid24].

set in. Electrons which are rectified owing to asymmetries in the sample's $J$-$V$ characteristics contribute to a time-averaged net current $\langle J_{lw}\rangle$, as explained in section 2.2, which we measure electronically. This is exactly the current which forms the basis for lightwave-STM [Coc13, Coc16, Jel17, Luo20, Pel21, Gar22, Wan22, Ara22, Roe24] and lightwave electronic nanodevices [Bio21, Bor23]. Since the tip is tapped, the measured rectified current $\langle J_{lw}\rangle$ is averaged over the tapping cycle.

When retracting the tip by only 200 pm (orange spheres, Fig. 4.4), where no sizeable time-averaged lightwave-driven tunnelling current $\langle J_{lw}\rangle$ is observed, we detect no near-field signals, except for a residual signal in the first harmonic. Comparing this residual signal to the transients at higher harmonics with an approached tip again reveals a distinct phase shift of $\sim\pi/2$. I would like to emphasize here, that this indicates that our phase-shifted optical signal decays within only 200 pm, about one atomic diameter[2], just like the tunnelling current. This strikingly strong confinement of the novel signal, comparable to that of the tunnelling current, suggests a direct link between the phase-shifted signal and the ultrafast tunnelling dynamics.

[2]The lattice constant of Au(111) is 288 pm [Dar02].

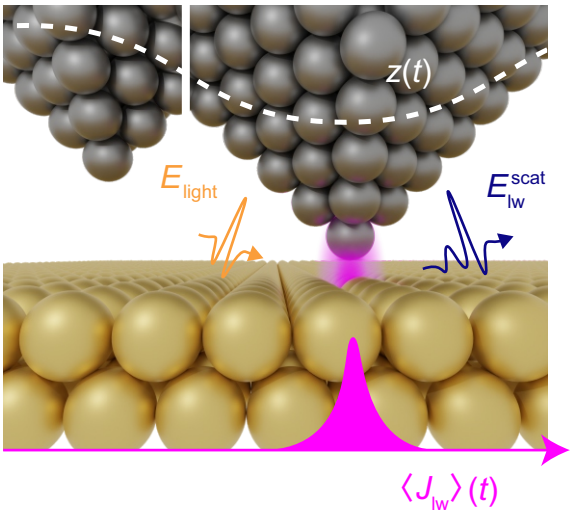


**Figure 4.5 |** Schematic of the tunnelling current and light emission during the tapping cycle. The dashed white line indicates the tip-position $z(t)$ during the tapping cycle. At the position of closest approach, the tunnelling probability is maximal. There, the tunnelling current (magenta) driven by the incoming electric field waveform $E_{\mathrm{light}}$, and the emitted $E_{\mathrm{lw}}^{\mathrm{scat}}$ also reach their maximum. By reducing the tapping amplitude to only 200 pm, approximately one atomic diameter, the far-field and even conventional near-field contributions are suppressed. Figure adapted from [Sid24].

According to Maxwell's equations, time-dependent currents $\boldsymbol{J}$ emit light, since they enter as a source term in the wave equation for the electric field $\boldsymbol{E}$ [Jac62]:

$$\left(\Delta - \frac{1}{c^2}\frac{\partial^2}{\partial t^2}\right)\boldsymbol{E}(\boldsymbol{r},t) = \mu_0 \frac{\partial}{\partial t}\boldsymbol{J}. \tag{4.1}$$

Here $\Delta$ is the Laplace operator, $\boldsymbol{r}$ the spatial coordinate, $c$ the speed of light and $\mu_0$ the vacuum permeability. In our case, the ultrafast lightwave-driven tunnelling currents $J_{\mathrm{lw}}$ emit transient electric field waveforms $E_{\mathrm{lw}}^{\mathrm{scat}}$.

We propose that our detection scheme should be sensitive to these emitted transients since tapping the tip modulates the emission process. Throughout the tip's tapping cycle (Fig. 4.5), lightwave-driven tunnelling predominantly occurs when tip and sample are in close proximity. When the incoming waveform $E_{\mathrm{light}}$ drives an ultrafast tunnelling current $J_{\mathrm{lw}}$ between tip and sample, $J_{\mathrm{lw}}$, according to equation 4.1, causes the emission of $E_{\mathrm{lw}}^{\mathrm{scat}}$. Both $J_{\mathrm{lw}}$ and $E_{\mathrm{lw}}^{\mathrm{scat}}$ reach their maximal strength at the point of closest approach ($\Delta z = 0$).

Asymmetries in the sample's $J$-$V$ characteristics rectify $J_{\mathrm{lw}}$, resulting in a time-averaged tunnelling current $\langle J_{\mathrm{lw}} \rangle$ (magenta) which we measure electronically. $\langle J_{\mathrm{lw}} \rangle$ also reaches its maximum at $\Delta z = 0$, yet we measure the tapping-cycle-averaged rectified tunnelling currents.

Knowing from Fig. 4.4 that the new optical signal decays within 200 pm, we choose to reduce the tapping amplitude to only 200 pm – about one atomic diameter and orders of magnitude smaller than customary in SNOM. Reducing the tapping amplitude to this scale effectively eliminates both the background signal at the first harmonic – stemming from e.g. geometric modulation of the far field – and the mesoscopic near-field contribution. At the same time, the short-ranged signal is still modulated.

Under these extreme conditions, we analyse whether our phase-shifted optical signals can be correlated with the lightwave-driven tunnelling currents. Specifically, we investigate their dependence on the tip-sample separation. We simultaneously sample the decay of both signals (Fig. 4.6) and observe that even at picometric tapping amplitudes a strong scattered signal $E_2^{\mathrm{scat}}$ persists, where the peak electric field $\hat{E}_2^{\mathrm{scat}} = E_2^{\mathrm{scat}}(t = 0\,\mathrm{fs})$ decays by an order of magnitude over 200 pm (Fig. 4.6**a**). This decay behaviour strikingly resembles that of the time-averaged lightwave-driven tunnelling currents $\langle J_{\mathrm{lw}} \rangle$, further supporting a common origin of the two signals.

To validate this interpretation, we trace the scattered THz electric field waveforms in the time domain (Fig. 4.6**b**). At a minimal relative tip-sample separation of $\Delta z = 0$, we detect intense waveforms peaking at EOS time $t = 0\,\mathrm{fs}$ in both scattered harmonics (blue spheres). To compare this to the conventional mesoscopic near-field signals, we also record a scattered near-field waveform with a larger tapping amplitude of $A = 2\,\mathrm{nm}$ outside of the tunnelling regime (orange spheres). Again we find the distinct phase shift of $\pi/2$ between the conventional near fields and our short-ranged signal, providing further indication that this new signal originates from lightwave-driven tunnelling. The picometric decay together with the distinct $\Delta\varphi = \pi/2$ phase shift points to the microscopic mechanism of the atomically confined near-fields: An alternating optical polarisation formed by ultrafast a.c. tunnelling currents which are driven by the THz electric fields.

Yet, the light emission from such a tunnelling event, consisting of a handful of electrons tunnelling across an angstrom-scale gap, according to equation 4.1 would be virtually undetectable. However, by leveraging the efficient coupling of fields at the tip apex into the far field via the tip acting as an antenna, tunnelling-driven emission surpasses even the conventional near-field signal in our specific experimental conditions. This result critically relies on atom-scale stability and picometric tapping

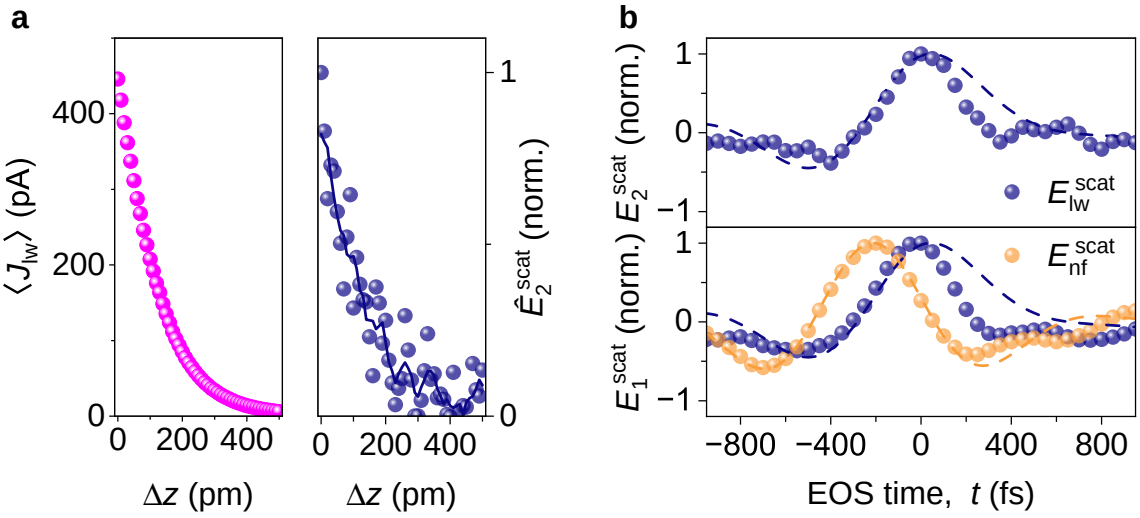


**Figure 4.6 |** Picometre near-field decays. **a**, When the tip-tapping amplitude is reduced to 200 pm, the peak of the scattered signal $\hat{E}_2^{\mathrm{scat}} = E_2^{\mathrm{scat}}(t = 0\,\mathrm{fs})$ demodulated at the second harmonic of $\nu_{\mathrm{tap}}$ decays on the same length scale as the time-averaged lightwave-driven tunnelling current $\langle J_{\mathrm{lw}} \rangle$ as a function of the relative tip-sample distance $\Delta z$. **b**, Scattered waveforms demodulated at $\nu_{\mathrm{tap}}$ (bottom) and $2\nu_{\mathrm{tap}}$ (top) for tip-tapping amplitudes $A = 200\,\mathrm{pm}$ (dark blue) and $A = 2\,\mathrm{nm}$ (orange). On average, about 180 electrons per pulse were rectified in the case of the dark blue curves, which were measured in tunnelling contact ($\Delta z \approx 0$). The dashed curves represent a fit based on the semiclassical model from section 4.3. $\hat{E}_{\mathrm{light}} = 0.8\,\mathrm{kV\,cm^{-1}}$. Figure adapted from [Sid24].

amplitudes. Only then the tunnelling-driven emission constitutes the dominant contribution to the observed response.

## 4.3 Terahertz emission from lightwave-driven tunnelling currents

In section 4.2, I demonstrated how we can use atomic-scale tapping amplitudes to isolate the novel short-ranged interaction from conventional near-field signals. We found that under these conditions, the optical signals decay on the same length scale as the time-averaged lightwave-driven tunnelling currents. To understand the subcycle dynamics occurring, specifically, to understand what gives rise to the $\pi/2$ phase shift, it is essential to uncover the microscopic mechanism leading to the light emission. In this section, I will present a semiclassical model (section 4.3.1), which is able to grasp the key signatures of our short-ranged signal, i.e. the $\pi/2$ phase delay with respect to conventional near fields and the atomic-scale localisation. Furthermore, I will also present in short, the fully quantum model developed by our theory partner *Jan Wilhelm* (section 4.3.2), which supports the conclusion that the phase-shifted optical signal originates from ultrafast tunnelling currents.

### 4.3.1 Semiclassical dipole model

Key features can be understood already with a semiclassical dipole model. There, the origins of the conventional, purely dielectric near-field signal and the tunnelling current signal can be described by time-dependent oscillating electric dipoles.
If a transient THz electric field $E_{\mathrm{light}}$ is coupled to the tip, a near-field dipole is induced, as described in section 2.1. Its dipole moment $\boldsymbol{p}_{\mathrm{nf}}$ follows the driving field and the dimensions of the dipole correspond to the radius of curvature of the tip. In addition, the electric field of this near-field dipole acts as a transient bias voltage (Fig. 4.7**b**) which can drive an atomically localised tunnelling current $J_{\mathrm{lw}}$ between the frontier atom of the tip and the sample. In the approximation of instantaneous tunnelling, which is fairly coarse [Jel17, Pel21], this transient bias drives an instantaneous tunnelling current $J_{\mathrm{lw}}$ (Fig. 4.7**c**), which follows the d.c. tunnelling conductance (Fig. 4.7**a**), in phase with the driving field. Both the near-field

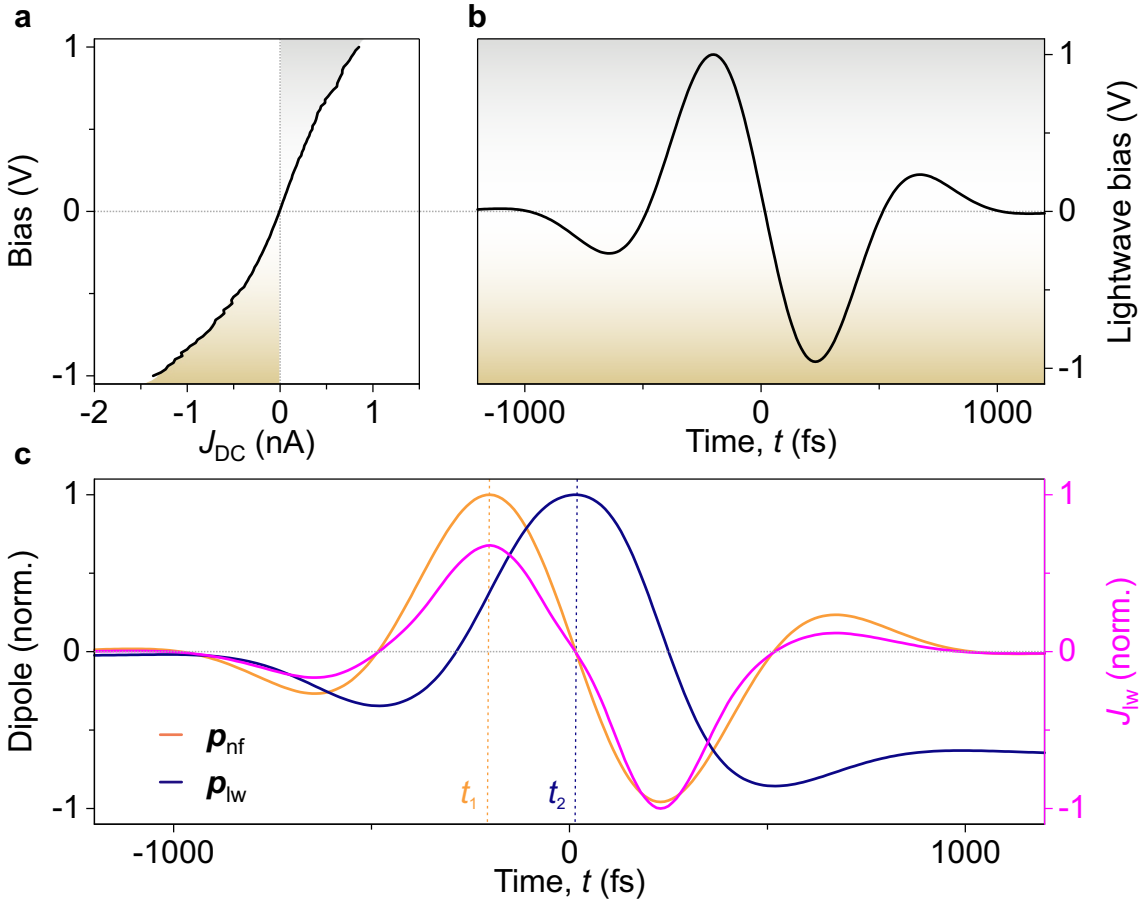


**Figure 4.7 |** Semiclassical modelling of the atomically confined optical near-field signals. **a**, Measured d.c. tunnelling conductance of the Au(111) sample. **b**, Lightwave bias induced by a test transient. **c**, Following the point-dipole model, the test transient forms an electric near-field dipole $\boldsymbol{p}_{\mathrm{nf}}$ (orange) in phase with the driving field. In the approximation of instantaneous tunnelling, this dipole drives an ultrafast tunnelling current $J_{\mathrm{lw}}$ (magenta) between tip and sample, according to the conductance shown in **a**. This current is in phase with the near-field dipole, reaching its maximum at time $t_1$, and it leads to the accumulation of charges, forming a second, lightwave-driven dipole $\boldsymbol{p}_{\mathrm{lw}}$ (blue). This dipole is proportional to the integral over the current, reaching its maximum at the zero crossing of the driving field ($t_2$, vertical dashed line), leading to a phase shift of $\pi/2$ compared to the mesoscopic near-field dipole.

dipole and the ultrafast tunnelling currents reach their maximum at the same time ($t_1$ in Fig. 4.7**c**).

This current in turn accumulates charge carriers in the tip and the sample, forming a second, lightwave-driven dipole $\boldsymbol{p}_{\mathrm{lw}}$ (Fig. 4.7**c**). Since the accumulated charge corresponds to the time integral over the instantaneous tunnelling current $J_{\mathrm{lw}}$, $\boldsymbol{p}_{\mathrm{lw}}$ reaches its maximum at the zero crossing of the driving electric field ($t_2$ in panel **c**). Accordingly, the phase of the lightwave-driven dipole moment $\boldsymbol{p}_{\mathrm{lw}}$ is retarded by $\pi/2$ compared to the driving field and the mesoscopic near-field dipole.

At large delay times where the driving field has already vanished, a residual $\boldsymbol{p}_{\mathrm{lw}}$ persists. This residual dipole forms the basis for the time-averaged lightwave-driven tunnelling current $\langle J_{\mathrm{lw}} \rangle$ measured in lightwave-STM. This highlights the depth of information available in our experiment, where the field-resolved optical signal provides insights into the full subcycle dynamics of $J_{\mathrm{lw}}$ directly in the time domain, rather than relying on solely measuring the time-averaged tunnelling current $\langle J_{\mathrm{lw}} \rangle$.

Both time-dependent dipoles, $\boldsymbol{p}_{\mathrm{nf}}$ and $\boldsymbol{p}_{\mathrm{lw}}$, emit light into the far field, which is detected via EOS. This emission is modified by the tip's antenna-like response. Accounting for the complex-valued tip-transfer function and the EOS detector response (for details see section 4.6), we can already use this semiclassical model to fit the previously measured data with a test waveform (dashed lines in Figs. 4.4 and 4.6).

Yet, the model ultimately assumes that the nanoscale dipole $\boldsymbol{p}_{\mathrm{lw}}$ is formed by accumulation of tunnelled electrons, and that the ultrafast flow of tunnelling electrons follows the same conductance as d.c. tunnelling, despite this being a rather simplified approximation [Jel17, Pel21], as already pointed out. Thus, our theory partner *Jan Wilhelm* performed a fully quantum-mechanical model based on *ab initio* time-dependent density-functional theory calculations.

### 4.3.2 Quantum model

*This section explains the key findings of the quantum model by Jan Wilhelm. For details on the calculations, I would like to refer to the methods section of our manuscript* [Sid24].

To grasp the formation dynamics of the lightwave-driven dipole $\boldsymbol{p}_{\mathrm{lw}}$ independent of any prior assumptions on the tunnelling itself, *Jan Wilhelm* carried out *ab initio* quantum simulations based on real-time time-dependent density functional theory (TDDFT), modelling the charge density in a tip-sample system consisting of 1010 sodium atoms for different tip-sample separations. There we trace the evolution of the charge density in the time domain, while an incoming transient electric field waveform $E_{\mathrm{light}}$ (central frequency: 6 THz, pulse duration[3]: 235.5 fs, peak electric field: $1\,\mathrm{V\,nm^{-1}}$) drives the dynamics. Here, the electron tunnelling dynamics is automatically included by the overlap of atomic orbitals.

In the semiclassical model, at time $t_1$ (top in Fig. 4.8**a**) where the driving field $E_{\mathrm{light}}$ reaches its maximum, the mesoscopic near-field dipole $\boldsymbol{p}_{\mathrm{nf}}$ which oscillates in phase with the driving field is maximal. With the quantum model (bottom in Fig. 4.8**a**), we find that at a tip-sample separation of 9 Å, the tunnelling current distribution ($J_{\mathrm{lw}}$, magenta isosurfaces) is highly inhomogeneous, determined by the polarisation of individual atomic orbitals. In contrast, when the tip is retracted to 14 Å, barely any tunnelling occurs. When the driving field crosses zero at $t_2$ in the semiclassical model (top in Fig. 4.8**b**), the near-field dipole vanishes but the charges accumulated from the tunnelling dynamics form an additional lightwave-driven dipole $\boldsymbol{p}_{\mathrm{lw}}$. The quantum simulation (bottom) shows how this dipole is formed: The tunnelling currents lead to a change in the charge density distribution at a tip-sample separation of 9 Å, as shown by the isosurfaces of the relative charge density $\Delta\rho$ in the bottom of panel **b**. Here, the relative charge density $\Delta\rho$ refers to the change in charge density with respect to equilibrium, where blue denotes a negative $\Delta\rho$, i.e. a decrease in charge density, and red a positive $\Delta\rho$. On the other hand, at $\Delta z = 14$ Å, where almost no tunnelling currents have flown, no dipole is formed.

Figure 4.9 shows the results of the quantum simulation in the time domain, calculated for a tip-sample separation of 9 Å. Plotted here are the near field at the tip apex

[3]Full width at half maximum of the Gaussian envelope.

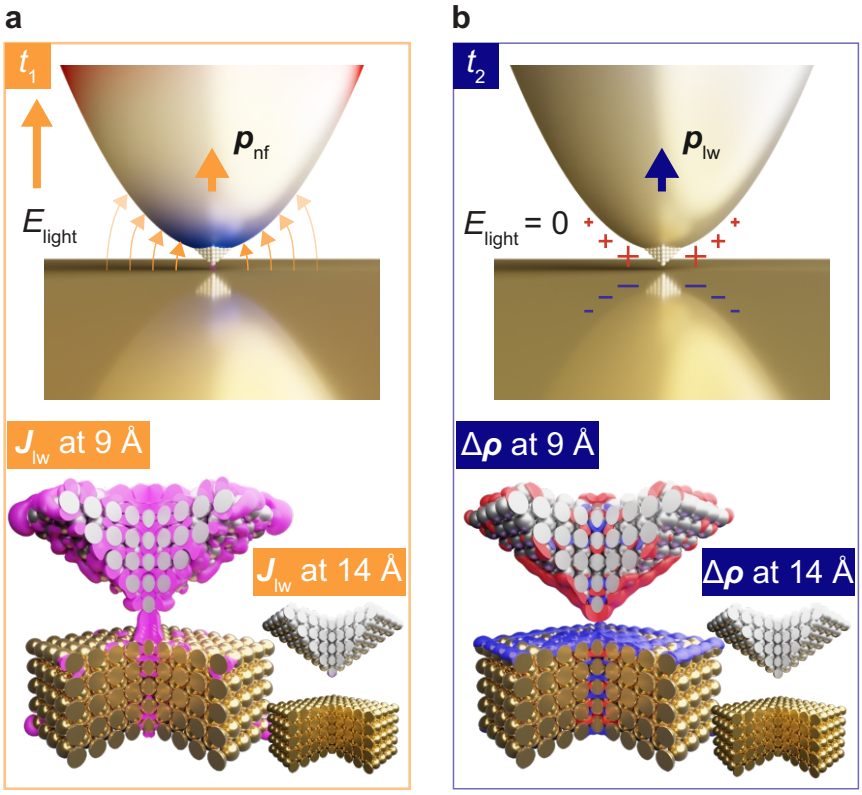


**Figure 4.8 |** Microscopic picture of the THz emission from ultrafast lightwave-driven tunnelling currents. **a**, At time $t_1$, $E_{\mathrm{light}}$ and the induced mesoscopic near-field dipole $\boldsymbol{p}_{\mathrm{nf}}$ are maximal (top). The bottom shows the frontier atoms of the tip. TDDFT is used here to calculate the ultrafast tunnelling currents at $t_1$, as depicted by the magenta isosurfaces. At a tip-sample distance of $z = 9\,\text{Å}$, lightwave tunnelling currents flow, whereas there is almost no ultrafast tunnelling at $z = 14\,\text{Å}$. **b**, At time $t_2$, where $E_{\mathrm{light}} = 0$, the near-field dipole $\boldsymbol{p}_{\mathrm{nf}}$ also reaches zero, but the charges accumulated from the tunnelling process form an additional lightwave-driven dipole $\boldsymbol{p}_{\mathrm{lw}}$. The results of the TDDFT calculations (bottom) show isosurfaces of the relative charge density $\Delta\rho$. For a tip-sample distance of 9 Å, a dipole exists even when the external lightwave-bias field crosses zero. This results from the ultrafast lightwave-driven tunnelling currents. In contrast, at $z = 14\,\text{Å}$ no sizeable dipole is formed owing to the lack of tunnelling. Blue: negative $\Delta\rho$, red: positive $\Delta\rho$. Figure adapted from [Sid24].

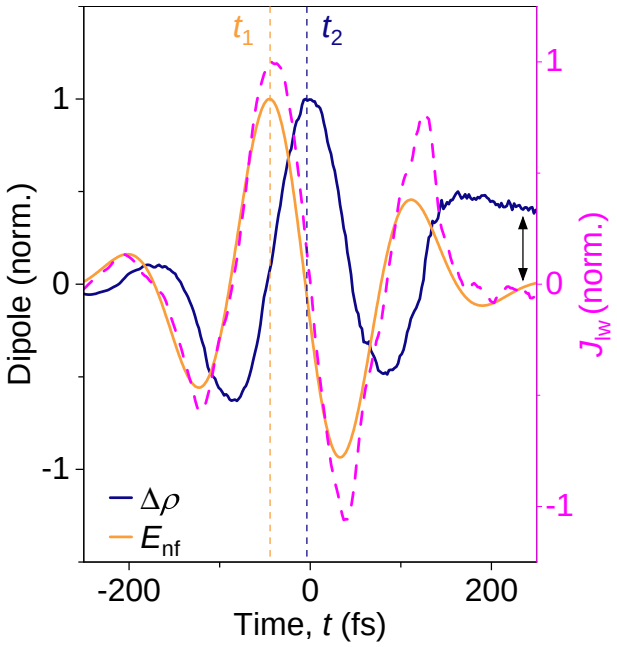


**Figure 4.9 |** Atomic-scale dipole formation dynamics in the time domain calculated in TDDFT at a tip-sample distance of 9 Å, showing the near field at the tip apex $E_{nf}$, the relative charge density $\Delta\rho$ and the instantaneous tunnelling currents $J_{lw}$. $t_1$ and $t_2$ indicate where the driving field reaches its maximum and the subsequent zero crossing, respectively. The experimentally observed $\pi/2$ phase shift is reproduced. A non-zero $\Delta\rho$ at large delay times (black arrow) shows that charges are accumulated owing to nonlinearities in the formation of the tunnelling currents. These residual charges are proportional to the time-averaged tunnelling currents $\langle J_{lw}\rangle$ measured in lightwave-STM. Figure adapted from [Sid24].

$E_{nf}$, the relative charge density $\Delta\rho$ and the instantaneous tunnelling currents $J_{lw}$. In this case, $\Delta\rho$ represents the total change in charge density, obtained as the sum over all relative charge $\Delta\rho$ in the tip minus the sum over all $\Delta\rho$ in the sample. The simulations successfully capture the characteristic phase delay of $\Delta\varphi = \pi/2$ between $E_{nf}$ and $\Delta\rho$. Notably, the presence of a non-zero $\Delta\rho$ at large delay times indicates that charges are accumulated owing to nonlinearities in the formation of the tunnelling currents. This confirms the prediction of the semiclassical model, that these residual charges form the time-averaged tunnelling currents $\langle J_{lw}\rangle$ observed in lightwave-STM.

The quantum simulations confirm the microscopic origin of our phase-shifted short-ranged optical signal: Light emission from subcycle tunnelling currents driven by the near fields. We thus call this new technique **N**ear-field **O**ptical **T**unnelling **E**mission, or in short **NOTE**.

Finally, we trace the peak of the NOTE dipole $\hat{p}_{lw}$ and the peak of the subcycle tunnelling currents $\hat{J}_{lw}$ as a function of tip-sample separation in the quantum simula-

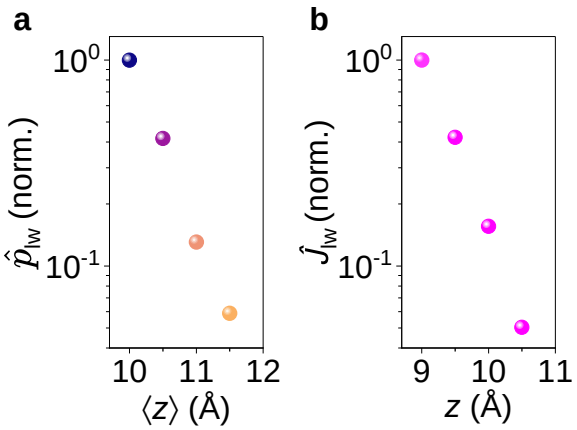


**Figure 4.10 |** Atomic-scale decay of the NOTE signal from the *ab initio* TDDFT calculations. **a**, Decreasing amplitude of the simulated NOTE dipole $\hat{p}_{\mathrm{lw}}$ as a function of average tip-sample separation $\langle z \rangle$ at a tapping amplitude of 1 Å. **b**, The maximum of the ultrafast tunnelling current $\hat{J}_{\mathrm{lw}}$ features a similar decay as a function of tip-sample separation $z$. Figure adapted from [Sid24].

tions (Fig. 4.10). Again, just as in Fig. 4.6, both signals decay on the same length scale.

First traces of more complex quantum dynamics might already be present in the experimental transients in Fig. 4.6. There, the experimental curves appear to oscillate at a higher frequency than predicted by the semiclassical model – independent of the test transients used for the semiclassical calculations. Such a deviation likely arises due to screening effects. Any tunnelled electrons polarise the surrounding medium, dynamically modifying the tunnelling barrier for the subsequent electrons.

Despite the significant advances made with the state-of-the-art quantum model, it still falls short in specific points. Accurately capturing NOTE with its inherently non-equilibrium and non-perturbative nature, would require scaling calculations to a degree that poses considerable challenges even for today's cutting-edge quantum theory. While these simulations reveal key NOTE features, fully accounting for many-body interactions – such as screening, scattering, and phonon and plasmon emission – remains a task for future theoretical development.

Nonetheless, these results illustrate that the NOTE dipole is formed by tunnelling. Thus the spatial resolution should be inherently governed by the overlap of atomic orbitals. This suggests the potential for atomic-scale resolution in NOTE microscopy, which we will explore in the following section. There I will demonstrate that NOTE is the first all-optical microscopy technique – one that relies solely on sending in light and measuring the outgoing light – featuring atomic resolution while also being subcycle sensitive.

## 4.4 Optical microscopy with atomic-scale spatial resolution

In the previous section, I detailed how we established a link between the optical NOTE signals and the subcycle lightwave-driven tunnelling currents. Both experiment (Fig. 4.6) and quantum simulations (Fig. 4.10) showed that the NOTE signal decays on atomic length scales. Given these two conditions, we expect the lateral resolution of NOTE microscopy to be similar to that of STM, which features sub-angstrom spatial resolution [Rep05, Lil07, Gro11, Coc16, Pel20, Che21, Roe24].

To test this hypothesis, we focus on a single packing defect in the herringbone reconstruction of a Au(111) surface (Fig. 4.11). This defect features a contrast in both d.c. STM and lightwave-driven STM (panels **a**,**c**) which likely stems from variations in the sample's local density of states. However, the defect holds the advantage that it is topographically flat, as seen in AFM (panel **b**). The flatness ensures that our optical signals are not influenced by topographic artefacts and allows us to use a quasi-constant height AFM feedback mode – we tap the tip and keep a constant frequency shift, maintaining a constant average tip-sample separation. We perform a high-precision line-cut through one of these defects, measuring simultaneously the rectified tunnelling current $\langle J_{\mathrm{lw}} \rangle$ (panel **d**) and the peak of the NOTE transient $\hat{E}_1^{\mathrm{scat}}$ (panel **e**). Both signals trace out the entire feature, determined by the extended wavefunction of the packing defect, illustrating that the resolution of both NOTE and lightwave-STM is governed by the orbital overlap of the frontier atom of the tip and the sample.

While the lateral extent of the packing defect's wave function limits the confinement of both the NOTE and STM signals on this sample, this does not imply a hard resolution limit. Instead, it indicates that the resolution in NOTE microscopy follows the same principles as state-of-the-art STM, where sub-angstrom features can be resolved. Unlike STM, NOTE does not rely on the electrical measurement of time-averaged tunnelling currents. Thus, NOTE microscopy should, like AFM [Gie03, Sch17], alternate charging scanning tunnelling microscopy (AC-STM) [Pat19] and near-field microscopy [Che19b], not be restricted to electrically conductive samples. As a result, NOTE should enable atomic and subcycle resolution even for non-conductive samples.

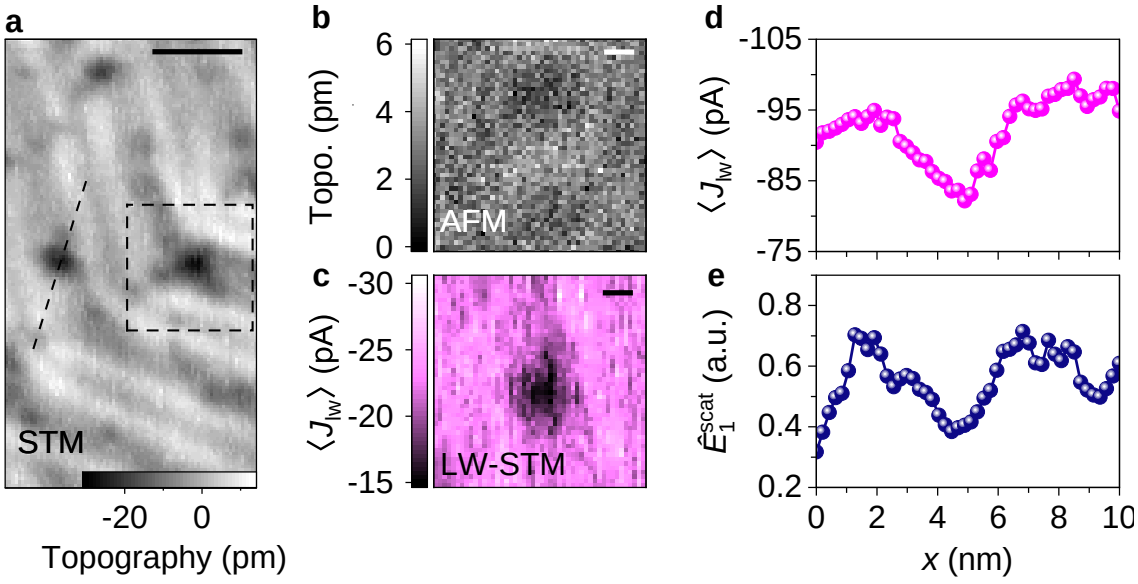


**Figure 4.11 |** Atomic-scale spatial resolution of NOTE microscopy. **a**, A herringbone reconstruction and nanometre-sized packing defects are revealed in a constant-current STM image of the Au(111) surface (voltage $V = -450\,\mathrm{mV}$, current setpoint $J_{\mathrm{set}} = 100\,\mathrm{pA}$). Scale bar: 5 nm. **b**, AFM topography ($A = 250\,\mathrm{pm}$, frequency shift setpoint $\Delta\nu_{\mathrm{tap}} = -6\,\mathrm{Hz}$) of the area marked by the dashed square in panel **a**. The defect is hardly noticeable in the AFM image, indicating that the STM signal stems from variations in the local density of states. **c**, The lattice defect is clearly visible in the quasi-constant-height lightwave-STM image captured simultaneously with panel **b**. Scale bars in **b** and **c**: 1 nm. **d**, Quasi-constant-height ($A = 250\,\mathrm{pm}$, $\Delta\nu_{\mathrm{tap}} = -5.8\,\mathrm{Hz}$) lightwave-STM line scan over a similar defect (dashed line in **a**), tracing the time-averaged lightwave-tunnelling current $\langle J_{\mathbf{lw}} \rangle$. Simultaneously, the same defect is imaged via its NOTE signal (**e**). Here, we show the peak of the scattered electric field transient demodulated at the first harmonic of the tapping frequency $\hat{E}_1^{\mathrm{scat}}$. To enhance clarity, the data have been smoothed using a Savitzky–Golay filter with a five-point window. $\hat{E}_{\mathrm{light}} = 0.4\,\mathrm{kV\,cm^{-1}}$ in **c** and $\hat{E}_{\mathrm{light}} = 0.5\,\mathrm{kV\,cm^{-1}}$ in **d**, **e**. With a pulse repetition rate of 13.7 MHz, one electron rectified per pulse corresponds to a time-averaged tunnelling current of about 2.2 pA. Figure adapted from [Sid24].

## 4.5 Subcycle atomic-scale spectroscopy

NOTE not only facilitates angstrom-scale spatial resolution, but it also allows for subcycle atomic-scale spectroscopy. We demonstrate this by studying a monolayer of tungsten diselenide ($WSe_2$) exfoliated directly on a flat Au(111) surface. This surface was prepared by cleaving mica and subsequent thermal evaporation of gold onto it in a high-vacuum chamber. Freshly cleaved $WSe_2$ was then stamped onto the gold surface in the load-lock chamber of the microscope, producing mostly monolayer but also bi- and trilayer $WSe_2$ flakes, which we can identify with steady-state tunnelling spectroscopy (Fig. 4.12**b**). Figure 4.12**a** shows a d.c. STM image of the monolayer $WSe_2$ on gold sample, revealing both the unit cell of the $WSe_2$ monolayer (yellow) and the moiré unit cell formed between it and the gold surface (orange).

When sweeping the THz electric field strength $\hat{E}_{\text{light}}$ and recording the time-averaged lightwave-driven tunnelling current $\langle J_{\text{lw}} \rangle$ we trace out the onset of tunnelling into the valence band of the $WSe_2$ monolayer (Fig. 4.12**c**). We also sample the peak of the NOTE signal in both the first and second harmonic ($\hat{E}_1$ and $\hat{E}_2$) as a function of $\hat{E}_{\text{light}}$ (Fig. 4.12**d**). At the highest field strength, about 20 electrons are rectified per pulse. The emerging optical nonlinearity resembles the onset behaviour of valence band tunnelling, as highlighted by the dashed lines which are overlaid as a guide to the eye and correspond to the d.c. conductance onset of the valence band. This remarkable agreement is a signature of the subcycle sampling inherent to NOTE, where the instantaneous tunnelling current at the peak of the incident field maps directly onto the peak of the NOTE signal, owing to the $\pi/2$ phase shift between the two.

While NOTE offers model-free access to subcycle tunnelling spectroscopy, this is not the case for the time-averaged lightwave-driven current $\langle J_{\text{lw}} \rangle$ (Fig. 4.12**c**). Although $\langle J_{\text{lw}} \rangle$ also traces out the onset, this current originates only from electrons rectified by our specific combination of waveform and conductance. All subcycle dynamics which might occur are lost in the process of rectification.

The measurements in this section can be considered as the first atomic-scale subcycle measurement of ultrafast conductance. Taking this idea yet one step further, the following section will provide a first glimpse into how NOTE can deliver information on the subcycle atomic-scale tunnelling dynamics directly in the time domain.

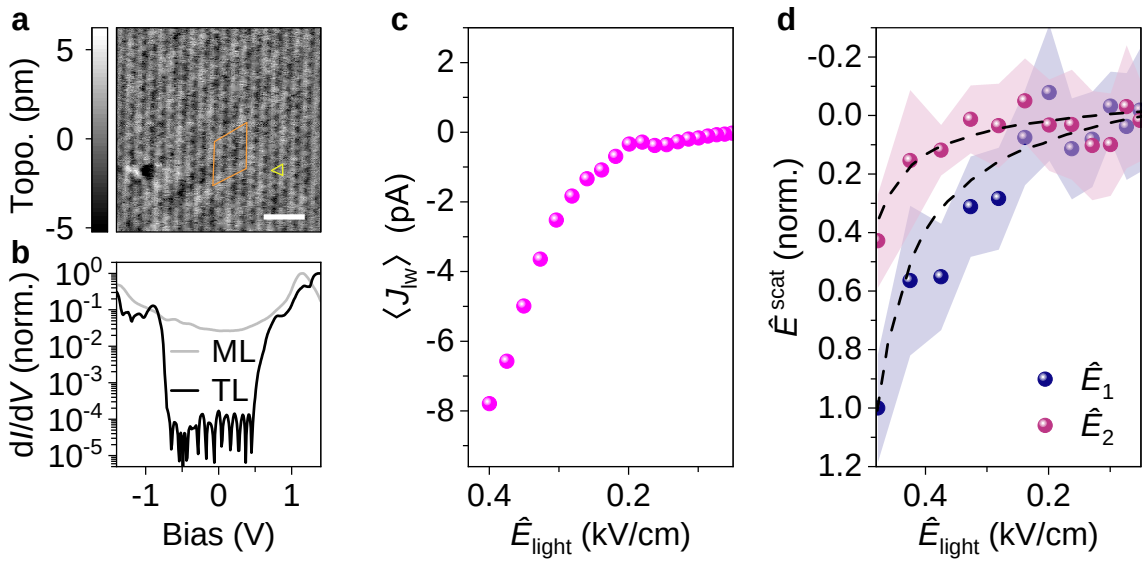


**Figure 4.12 |** Subcycle atomic-scale spectroscopy of $WSe_2$. **a**, Constant-current STM image (bias voltage $V = 1\,\mathrm{V}$, current setpoint $J_{set} = 100\,\mathrm{pA}$) of the surface of the monolayer $WSe_2$ which is exfoliated directly on flat Au(111). The unit cells of the $WSe_2$ and the moiré superlattice formed between it and the gold surface are depicted in yellow and orange, respectively. Scale bar: 1 nm. **b**, steady-state differential conductance spectroscopy of monolayer (ML) and trilayer (TL) $WSe_2$ on Au(111). The trilayer features a clear band gap. **c**, The onset of time-integrated THz-driven tunnelling currents $\langle J_{lw} \rangle$ in monolayer $WSe_2$ as a function of the peak THz field strength ($\hat{E}_{light}$), indicating the start of tunnelling into the $WSe_2$ valence band. **d**, The peak of the scattered NOTE transients demodulated at the first harmonic $\hat{E}_1$ and second harmonic $\hat{E}_2$ of the tapping frequency features an onset behaviour as a function of $\hat{E}_{light}$. On average, about 20 electrons are rectified per pulse at the highest used field strength. For reference, the d.c. valence band conductance onset of the monolayer is overlaid as black dashed lines as a guide to the eye. The error bars correspond to one standard deviation. Figure adapted from [Sid24].

## 4.6 Clocking subcycle tunnelling currents on atomic length scales

The simplicity of the tunnelling junction of a $WSe_2$ monolayer exfoliated directly onto a flat Au(111) surface leads to an ultrafast current-voltage characteristic that closely resembles its d.c. counterpart. Yet, in most material systems, the ultrafast flow of tunnelling electrons is unlikely to line up with the d.c. behaviour. In this section, I will explain, how the NOTE signal enables access to the ultrafast tunnelling dynamics directly in the time domain and how we can leverage this to trace the subcycle tunnelling currents within the band gap of a semiconducting quantum material – a trilayer of $WSe_2$ on gold.
In our models, the NOTE dipole is formed as a time integral over the ultrafast tunnelling currents. Thus, by differentiating this dipole, we can access the subcycle tunnelling currents directly in the time domain. To do so, we need to first retrieve the NOTE dipole at the tip's apex, which emits the NOTE transients we measure in electro-optic sampling.

### 4.6.1 Retrieving atomic-scale dipoles at the scanning probe's apex

In our measurement we detect far-field waveforms which are scattered from the nanoscopic scale of the tip's apex. Yet, the NOTE transients measured in the far field differ from the NOTE dipole at the tip apex. This transformation is mainly governed by two contributions: the response function of our detection system and the scattering process from the near field to the far field. In this section, I will explain, how we can account for both of these transformations to gain access to the time-dependent dipoles at the tip's apex.

#### Correcting for the detector response

Our detection system features a complex-valued frequency-dependent response function. Thus, the transients we measure in EOS do not directly represent the electric field propagating to the electro-optic crystal. There are two main factors which we

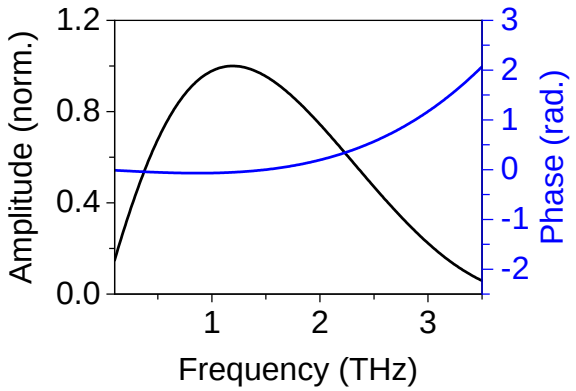


**Figure 4.13 |** Response function of the electro-optic sampling setup including the detector response of the ⟨110⟩-cut GaP electro-optic crystal with a thickness of 2 mm and the focusing conditions. The response function's amplitude features a FWHM bandwidth of 2.1 THz ranging from 0.3 THz to 2.4 THz, while the phase is relatively flat at frequencies up to 1.5 THz where it begins to increase. Figure adapted from [Sid24].

have to take into account to correct for this. On the one hand, the focal spot size is frequency dependent owing to diffraction. Higher frequencies are focused more tightly, which increases their field strength in comparison with lower frequencies. Since the gate pulses have a significantly higher centre frequency (291 THz) than the sampled waveforms (~0.1-2.5 THz), only the centre of the THz beam will interact with the gate pulses, effectively acting as a high-pass frequency filter in our detection. To evaluate the influence of this effect, we use Gaussian optics to find the frequency dependent detection sensitivity. For this we evaluate the local frequency-dependent field strength and integrate over the volume in which the interaction with the gate pulses takes place [Pla21].

On the other hand, the electro-optic crystal introduces additional frequency dependence. This stems from the coupling between the THz and gate pulses via the $\chi^{(2)}$ nonlinearity, the transmission through the electro-optic crystal, and the phase matching condition [Kam07]. Taking all these effects into account, we receive the complex-valued EOS response function of our detection system as shown in Fig. 4.13. The response amplitude features a FWHM bandwidth of 2.1 THz spanning from 0.3 THz to 2.4 THz. The spectral phase is relatively flat up to 1.5 THz from whereon it increases.

### Numerical simulation of the tip-transfer function

The second critical contribution affecting the measured waveform is the emission process from the tip's apex into the far field. The nanoscale tip acts as an antenna,

and the frequency-dependent transfer from the tip to the far field can be described by a complex-valued transfer function. Numerical simulations allow for the calculation of these transfer functions. We build here on previous experience in their calculation [Pel21].

To simulate the frequency dependent transfer function from the far field to the near field, we solved Maxwell's equations in the frequency domain with the commercial finite element solver COMSOL Multiphysics. The tip geometry (Fig. 4.14**a**,**c**) was modelled with a shaft radius of 62.5 µm, a tapered section length of 150 µm, and an apex radius of curvature of 50 nm, as determined from electron microscopy images of the experimental tip (Fig. 4.14**b**). We positioned the tungsten tip at $d_{\mathrm{tip}} = 1\,\mathrm{nm}$ above a flat gold sample and implemented the complex dielectric functions of tungsten [Ord88] and gold [Ord87] from literature. Tip and sample were placed into a 2D simulation geometry with a width of 0.9 mm and a height of 1.2 mm, allowing us to calculate the transfer function for a spectral range from 0.3 THz to 6 THz with a spacing of 0.1 THz within our available computational resources.

We coupled in the THz radiation at an angle of $\alpha = 33°$ (with respect to the sample surface) by using a scattering boundary condition on the incoupling side. To minimise artefacts stemming from scattering and diffraction at the edges where the excitation boundary meets other regions, we multiplied the incoupled plane wave with a windowing function $W(s)$:

$$W(s) = \frac{1}{2}(1 - \cos(2\pi\frac{s}{L})),$$

where $s$ is the coordinate along the scattering boundary and $L$ the length of the scattering boundary.

Except for the excitation boundary, all boundaries were equipped with perfectly matched layers to absorb all outgoing radiation and imitate an infinite volume. The edges of the perfectly matched layers were also given a scattering boundary condition to further suppress any residual backscattering.

To simultaneously account for the influence of the mesoscopic tip shape and the nanoscopic tip apex, we implemented a graded mesh [Pel21] (Fig. 4.15). This approach allows the large simulation volume to be meshed coarsely while maintaining a fine mesh at the nanoscale tip apex. We achieve this by decreasing the mesh

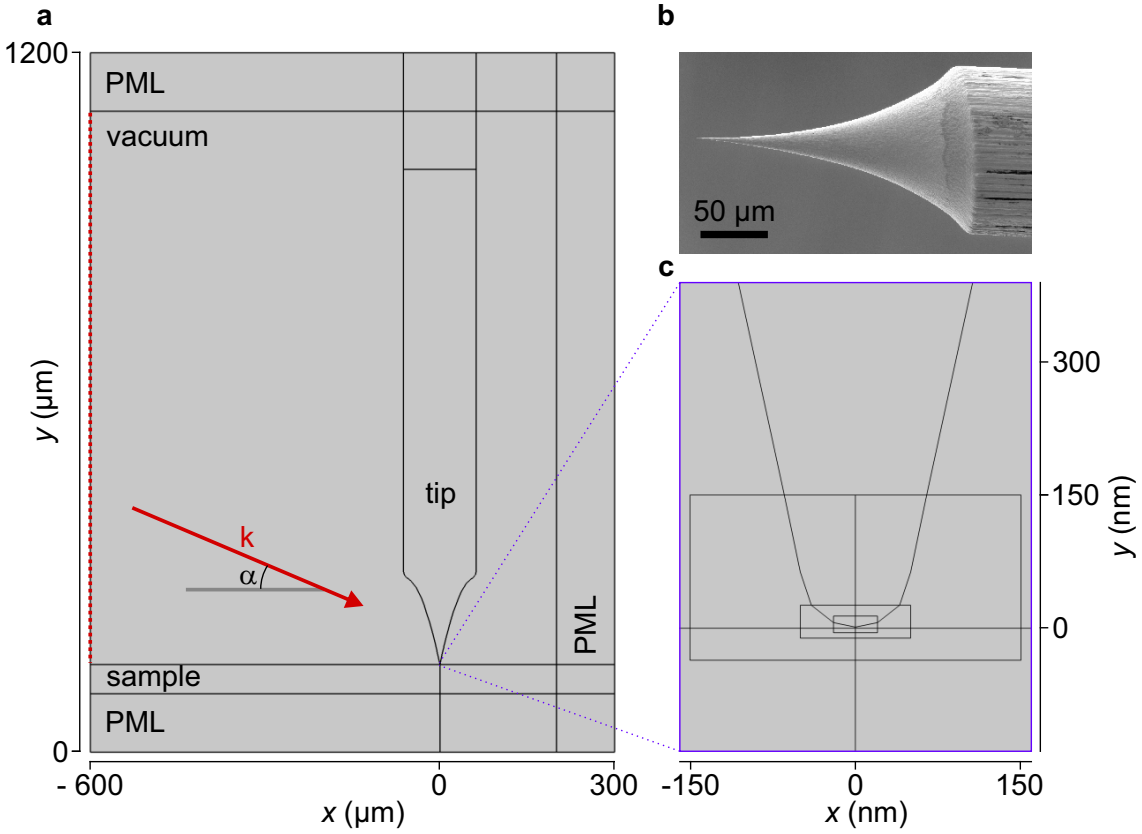


**Figure 4.14** | Finite element simulation geometry. **a**, The 2D simulation area is surrounded by perfectly matched layers (PML) with a thickness of 100 µm, except for the excitation boundary (dashed red line), where the light is coupled in at an angle of $\alpha = 33°$ by a scattering boundary condition. The tip is based on a scanning electron microscopy image (**b**) of the type of tip used in the experiments. Shaft radius: 62.5 µm, length of the tapered part of the tip: 150 µm, tip apex radius of curvature: 50 nm, tip sample distance: 1 nm. **c**, The zoom-in shows the simulation geometry at the apex of the tip, which is split into multiple sections to allow for graded meshing. k: Wave vector.

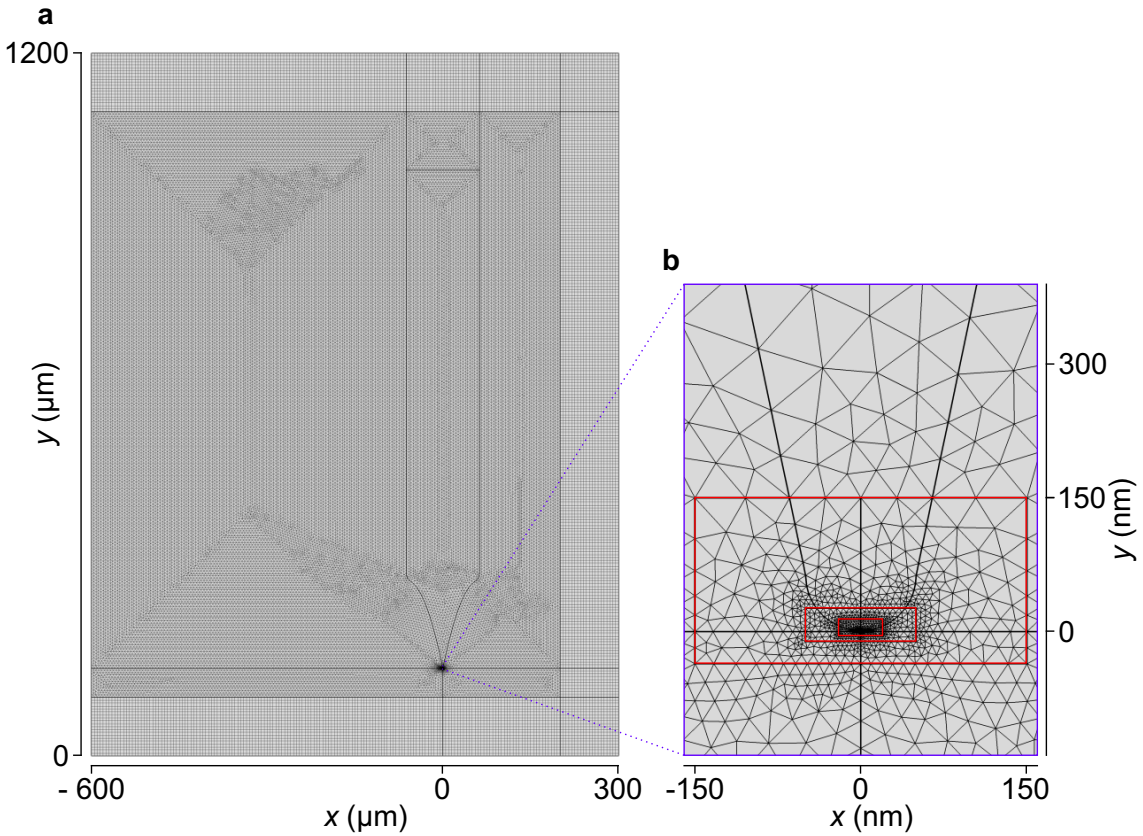


**Figure 4.15 |** Meshing of the simulation volume. To enable simultaneous meshing of a large volume, comparable with the excitation wavelength, and a nanoscale STM tip, a graded mesh is used. In the main volume (**a**) a maximum element size of 5 µm is employed to ensure at least 10 meshing points per wavelength. The inset (**b**) shows the boxes (red lines) which are used to grade the mesh. Towards the tip, the mesh becomes progressively finer such that there are always multiple mesh nodes between tip and sample.

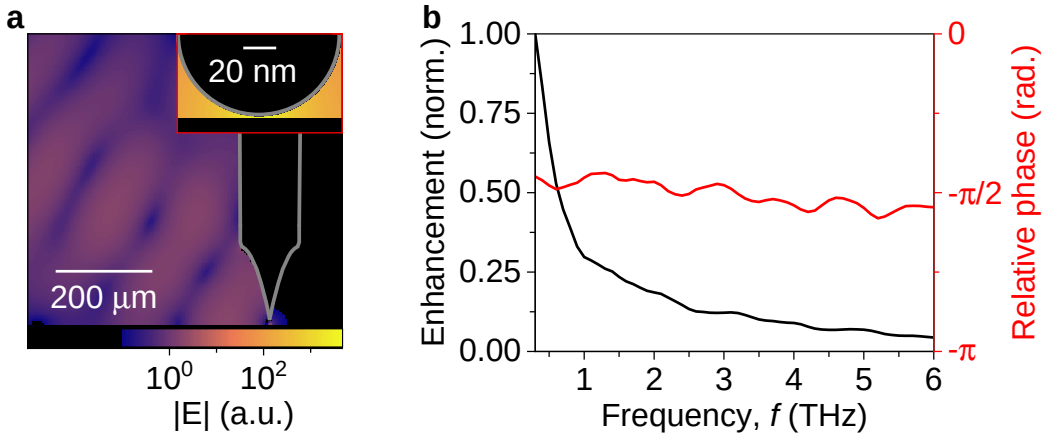


**Figure 4.16 |** Numerical simulation of the tip-transfer function. **a**, Simulated electric field amplitude $|E|$ for an excitation frequency $f$ of 1 THz, with the outline of the STM tip sketched in grey. The field at the apex of the tip is shown in the inset. **b**, Calculated field-enhancement factor, resembling a $f^{-1}$ behaviour, and relative phase shift as a function of frequency. The phase is shifted by approximately $-\pi/2$ and both phase and field enhancement feature slight periodic modulations. Figure adapted from [Sid24].

size stepwise (red boxes in Fig. 4.15**b**). To ensure at least 10 mesh elements per wavelength at a maximum frequency of 6 THz, the maximal mesh-element size was kept at 5 µm. The minimum element size at the tip apex was 3 Å, ensuring multiple meshing nodes between tip and sample.

To retrieve the complex-valued transfer function (Fig. 4.16), we evaluate the electric field's amplitude and phase in the centre of the tunnelling junction ($E_{\mathrm{tip}}$, $\varphi_{\mathrm{tip}}$) and compare them to results from a reference simulation where the tip was replaced with vacuum ($E_{\mathrm{vac}}$, $\varphi_{\mathrm{vac}}$). We evaluate the field enhancement by calculating the ratio $E_{\mathrm{tip}}/E_{\mathrm{vac}}$ and the phase shift is calculated as the difference $\varphi_{\mathrm{tip}} - \varphi_{\mathrm{vac}}$. When sweeping the frequency of the incoupled lightwave, we find the field enhancement showing a clear $f^{-1}$ behaviour ($f$: THz frequency), consistent with the results in reference [Pel21], with slight modulations which can be altered by changing the tip geometry. These slight modulations are also seen in the phase shift of approximately $-0.5\pi$. In reference [Pel21] a similar periodic modulation was found and attributed to standing waves formed by surface plasmons reflected at the tip's etching edge and at the tip apex, giving rise to a periodic enhancement or reduction of the

coupling efficiency. It is important to note here, that both near-field and NOTE signals originate from extremely sub-wavelength volumes at the tip apex. Thus they both experience the same phase shift and their relative phase is not influenced by propagation.
To conclude, by quantifying the complex-valued frequency-domain response functions of both the detection system and the scattering process, we can now reconstruct the time-dependent dipoles at the tip's apex. Building on these results, section 4.6.2 will demonstrate how NOTE can provide a first glimpse into subcycle atomic-scale tunnelling currents directly in the time domain.

### 4.6.2 Tracing subcycle atomic-scale tunnelling directly in the time domain

NOTE microscopy directly measures the optical signal emitted by tunnelling currents that are driven on a subcycle timescale. Therefore, it does not rely on a net current flowing, unlike lightwave-STM. This allows us to investigate even insulating samples, as I will demonstrate in this section. With the tools developed in section 4.6.1, we will even be able to extract these subcycle tunnelling currents directly in the time domain.
To gain access to the instantaneous tunnelling currents, we first need to find the nanoscale dipoles at the tip's apex – the extraction is illustrated in Fig. 4.17, where we begin by measuring the electric field transient in the time domain via EOS. We then proceed to the frequency domain via a Fourier transform. There, we correct the spectrum by dividing it by the tip-transfer function (Fig. 4.16), which we obtained by solving Maxwell's equations with the numerical finite element simulations, and we divide by the response function of our detection system (Fig. 4.13). Since the response function features spectral components with zero amplitude at large frequencies, a windowing function is required to erase any artefacts arising from dividing by zero. The corrected spectrum is then transformed back into the time domain using an inverse Fourier transform, yielding the oscillating dipole at the tip's apex, which emits the light we measure. This process holds true for both the near-field and the NOTE dipole. The latter arises from the accumulation of the tunnelled charge carriers. As established in section 4.3, this is mathematically expressed by the

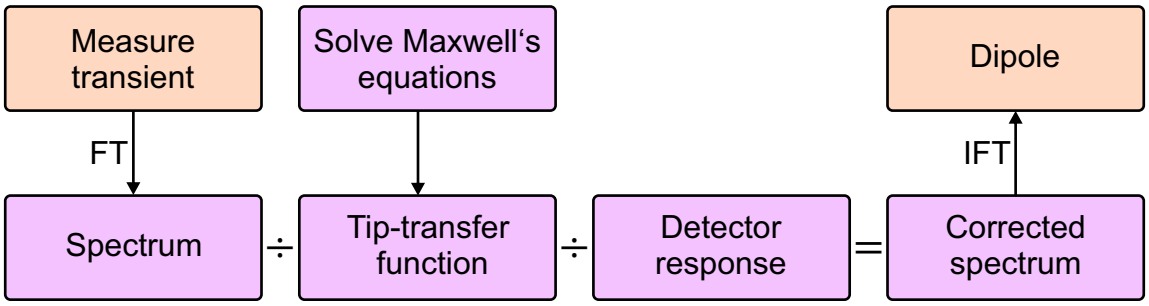


**Figure 4.17 |** Schematic on the retrieval of the nanoscale dipole at the tip's apex. The transient electric field waveform is measured in the time domain and converted to the frequency domain via a Fourier transform (FT). There, the complex-valued spectrum is divided by the tip-transfer function, derived from solving Maxwell's equations, and by the response function of the detection system. This yields the corrected spectrum, which is then transformed back into the time domain using an inverse Fourier transform (IFT) to obtain the dipole at the tip's apex. Peach: Time domain. Purple: Frequency domain.

NOTE dipole being the integral of the ultrafast tunnelling currents. Thus, taking its time-derivative reveals the subcycle tunnelling current directly in the time domain.

To demonstrate that the ultrafast flow of tunnelling electrons can dramatically differ from the d.c. case, we switch to a more insulating sample: a native trilayer of $WSe_2$ on Au(111), which can also be found on the sample system that was described in section 4.5. The additional layers of $WSe_2$ form intermediate tunnelling barriers, removing direct tunnelling between the tip and the gold surface, and give rise to alternative tunnelling pathways. The d.c. STM differential conductance of this sample is shown in Fig. 4.12**b**, revealing a clear band gap, confirming its semiconducting nature. We now tune the amplitude of the transient THz bias voltage, such that tunnelling out of the valence band of the trilayer only just sets in. Thus, if d.c. and ultrafast a.c. tunnelling followed the same current-voltage behaviour, as approximated in lightwave-STM, only the field crest of the THz waveform would drive tunnelling. Consequently, this current would be uni-directional.

To challenge this approximation, we set out to resolve ultrafast atomic-scale tunnelling currents with subcycle time resolution for the first time using the method described above. We first measure the near-field transient on the $WSe_2$ trilayer with a slightly retracted tip ($E_1$ in Fig. 4.18**a**) and compare it to the NOTE signal that we obtain

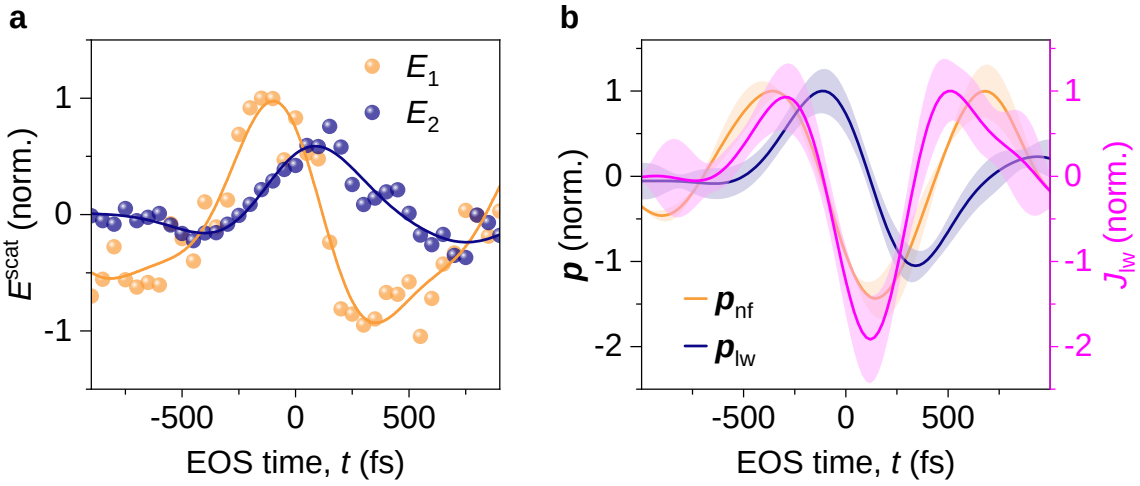


**Figure 4.18 |** Subcycle tunnelling currents on trilayer $WSe_2$. **a**, Scattered near-field transient demodulated at $\nu_{tap}$ measured with a slightly retracted tip, $E_1$, and NOTE transient, $E_2$, demodulated at $2\nu_{tap}$ recorded in tunnelling contact. $E_2$ was measured with a rectified tunnelling current of approximately 50 electrons per pulse on average at a frequency shift setpoint of $\Delta\nu = -6\,\mathrm{Hz}$ at a tapping amplitude of $A = 250\,\mathrm{pm}$. $E_1$ was measured with a tip retracted by 300 pm from the original setpoint. **b**, By accounting for the tip-transfer function and the response of the detection system, we can retrieve the time-dependent dipoles at the apex of the tip, $\boldsymbol{p}_{nf}$ and $\boldsymbol{p}_{lw}$, that emitted $E_1$ and $E_2$ in **a**, respectively. The instantaneous tunnelling current $J_{lw}$, obtained by differentiating $\boldsymbol{p}_{lw}$ is shown in magenta. The error bars in this figure correspond to one standard deviation. $\hat{E}_{light} = 0.3\,\mathrm{kV\,cm^{-1}}$. Figure adapted from [Sid24].

in tunnelling contact ($E_2$ in Fig. 4.18**a**). There, on average about 50 electrons per pulse are rectified.

By accounting for the tip-transfer function and the response function of the detection system, we retrieve the near-field dipole $\boldsymbol{p}_{nf}$ from $E_1$ and the NOTE dipole $\boldsymbol{p}_{lw}$ from $E_2$ (Fig. 4.18**b**). Finally, taking the time derivative of the NOTE dipole, we directly clock the subcycle tunnelling currents in the time domain (magenta in Fig. 4.18**b**). I would like to emphasise here, that to the best of our knowledge, these experiments mark the first subcycle tunnelling process ever resolved directly on atomic length scales.

Intriguingly, we observe a finite tunnelling current, even for bias voltages within the band gap of the sample, where no rectified lightwave-driven tunnelling currents can

be measured. These currents could for example stem from the additional tunnelling pathways introduced by the $WSe_2$ trilayer, where some are completely hidden to time integrated measurements. Several alternative tunnelling pathways could occur in the trilayer. For example, a charge planted into the top layer can sequentially tunnel to the second and then third layer, which is hybridized with gold, allowing it to reach the substrate. Alternatively, the charge could remain in the top or second layer for some time before returning to the tip within the next half cycle of the driving field. The net, time-averaged current picked up by the STM preamplifier can only be sensitive to the first path. However, the charges temporarily occupying the top and middle layers inevitably contribute to the NOTE signal. Additionally, the signal may be affected by field-induced band bending and subcycle distortion of atomic orbitals in the top $WSe_2$ layer – caused by charges that are trapped within the trilayer during the entire THz pulse.

It is these effects which are beyond reach of conventional current-sampling techniques and which are only accessible through the subcycle sampling intrinsic to NOTE. This highlights the greatest strength of all-optical NOTE microscopy: enabling subcycle access to tunnelling currents directly in the time domain without prior assumptions about the non-equilibrium material conductance or the exact fields at the tip apex. Unlike in current-sampling techniques, NOTE's quantitative field sampling of the emitted light relies on the well-defined and instantaneous $\chi^{(2)}$ optical nonlinearity of EOS. This downconversion in the EOS crystal is both spatially and temporally separated from the dynamics occurring within the tip-sample junction. Thus, the detection scheme is completely decoupled from the inherent sample dynamics. This is in stark contrast to lightwave-STM where only the electrons that happen to be rectified as a consequence of the complex interplay of competing nonlinearities can be detected. Instead NOTE gives direct subcycle access to the flow of quantum mechanical entities – electrons – providing unique insights into tunnelling dynamics far from equilibrium, in the strong-field regime. Under these circumstances, previously tunnelled electrons can influence the tunnelling dynamics of the following electrons [Pel21, Roe24]. Thus, as in attosecond ionisation [Dah12] and high-harmonic generation [Cor07, Kra09], the absolute timing of electron tunnelling becomes critical. The extreme confinement of tunnelling electrons in space and time in NOTE greatly increases the probability of two consecutive tunnelling electrons interacting, enhancing correlation effects. NOTE

enables in situ control over this confinement. This approach could be particularly interesting for correlated materials, e.g. including the formation of excitons near specific atomic sites.

To conclude this chapter, we have found a novel quantum-mechanical atomic-scale contrast mechanism for near-field microscopy: light emission from ultrafast a.c. tunnelling currents driven by optical near fields. This discovery brings ultrafast optical microscopy to atomic length scales and facilitates clocking the subcycle dynamics of atomically confined tunnelling currents directly in the time domain. Since NOTE measures the light emitted by electrons transiently driven to and from the sample (similar to AC-STM [Pat19] but on an ultrafast time scale), it does not rely on time-averaged tunnelling currents, even providing access to insulating materials. Furthermore, the detection in NOTE is based on the instantaneous $\chi^{(2)}$ nonlinearity of EOS and is thus decoupled from the sample dynamics, unlike in current-sampling techniques.
Looking ahead, we envisage NOTE unravelling quantum phases one by one by tracing the subcycle quantum flow of electrons on its intrinsic length and time scales. To facilitate this, we aim to prepare a host of dynamical phases of matter by fabricating novel material systems and driving elementary excitations within these. To prepare these excited states, we have developed a state-of-the-art tunable optical pump source operating at MHz repetition rates. This pump source can be modulated at high frequencies up to 300 kHz while maintaining thermal stability, promising atomic resolution optical pump—NOTE probe experiments. The next chapter will detail the design and setup of this tunable optical pump source.

Chapter 5

# A tunable ultrafast optical pump source

*The noncollinear optical parametric amplifier (NOPA) described in this chapter was developed together with Christian Meineke and Lukas Kastner, who at the same time built similar NOPAs in their setups. Especially former Bachelor's and Master's student Peter Menden helped in the construction of this NOPA. My colleagues Felix Schiegl and Svenja Nerreter contributed in the final stages of the development.*

Near-field optical tunnelling emission microscopy opens an entirely new perspective on elementary dynamics at their intrinsic length and time scales, promising to unravel the inner workings of even the most complex material systems. Among these, twisted van der Waals heterostructures have recently attracted particular interest owing to their remarkable potential for realising elusive states of matter in the laboratory [Gei13, Cao18, Wan18, Zho21, Ken21, Zha21a].

By stacking different materials, monolayer by monolayer, such heterostructures offer an extremely versatile toolbox with a host of tuning knobs, including twist angle, gating and strain [Ken21]. This allows precise control over emergent phenomena – reliably creating and manipulating new phases of matter, such as charge density waves [Che20], superconductors [Cao18, Bal20], Mott insulators [Che19a], moiré flat bands [Bal20, Xia21, Xu22] and moiré excitons [Yu17, Tra19, Hua22].

In semiconducting TMDC monolayers, the Coulomb interaction between electrons and holes is significantly stronger than in bulk semiconductors due to reduced dielectric screening. Additionally, the lower dimensionality leads to a smaller effective

separation between electron and hole. Together with large effective masses, this gives rise to high exciton binding energies, of a few hundred meV, allowing excitons to remain stable even at room temperature [Wan18].

Excitons in moiré superlattices experience a periodically modulated potential landscape and have been shown to localise [Kar22] and form on ultrafast time scales [Sch22] in momentum space studies. However, directly resolving moiré exciton formation in space and time has so far remained elusive.

For this task, NOTE microscopy would be ideally suited, particularly when combined with an ultrafast tunable pump source capable of resonantly generating excitons in various material systems. Typical exciton resonances in TMDCs range from the near-infrared to the visible spectral range – around 1-2 eV [Wan18]. To reach such photon energies, optical parametric amplification of a broadband supercontinuum can be exploited.

Optical parametric amplifiers (OPAs) driven by ultrashort NIR pulses have proven to be stable, tunable light sources. Their broad gain bandwidth, made possible by nonlinear crystals that support broadband phase matching – such as $\beta$-barium borate (BBO) – allows for tunability from the visible to the NIR spectral range, and enables pulse durations shorter than the seed pulses provided by the driving lasers [Rie00, Cer03, Man16].

However, commercially available ytterbium-laser-based OPAs generating femtosecond visible light pulses typically operate at pulse repetition rates of a few hundred kilohertz. Currently, the highest commercially available pulse repetition rate is 2 MHz (offered by *Light Conversion*, *Active Fiber Systems*, and *APE*). Even in scientific literature, reports on optical parametric amplifiers operating in the visible spectral range and at MHz repetition rates remain scarce [Fat12, Nil14, Mei24].

Thus we developed a two-stage noncollinear optical parametric amplifier (NOPA) operating at pulse repetition rates of up to 8.26 MHz, with a tunable centre wavelength in the spectral range from 650 nm to 900 nm. The design and implementation of the NOPA will be discussed in this chapter. Section 5.1 introduces the relevant physical principles and design considerations. The experimental implementation is described in section 5.2, followed by section 5.3 which presents a novel pump modulation scheme we developed to avoid measurement artefacts arising from thermal tip-expansion effects.

## 5.1 Optical parametric amplification

With ytterbium-based lasers, spectral tunability down to wavelengths as short as 650 nm can be achieved in an OPA seeded by a supercontinuum generated in a $\chi^{(3)}$ medium and pumped by the second harmonic of the laser's fundamental wavelength [Man16]. This section provides an overview of the key physical processes in optical parametric amplification. Section 5.1.1 explains how a broadband supercontinuum can be generated from intense narrowband light pulses in a $\chi^{(3)}$ medium. In section 5.1.2, the principles of parametric amplification are explained and section 5.1.3 covers second-harmonic generation.

### 5.1.1 Supercontinuum generation

To generate new frequencies over a wide spectral range from a narrowband laser fundamental, centred around 291 THz, we use supercontinuum generation [Cou07, Ber07] in a $\chi^{(3)}$ nonlinear crystal. In crystals with inversion-symmetry, $\chi^{(3)}$ is the leading perturbative order, resulting in an **intensity dependent refractive index**. This determines how the refractive index of a material changes as a function of the light intensity and leads to multiple nonlinear phenomena, such as self-phase modulation, self-focusing and self-steepening. Supercontinuum generation is a complex interplay between these effects. Self-phase modulation broadens the pulse's spectrum and self-focusing boosts the intensity by confining the beam profile spatially. Self-steepening further increases the intensity by effectively focusing the pulse in time. At sufficiently high intensities, plasma generation will set in, which defocuses the beam. Multiple cycles of self-focusing and plasma-defocusing guide the light in a highly intense filament. Together, these processes can lead to extreme spectral broadening, resulting in a so-called supercontinuum. In this section, I will explain these nonlinear optical phenomena based on the framework presented in reference [Boy08].

**Intensity-dependent refractive index.** In a nonlinear crystal with vanishing $\chi^{(2)}$ nonlinearity, the first term in the nonlinear polarisation is $P^{(3)}$. Under monochromatic illumination at the frequency $\omega$, and neglecting third-harmonic generation, we

consider only the component of $P^{(3)}$ oscillating at $\omega$. To leading order, the nonlinear polarisation $P^{\mathrm{NL}}$ then becomes [Sal07, Boy08]

$$P^{\mathrm{NL}}(\omega) = 3\epsilon_0\chi^{(3)}(\omega = \omega + \omega - \omega)|E(\omega)|^2 E(\omega). \tag{5.1}$$

Assuming linearly polarised light and an isotropic medium, the tensor nature of $\chi^{(3)}$ can be neglected. Excluding all other nonlinear polarisations, the total material polarisation $P$ can be written as

$$P(\omega) = \epsilon_0\chi^{(1)}E(\omega) + P^{\mathrm{NL}}(\omega) \equiv \epsilon_0\chi_{\mathrm{eff}}E(\omega) \tag{5.2}$$

with the effective susceptibility $\chi_{\mathrm{eff}}$. In general, the refractive index is defined as [Boy08]

$$n^2 = 1 + \chi_{\mathrm{eff}}, \tag{5.3}$$

where the linear refractive index $n_0$ is given by [Boy08]

$$n_0 = \sqrt{1 + \chi^{(1)}}. \tag{5.4}$$

However now, there is also a nonlinear contribution to the refractive index, yielding the intensity dependent refractive index, also known as the optical Kerr effect [Boy08]:

$$n = n_0 + n_2 I, \tag{5.5}$$

where $n_2$ is called the nonlinear refractive index and the intensity $I$ corresponds to [Boy08]

$$I = 2n_0\epsilon_0 c|E(\omega)|^2, \tag{5.6}$$

where $\epsilon_0$ denotes the vacuum permittivity and $c$ the speed of light.

To identify $n_2$, we start by substituting equation 5.5 into equation 5.3, which yields

$$(n_0 + n_2 I)^2 = 1 + \chi^{(1)} + 3\chi^{(3)}|E(\omega)|^2, \tag{5.7}$$

relating the nonlinear refractive index to the nonlinear susceptibility. Using the definition for the intensity from equation 5.6, we receive

$$n_0^2 + 2n_0 n_2 2n_0 \epsilon_0 c|E(\omega)|^2 + O(|E(\omega)|^4) = 1 + \chi^{(1)} + 3\chi^{(3)}|E(\omega)|^2, \tag{5.8}$$

where $O(|E(\omega)|^4)$ denotes all terms scaling with $|E(\omega)|^4$. Neglecting $O(|E(\omega)|^4)$ and solving for $n_2$, we obtain the nonlinear refractive index

$$n_2 = \frac{3\chi^{(3)}}{4n_0^2\epsilon_0 c}. \tag{5.9}$$

The intensity-dependent refractive index has multiple consequences, including the effects of self-phase modulation, self-focusing, and self-steepening which will be discussed in the following.

**Self-phase modulation.** The electric field $E(z,t)$ of a propagating light pulse can be described by

$$E(z,t) = A(z,t)\, e^{i(k_0 z - \omega_0 t)} + \text{c.c.} = A(z,t)\, e^{i\Phi} + \text{c.c.}. \tag{5.10}$$

Here, $A(z,t)$ is the amplitude and $\Phi$ the phase, where $k_0$ is the wave vector, $\omega_0$ the frequency and $z$ and $t$ the space and time coordinate, respectively. When the light pulse propagates through a $\chi^{(3)}$ nonlinear medium, it experiences the intensity dependent refractive index, equation 5.5, leading to a time-dependent wave vector:

$$k(t) = \frac{\omega_0}{c} n(t) = k_0 + \frac{\omega_0}{c} n_2 I(t), \tag{5.11}$$

with $k_0 = \frac{\omega_0}{c} n_0$. This also affects the phase

$$\Phi = k_0 z + \frac{\omega_0}{c} n_2 I(t) z - \omega_0 t \equiv k_0 z - \Phi_{\text{NL}} - \omega_0 t, \tag{5.12}$$

resulting in an additional time-dependent term, the nonlinear phase $\Phi_{\text{NL}}$. Since the instantaneous frequency $\omega(t)$ is defined as [Boy08]

$$\omega(t) = -\frac{\partial \Phi}{\partial t}, \tag{5.13}$$

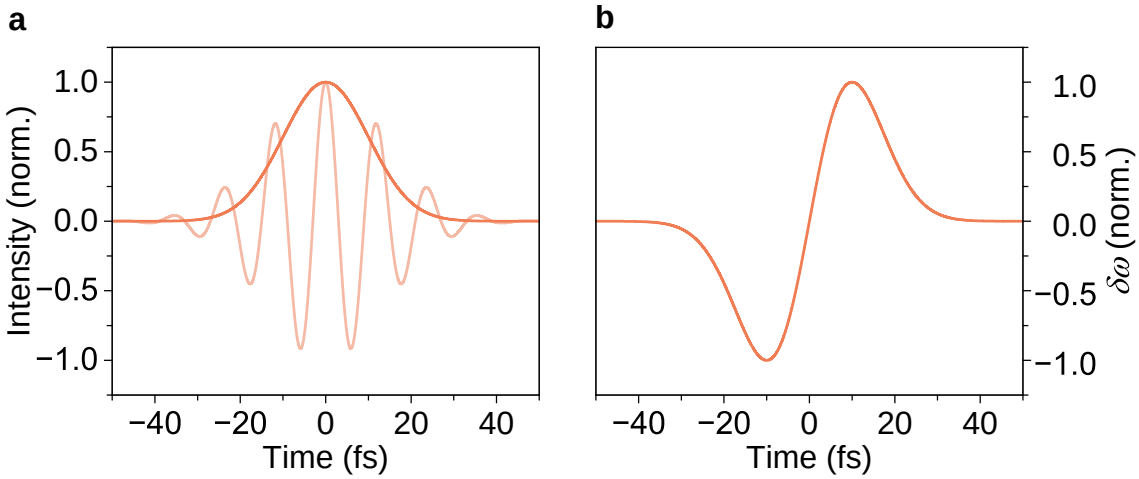


**Figure 5.1 |** Self-phase modulation. **a**, A Gaussian intensity envelope of a femtosecond pulse (orange) with its carrier wave (bright orange) oscillating beneath it. Owing to the optical Kerr effect, the intensity envelope induces a corresponding time-dependent variation in the refractive index. **b**, The time-varying refractive index changes the instantaneous frequency $\delta\omega$ proportional to the negative time-derivative of the intensity envelope. Frequencies arriving earlier are reduced and those which arrive later are increased.

this changes the instantaneous frequency via

$$\omega(t) = \omega_0 + \frac{\mathrm{d}\Phi_{\mathrm{NL}}}{\mathrm{d}t} \equiv \omega_0 + \delta\omega, \tag{5.14}$$

where $\delta\omega$ is the change in instantaneous frequency. Thus, an intense light pulse can alter its own spectral content by modulating its phase – hence the name **self-phase modulation**.

Figure 5.1 shows this effect for a light pulse with a Gaussian intensity envelope. Since the change in instantaneous frequency $\delta\omega$ is proportional to the negative time-derivative of the intensity, early parts of the pulse experience a frequency reduction via a negative $\delta\omega$ and later parts experience a frequency increase. For Fourier limited or positively chirped[1] pulses, which is the most common case, this leads to spectral broadening. Negatively chirped pulses experience spectral narrowing.

[1]Chirp refers to a time-dependent variation in a pulse's instantaneous frequency. For a positively (negatively) chirped pulse, the instantaneous frequency increases (decreases) as a function of time.

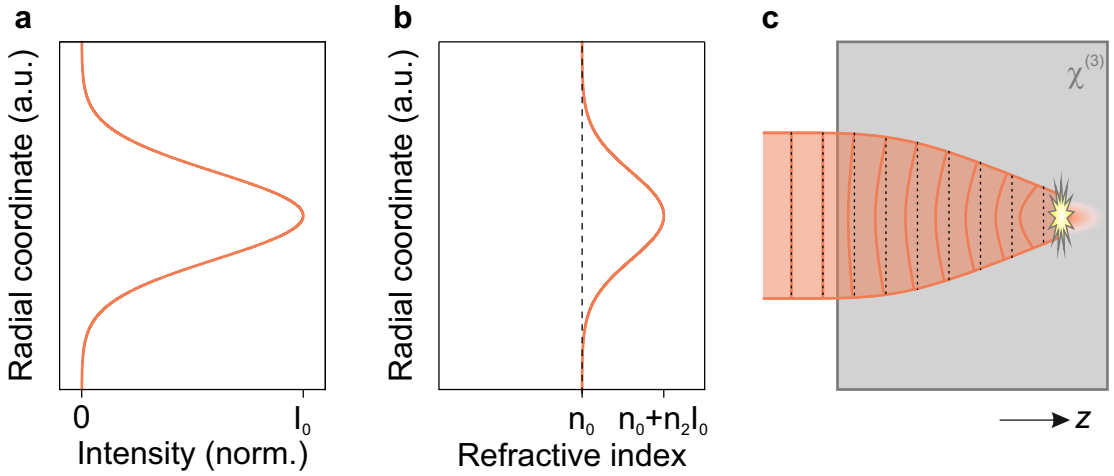


**Figure 5.2 |** Self-focusing. **a**, A Gaussian intensity profile in space induces a corresponding Gaussian-shaped refractive index profile in a $\chi^{(3)}$ medium owing to the intensity-dependent refractive index, **b**. **c**, This refractive-index variation slows down the central part of the Gaussian beam profile relative to the edges, causing the wavefronts to curve inward, focusing the beam. This so-called self-focusing effect increases the intensity, which can facilitate damage in the medium.

**Self-focusing.** According to the intensity-dependent refractive index, a light pulse with a Gaussian spatial intensity profile (Fig. 5.2**a**) experiences a similar spatial profile of the refractive index (Fig. 5.2**b**). As a result, the central part of the beam propagates more slowly than the edges, curving the wavefronts and focusing the beam (Fig. 5.2**c**). This drastically enhances the intensity and can ultimately lead to damage in the $\chi^{(3)}$ medium. Diffraction, however, counteracts the process of self-focusing. The critical power is where diffraction and self-focusing are perfectly balanced. Below it, diffraction dominates, while above it, self-focusing prevails. The critical power $P_{\mathrm{cr}}$ is given by [Boy08]

$$P_{\mathrm{cr}} = \frac{\pi(0.61)^2\lambda_0^2}{8n_0n_2}, \tag{5.15}$$

where $\lambda_0$ is the wavelength in vacuum.

At some point, self-focusing leads to such high intensities that multi-photon absorption begins to set in [Cou07, Ber07]. This process promotes electrons from the valence to

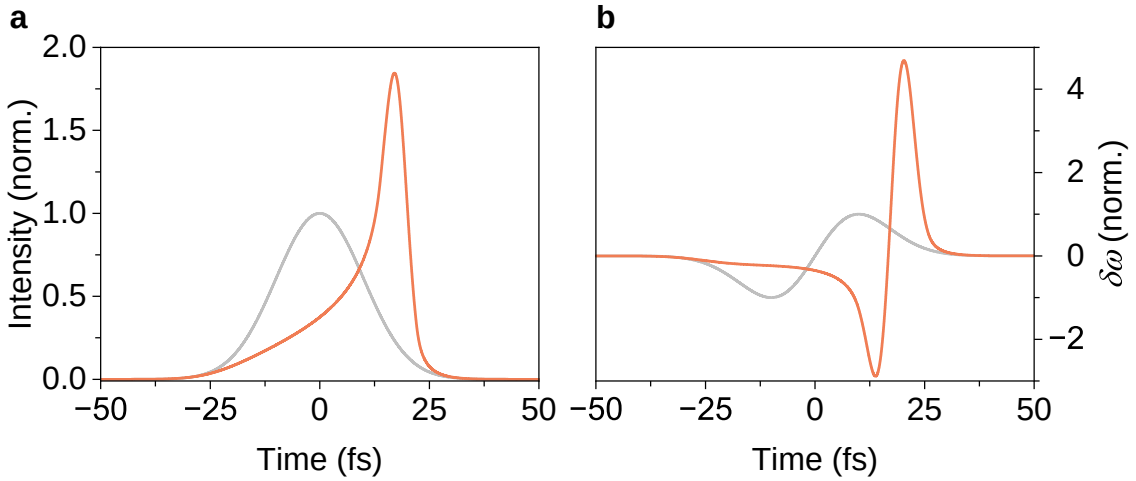


**Figure 5.3 |** Self-steepening. **a**, A laser pulse with a Gaussian intensity envelope (grey) in the time domain experiences a corresponding Gaussian temporal refractive index distribution. This effectively slows down the central part of the pulse with respect to the edges, smoothing out the beginning of the pulse and enhancing the trailing part (orange). **b**, This also alters the change in the instantaneous frequency $\delta\omega$ (orange). Here, the trailing part of the pulse is modulated much more than in the case without self-steepening (grey).

the conduction band, generating a plasma. The plasma counteracts self-focusing by reducing the material's refractive index $n$ according to [Cou07]:

$$n \approx n_0 - \frac{\rho}{2\rho_c}. \tag{5.16}$$

Here, $\rho$ is the plasma density, and $\rho_c$ is the critical plasma density above which the plasma becomes opaque. As a result of the reduction in $n$, the beam defocuses, which halts further plasma generation. This allows self-focusing to dominate again, starting a new cycle of plasma formation and subsequent defocusing. Multiple cycles of self-focusing, plasma generation and defocusing guide the light in a so-called filament [Cou07] – a tightly focused region where the light remains highly confined and maintains an extremely high intensity over an extended propagation distance.

**Self-steepening.** The extreme intensities within such a filament initiate the effect of self-steepening. Owing to the intensity dependent refractive index, a light pulse with a Gaussian temporal intensity envelope experiences a higher refractive index

at its intensity peak than at its edges. As a result, the pulse's peak slows down compared to its leading and trailing edges, distorting the Gaussian shape as shown in Fig. 5.3**a**. While the leading edge of the pulse flattens, the intensity drop at the trailing edge becomes significantly steeper. This altered pulse shape also leads to a modified change of the instantaneous frequency due to self-phase modulation (Fig. 5.3**b**). The leading edge of the pulse undergoes a weaker redshift which increases substantially towards the centre of the pulse. The blueshift at the trailing edge is significantly intensified. Consequently, the spectral broadening exhibits a pronounced asymmetry.

Self-phase modulation and self-steepening within a filament formed by a balance of self-focusing and plasma-defocusing lead to the generation of an extremely broadband but relatively weak supercontinuum. To select a specific spectral region within the supercontinuum and amplify it, we resort to optical parametric amplification.

### 5.1.2 Phase matching in parametric amplification

As seen in equation 3.5 of section 3.2.1, mixing two frequencies $\omega_1$ and $\omega_2$ in a $\chi^{(2)}$ nonlinear crystal can lead to the generation of their difference frequency $\omega_3 = \omega_1 - \omega_2$. In the context of parametric amplification, $\omega_1$ is usually called pump frequency $\omega_\mathrm{p}$, $\omega_2$ is the signal frequency $\omega_\mathrm{s}$, and $\omega_3$ the idler frequency $\omega_\mathrm{i}$. The energy diagram of difference-frequency generation (DFG) is shown in Fig. 5.4**a**. The pump photon is split into a signal photon and an idler photon, amplifying the signal pulses and generating the idler pulses. This is why this process is also referred to as **optical parametric amplification**, a technique that enables the amplification of select spectral regions within extremely broadband yet weak supercontinua.

**Critical phase matching.** Phase matching, i.e. photon momentum conservation (see section 3.2.1), can be achieved by exploiting the polarisation-dependent refractive index in birefringent crystals, which is known as **critical phase matching**.
Here we use BBO as the $\chi^{(2)}$ nonlinear crystal. It features broadband transparency along with a large nonlinear coefficient and allows for phase matching throughout the desired spectral range [Man16]. BBO is a negatively uniaxial birefringent

crystal, which means it possesses a single optic axis where the refractive index for extraordinary polarisation[2], $n_\mathrm{e}$, is smaller than that for ordinary polarisation[3], $n_\mathrm{o}$. If the optic axis is tilted by an angle $\theta_\mathrm{pm}$ with respect to the wave vector $\boldsymbol{k}$, the two refractive indices light can experience in a uniaxial birefringent crystal are $n_\mathrm{o}$ and $n_\mathrm{eo}$, where $n_\mathrm{eo}$ is given by [Sal07]

$$\frac{1}{n_\mathrm{eo}^2(\theta_\mathrm{pm})} = \frac{\sin^2(\theta_\mathrm{pm})}{n_\mathrm{e}^2} + \frac{\cos^2(\theta_\mathrm{pm})}{n_\mathrm{o}^2}. \tag{5.17}$$

By rotating the crystal, the optimal $\theta_\mathrm{pm}$ can be chosen, such that the phase matching condition ($\hbar\Delta\boldsymbol{k} = 0$, equation 3.7) can be fulfilled. Since BBO features normal dispersion, i.e. $\frac{\mathrm{d}n}{\mathrm{d}\omega} > 0$, there are two ways in which phase matching can be achieved.

**Type-I phase matching: eoo.** The wave with the highest frequency, $\omega_1$, is extraordinarily polarised, while the other two waves[4], $\omega_2$ and $\omega_3$, are ordinarily polarised – *eoo*.

**Type-II phase matching: eoe.** The waves with the highest and lowest frequency, $\omega_1$ and $\omega_3$, are extraordinarily polarised, whereas the wave at the intermediate frequency, $\omega_2$, is ordinarily polarised – *eoe*.

Which type of phase matching occurs is governed by the nonlinear tensor $\chi^{(2)}$. For both types of phase matching, the nonlinear tensor can be broken down to effective nonlinearities $d_\mathrm{eff}$. In crystals with the point group 3m, such as BBO, $\chi^{(2)}$ reduces to [Man16]

$$d_\mathrm{eff}^\mathrm{eoo} = d_{31}\sin(\theta) - d_{22}\cos(\theta)\sin(3\phi), \tag{5.18}$$

$$d_\mathrm{eff}^\mathrm{eoe} = d_{22}\cos^2(\theta)\cos(3\phi). \tag{5.19}$$

Here, the azimuthal angle $\phi$ is the angle between the crystal's x-axis and the wave vector's projection onto the x-y plane [Eim87]. From equations 5.18 and 5.19, we find that type-I phase matching occurs when $\phi = 90°$, and type-II phase matching when $\phi = 0°$.

Figure 5.4**b** shows how type-II phase-matched collinear optical parametric amplification is achieved in a BBO crystal. For type-II phase matching, the azimuthal angle $\phi$

[2]Polarisation parallel to the optic axis of the crystal

[3]Polarisation perpendicular to the optic axis of the crystal

[4]Here the convention that the frequency decreases from $\omega_1$ to $\omega_3$ is used.

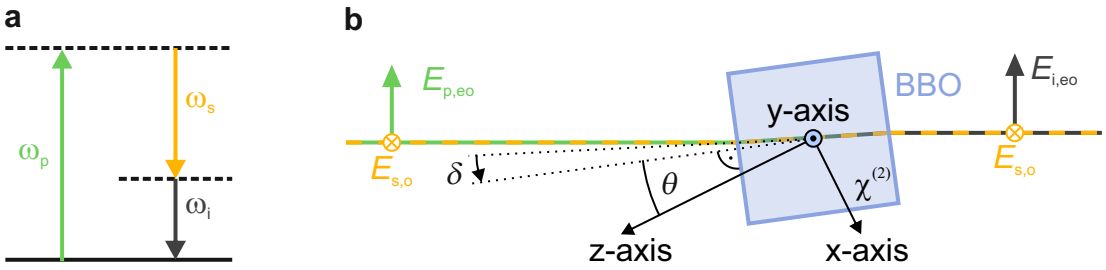


**Figure 5.4 |** Optical parametric amplification. **a**, Energy diagram for difference-frequency generation (DFG). The energy of the pump photon, in this case the second-harmonic photon, is split into a signal photon and an idler photon. $\omega_\mathrm{p}$: Second-harmonic pump frequency, $\omega_\mathrm{s}$: Signal frequency, $\omega_\mathrm{i}$: Idler frequency. **b**, Type-II phase matching for DFG in BBO. The incoming signal wave $E_\mathrm{s,o}$ is polarised perpendicular to the optic axis of the crystal (z-axis), experiencing the ordinary refractive index $n_\mathrm{o}$. The pump wave $E_\mathrm{p,eo}$ is polarised vertically. It thus has a component parallel to the crystal's optic axis and experiences the extraordinary refractive index $n_\mathrm{eo}$. The azimuthal angle $\phi$ between the x-axis and the projection of the wave vector onto the x-y plane is set to 0° for type-II phase matching. The polar angle $\theta$ of the crystal, together with the adjustable angle $\delta$ (which lies between the surface normal and the wave vector in the crystal), forms the internal phase matching angle $\theta_\mathrm{PM}$. The resulting idler field $E_\mathrm{i,eo}$ is extraordinarily polarised, while the amplified signal wave remains ordinarily polarised.

is set to 0°. The incoming signal wave's electric field $E_\mathrm{s,o}$ is polarised perpendicular to the crystal's optic axis (the z-axis), therefore experiencing the ordinary refractive index. The high-frequency pump wave's polarisation ($E_\mathrm{p,eo}$) contains a component parallel to the optic axis and thus experiences the extraordinary refractive index. In type-II phase matching, the newly generated idler wave is polarised extraordinarily. The internal phase matching angle $\theta_\mathrm{pm}$ can be set by adjusting the external rotation angle $\delta$. This allows detuning from the crystal's polar angle $\theta$, determined by the crystal's cut. Due to dispersion, the optimal $\theta_\mathrm{pm}$ varies with the amplified wavelength. Thus, tuning $\theta_\mathrm{pm}$ enables fine control over the amplified spectral range.

**Noncollinear optical parametric amplification.** One key challenge in parametric amplification is the mismatch between the signal and idler group velocities, $v_\mathrm{g,s}$ and $v_\mathrm{g,i}$. This leads to the signal and idler pulses separating in space and time while they propagate through the mixing crystal (Fig. 5.5**a**). Since both of them undergo

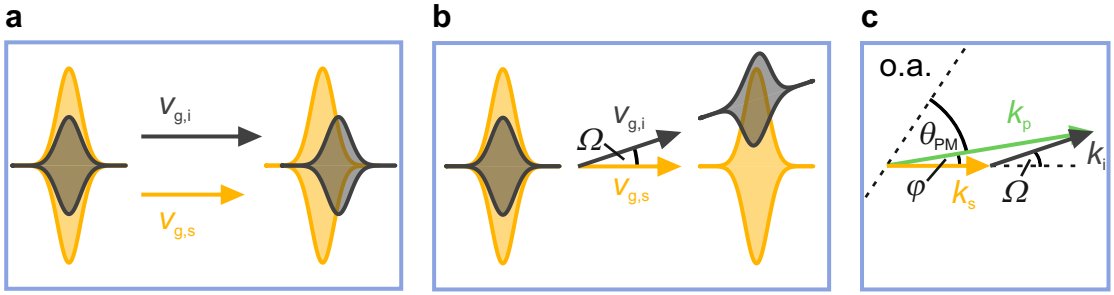


**Figure 5.5 |** Noncollinear optical parametric amplification. **a**, In the $\chi^{(2)}$ nonlinear crystal (blue box), the group velocities of the idler ($v_{g,i}$, dark grey) and the signal ($v_{g,s}$, yellow) pulses differ. As a consequence, they separate in space and time after propagating through the crystal. Since the pump pulse undergoes difference-frequency generation with both the signal and the idler pulse, them separating in time lengthens the duration of the amplified signal pulse. **b**, This temporal elongation is avoided, when the wave vectors are tilted with respect to each other by an angle $\Omega$, such that the projection of the idler's group velocity onto the propagation direction of the signal pulse matches the signal's group velocity. This configuration is called the magic angle. **c**, One can realise this when tilting the pump wave vector $\boldsymbol{k}_p$ with respect to the signal wave vector $\boldsymbol{k}_s$ by an angle $\varphi$, such that by momentum conservation $\Omega$ reaches the magic angle. $\boldsymbol{k}_i$: Idler wave vector, $\theta_{PM}$: Phase-matching angle, o.a.: Optic axis. This figure was inspired by similar figures in [Rie00, Cer03, Man16].

difference-frequency mixing with the pump pulse, each contributing to the generation of the other, this lengthens both the idler and the amplified signal pulses. This effect is counteracted, if the signal and idler pulses interact in a noncollinear fashion. Tilting their wave vectors by an angle $\Omega$ relative to each other allows the projection of $\boldsymbol{v}_{\mathrm{g,i}}$ onto the direction of $\boldsymbol{v}_{\mathrm{g,s}}$ to be matched with $v_{\mathrm{g,s}}$ [Rie00, Cer03, Man16]. This condition is satisfied when:

$$v_{\mathrm{g,s}} = \cos(\Omega) v_{\mathrm{g,i}}. \tag{5.20}$$

This way, the time-separation between signal and idler pulses is counteracted and elongation of the amplified pulses is avoided (Fig. 5.5**b**). This configuration is called magic-angle noncollinear optical parametric amplification and allows for the most broadband phase matching.

This broadband noncollinear optical parametric amplification can be achieved by tilting the pump wave vector $\boldsymbol{k}_{\mathrm{p}}$ with respect to the signal wave vector $\boldsymbol{k}_{\mathrm{s}}$, such that by momentum conservation $\Omega$ matches the magic angle (Fig. 5.5**c**). For this purpose, the angle $\varphi$ between $\boldsymbol{k}_{\mathrm{p}}$ and $\boldsymbol{k}_{\mathrm{s}}$, which we can tune in the experiment, is set to the value determined by [Sch07]

$$\sin(\varphi) = k_{\mathrm{i}} \frac{\sin(\Omega)}{\sqrt{k_{\mathrm{s}}^2 + k_{\mathrm{i}}^2 + 2k_{\mathrm{s}}k_{\mathrm{i}}\cos(\Omega)}}. \tag{5.21}$$

Here, $k_{\mathrm{s}}$ and $k_{\mathrm{i}}$ are the magnitudes of the signal and idler wave vectors $\boldsymbol{k}_{\mathrm{s}}$ and $\boldsymbol{k}_{\mathrm{i}}$, respectively.

### 5.1.3 Second-harmonic generation

For parametric amplification, a source of high frequency photons is necessary to pump the process. Due to energy conservation in difference-frequency generation, $\omega_3 = \omega_1 - \omega_2$, the pump frequency $\omega_1$ has to be higher than both the signal and the idler frequency. To reach photon energies which correspond to the resonances of (moiré) excitons in TMDCs, which typically lie below 2.4 eV [Wan18], we can use the second harmonic of the centre frequency of our ytterbium-fibre amplifier as pump pulses (photon energy: 2.4 eV). Thus, we resort to second-harmonic generation in a $\chi^{(2)}$ nonlinear crystal, $\beta$-barium borate (BBO).

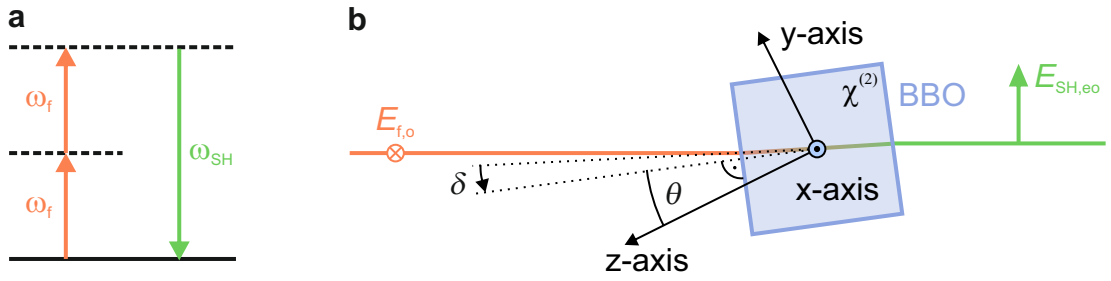


**Figure 5.6 |** Second-harmonic generation. **a**, Energy diagram for SHG. Two photons of the fundamental frequency $\omega_\mathrm{f}$ (orange) are converted to one photon at the second-harmonic frequency $\omega_\mathrm{SH}$. **b**, Type-I phase matching for SHG in a $\chi^{(2)}$ nonlinear BBO crystal. The polarisation of the incoming NIR electric field $E_\mathrm{f,o}$ is perpendicular to the crystal's optic axis (z-axis), resulting in ordinary polarisation. With cut-angles $\phi = 90°$ and $\theta = 23.5°$, the BBO crystal is configured for type-I phase matching. Rotating the crystal around the x-axis adjusts the angle $\delta$, allowing for tuning of the phase-matching angle $\theta_\mathrm{PM} = \theta + \delta = 23.4°$. The generated second-harmonic field $E_\mathrm{SH,eo}$ is vertically polarised, featuring a component parallel to the optic axis leading to extraordinary polarisation.

The nonlinear polarisation in a $\chi^{(2)}$ nonlinear crystal, as seen in equation 3.5, contains spectral components oscillating at twice the incoming laser frequency, which is referred to as *second-harmonic generation* (SHG). Figure 5.6**a** shows the energy diagram of SHG. Two photons of the fundamental frequency $\omega_\mathrm{f}$ combine to one photon at the second-harmonic frequency $\omega_\mathrm{SH} = 2\omega_\mathrm{f}$. To perform SHG, we use type-I phase matching achieved in a BBO crystal as shown in Fig. 5.6**b**. The polarisation of the incident NIR pulse's electric field $E_\mathrm{f,o}$ is perpendicular to the crystal's optic axis, resulting in ordinary polarisation. The crystal is cut for type-I phase matching, i.e. $\phi = 90°$, with a polar angle of $\theta = 23.5°$. We fine-tune the phase-matching condition by rotating the crystal around its x-axis, adjusting the angle $\delta$. This allows precise control of the phase-matching angle, $\theta_\mathrm{pm} = \theta + \delta = 23.4°$, optimising the conversion process. The resulting second-harmonic field, $E_\mathrm{SH,eo}$, is polarised vertically, i.e. features extraordinary polarisation.

## 5.2 A two-stage noncollinear optical parametric amplifier at megahertz repetition rates

Having laid the theoretical foundation by detailing the processes relevant in optical parametric amplification in the previous sections, this section demonstrates how we leverage these effects to experimentally realise a tunable optical pump source operating at a high pulse repetition rate of 8.26 MHz.

To achieve this, we have designed a NOPA consisting of two amplification stages, as sketched in Fig. 5.7. We start with the ytterbium-fibre amplifier used in the previous chapters (centre wavelength $\lambda_c = 1030\,\mathrm{nm}$, pulse duration $\tau = 260\,\mathrm{fs}$). We operate at a pulse repetition rate of 8.26 MHz, the highest repetition rate at which we found supercontinuum generation to be stable. The NOPA requires an input pulse energy of $\varepsilon = 2.1\,\mu\mathrm{J}$. A half-wave plate and a thin-film polariser split the NIR pulses into two arms: (i) the supercontinuum arm and (ii) the SHG arm of the NOPA. The reflected part, arm (i), consisting of $0.54\,\mu\mathrm{J}$ is used for supercontinuum generation. There, the pulses are focused into a $\chi^{(3)}$ medium, an yttrium aluminium garnet (YAG) crystal with a thickness of 5 mm. YAG crystals feature a comparatively large nonlinear refractive index of $n_2 = 6.2 \times 10^{-16}\,\mathrm{cm^2\,W^{-1}}$ [Dub17] and have been shown to be resistant to optical damage even for supercontinuum generation at high repetition rates [Gri20]. A lens with a focal length of $f = 50\,\mathrm{mm}$ focuses the pulses, reaching a peak intensity of $\sim 14\,\mathrm{GW\,cm^{-2}}$ at the entrance facet of the YAG crystal. This ignites a filament which generates a supercontinuum spanning from the infrared to the visible range. Since we aim to amplify only the short-wavelength part of this supercontinuum, we filter out the long-wavelength components including the residual laser fundamental using a short-pass filter with a cut-off wavelength of 950 nm. The spectral intensity of the filtered supercontinuum covers the wavelength range from 950 nm to 575 nm (Fig. 5.8**a**), and gradually decreases as the wavelength deviates further from the laser fundamental of 1030 nm. A lens with $f = 25\,\mathrm{mm}$, positioned directly behind the YAG crystal, refocuses the supercontinuum into the first NOPA stage.

The part that is transmitted through the thin-film polariser, arm (ii), consisting of the remaining $1.56\,\mu\mathrm{J}$ of pulse energy, generates the pump pulses via SHG in a BBO crystal with a thickness of 1.2 mm cut for type-I phase matching ($\varphi = 90°$, $\theta = 23.5°$).

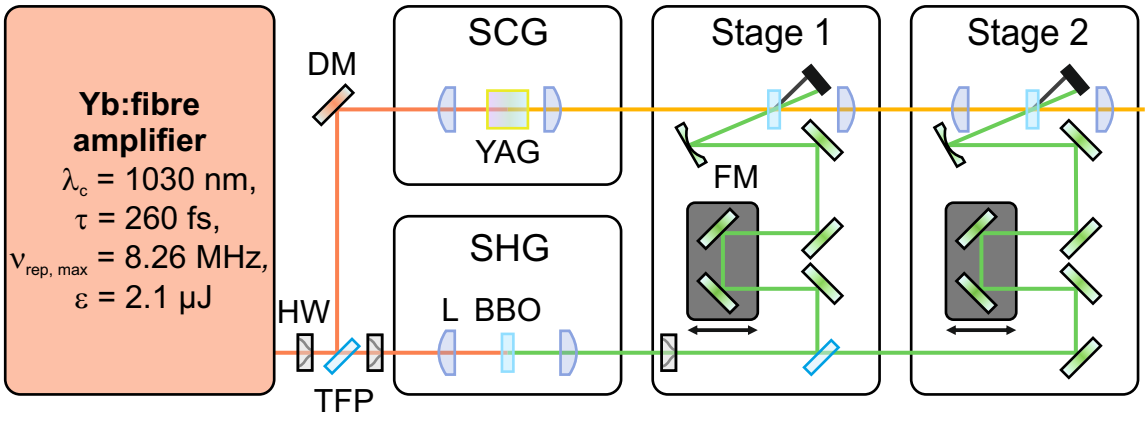


**Figure 5.7** | Schematic setup of the two-stage noncollinear optical parametric amplifier. Pulses from an ytterbium-fibre amplifier with a centre wavelength of 1030 nm, pulse duration of 260 fs, maximum repetition rate of 8.26 MHz and a pulse energy of $\epsilon = 2.1\,\mu J$ are used for noncollinear optical parametric amplification. The pulses are split into two arms via a half-wave plate (HW) and a thin-film polariser (TFP). 1.56 µJ are used to generate the second harmonic in a BBO with a thickness of 1.2 mm and cut for type-1 phase matching. A conversion efficiency of 62% leads to 1 µJ of the second harmonic which is sent as pump pulses into the two amplification stages with approximately equal power. The other 0.54 µJ of the fundamental are used to generate a supercontinuum in a YAG crystal with a thickness of 5 mm which is subsequently amplified in stage 1 and stage 2 via optical parametric amplification. The time overlap between the supercontinuum signal pulses and the second-harmonic pump pulses is tuned via a delay stage in each amplification stage. DM: Dielectric mirror, L: Lens, FM: Focusing mirror, SCG: Supercontinuum generation, SHG: Second-harmonic generation.

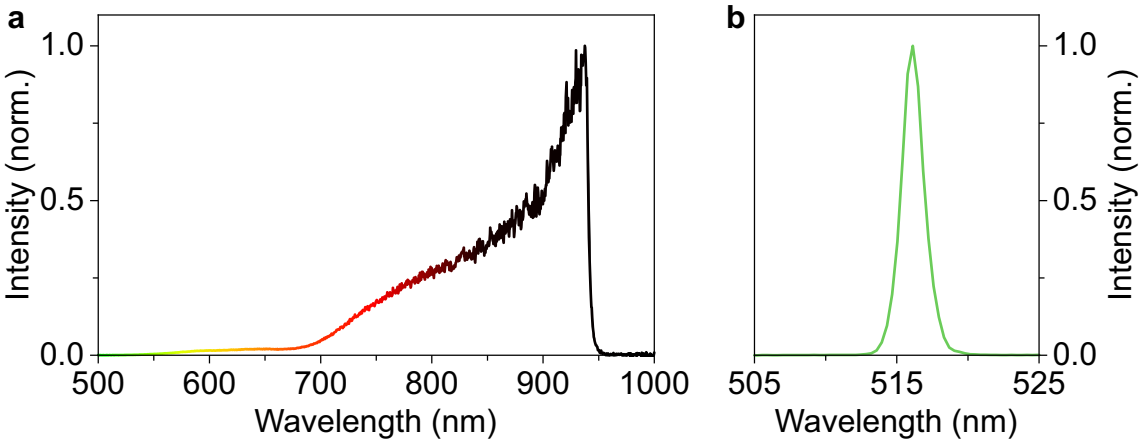


**Figure 5.8 |** Supercontinuum and second-harmonic spectra. **a**, The spectral intensity of the short-wavelength part of the supercontinuum reaches as far as 575 nm, whereas the long-wavelength part is filtered out with a short-pass filter with a cut-off wavelength of 950 nm. **b**, The spectral intensity of the second-harmonic pulses is centred at 516 nm and features a FWHM bandwidth of 3 nm.

This results in the spectral intensity depicted in Fig. 5.8**b**, centred at 516 nm with a FWHM bandwidth of 3 nm. With a NIR peak intensity of 13.5 GW cm$^{-2}$ we achieve a power conversion efficiency of 62%, resulting in a pump-pulse energy of 1 µJ.

The pump pulses are split into the two NOPA stages with the combination of a half-wave plate and a thin-film polariser. The pump-splitting ratio can be tuned to optimise the conversion efficiency of the OPA process. We found the best splitting ratio to be $\sim 50:50$. Any residual spectral components at the laser's fundamental wavelength are filtered out by the dielectric mirrors along the following beam path which have a high-reflectivity coating for a wavelength of 515 nm but not for the fundamental wavelength.

In the first NOPA stage (stage 1), the supercontinuum and the pump pulses are spatio-temporally overlapped in a BBO crystal ($\theta = 26.5°$, $\phi = 0°$) with a thickness of 5 mm leading to optical parametric amplification. Owing to the noncollinearity with a pump-tilt angle of $\sim 3°$, idler and pump pulses can be easily blocked after amplification. The signal pulses are further amplified in the second NOPA stage (stage 2) in an identical BBO. The pump pulses are focused into the two stages using lenses with focal lengths of $f = 250$ mm and $f = 300$ mm, leading to peak intensities of 3 GW cm$^{-2}$ and 2.6 GW cm$^{-2}$, respectively. In both amplification stages, the time-

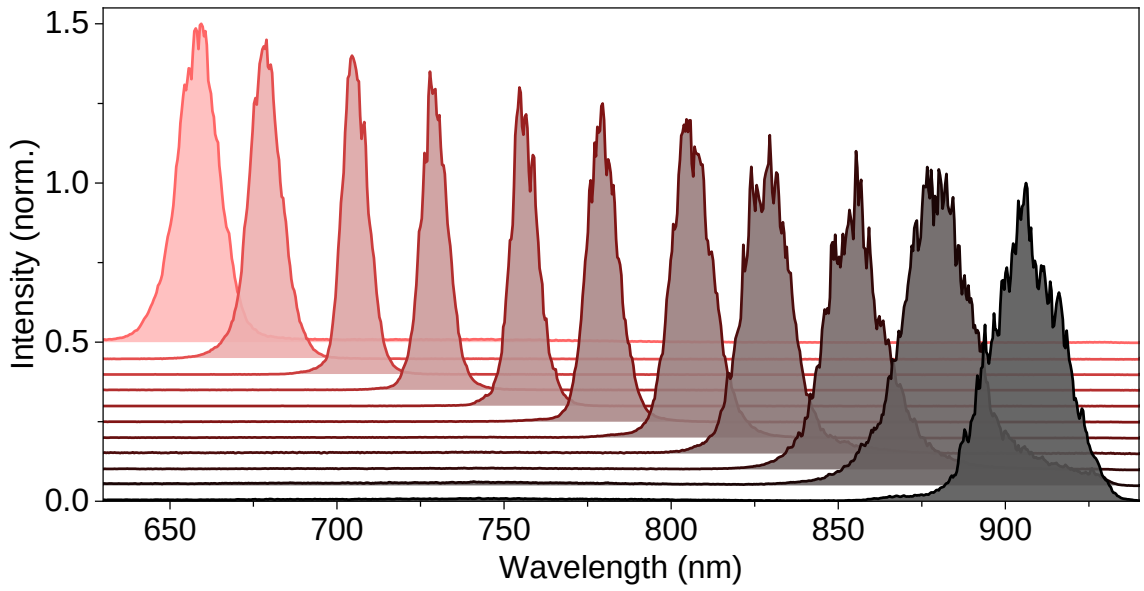


**Figure 5.9 |** NOPA output spectra after the two-stage amplification demonstrating the spectral tunability. The plot shows the normalised spectral intensity after both NOPA stages for central wavelengths between 650 nm and 900 nm, in steps of ∼25 nm. The spectra are offset vertically in increments of 0.05 for clarity.

overlap is tuned using a delay stage, and the phase-matching conditions are optimised by tilting the crystal. This allows us to choose which spectral region to amplify. Using two amplification stages enables operation in a regime of pump depletion, which greatly enhances the stability of OPAs, as it is less sensitive to fluctuations in the supercontinuum seed pulses [Cer03]. Typically, quantum efficiencies[5] of 30% or higher are used. We achieved a quantum efficiency of ∼39% when amplifying at a centre wavelength of 730 nm.

Figure 5.9 shows the spectral intensity after two NOPA stages tuned to different spectral amplification regions. We find that we are able to produce more than 100 mW of average power in the entire spectral range reaching from 650 nm to 900 nm. At a pulse repetition rate of 8.26 MHz, this relates to a pulse energy of ∼12 nJ. At even shorter wavelengths, amplification is drastically reduced in BBO crystals owing to absorption of the idler pulses, which sets in at wavelengths of ∼3 µm [Eim87].

[5]The fraction of pump photons undergoing difference-frequency generation

## 5.3 Constant-power pump modulation

To trace the ultrafast dynamics induced by pump pulses in pump-probe experiments, the pump-pulse train has to be modulated for lock-in detection. In most far-field experiments, this is achieved by mechanically chopping the beam. For higher modulation frequencies, acousto-optic modulators are often employed. Irrespective of the technique, usually the modulation cycle consists of a part where the light is turned on and one part where it is turned off. This changes the thermal load on the system throughout the modulation cycle. For experiments with atomic-scale tip-sample separation, such thermal fluctuations can be detrimental.
Whereas at THz frequencies, the influence of thermal effects on STM tips is negligible [Aza24], in the visible and NIR spectral ranges, tip heating can significantly alter the tunnelling junction [Gra98, Hub98, Ger00, Aza24]. [Gra98] investigated tip expansion at different modulation frequencies for continuous-wave irradiation. They estimated the expansion of a tungsten tip to be $\sim 10\,\mathrm{pm\,mW^{-1}}$ in the best case scenario, at a modulation frequency of 100 kHz. [Ger00] argues on the basis of finite element simulations, that previous studies with pulsed lasers, finding a tip expansion of a few nanometres for microjoule pulse energies, may have underestimated tip expansion by more than an order of magnitude, owing to their limited detection bandwidths.
To avoid this issue entirely, it is essential to modulate the pump-pulse train without changing the thermal load on the tunnelling junction. We have therefore developed a new modulation scheme which does not change the average power incident on the tip throughout the modulation cycle. Instead, this scheme is based on changing the relative timing of pump and probe pulses.

**Shaken-pulse-pair optical pumping.** To investigate pump-induced changes in NOTE signals while retaining atomic resolution, we developed a pump-modulation scheme based on the idea of shaken-pulse-pair modulation [Tak02, Tak05]. In this approach, the timing of the pump pulses is modulated by changing the optical path length periodically via an end mirror on a piezoelectric stage. In these studies, timing modulations in the range of picoseconds were achieved at modulation frequencies of a few hertz.

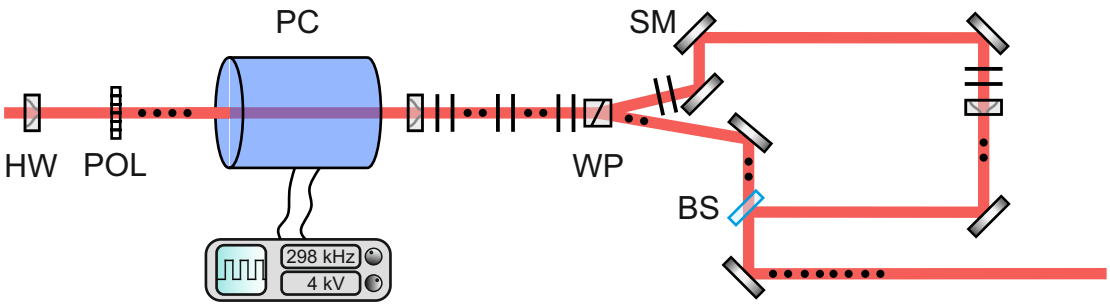


**Figure 5.10 |** Shaken-pulse-pair pump-modulation scheme. To modulate the timing of the pump pulses, we use a Pockels cell (PC) in half-wave operation which periodically switches the polarisation of the pump pulses (red) from s-polarisation (black dots) to p-polarisation (black stripes). Depending on their polarisation, the pump pulses are split onto two different beam paths with different lengths via a Wollaston prism (WP). In the longer path, a half-wave plate turns the polarisation by 90° such that when recombining via a beam splitter (BS), both paths have the same polarisation. A half-wave plate (HW) and linear polariser (POL) before the PC are used to reduce the pump power to below its damage threshold and to align the polarisation with the PC's orientation. The PC's driver sends a high-voltage signal, allowing modulation at frequencies of up to 300 kHz. SM: Silver mirror.

To combine this approach with significantly higher modulation frequencies for improved signal-to-noise ratios, we developed a similar modulation scheme using a Pockels cell (PC) and polarisation optics to periodically direct the pump pulses along two different beam paths (Fig. 5.10). The difference in beam paths ensures that half of the time, the pump pulses arrive before the probe pulses, leading to a pump-induced change in the scattered light. The other half of the time, the pump pulses arrive after the probe pulses and thus do not influence the detected light. This way, the average power on the tip-sample junction remains constant, while the periodic presence and absence of the pump-induced signal enables its detection with a lock-in amplifier.

To achieve this, the PC is operated in half-wave mode and switches the pump-pulse polarisation strictly between s-polarised and p-polarised at frequencies of up to 300 kHz. A Wollaston prism then spatially separates the s- and p-polarised pulse trains onto two beam paths with different lengths. The difference in path lengths is chosen to be $\sim 500$ mm such that even pump-probe delay times of up to 1.5 ns are achievable before pulses from the longer pump path start to temporally overlap

with the probe pulses. The polarisation in the longer path is turned by 90° with a half-wave plate such that upon recombination with a beam splitter both pulse trains have the same polarisation.
The PC's medium consists of two BBO crystals with a thickness of 20 mm each. This introduces significant dispersion into the setup. At a wavelength of 730 nm, the ordinary refractive index of BBO has a group velocity dispersion of $\sim 83\,\mathrm{fs}^2\,\mathrm{mm}^{-1}$ [Eim87] – the total group delay dispersion from the Pockels cell alone would amount to $\sim 3300\,\mathrm{fs}^2$. Including the dispersion introduced by the other dispersive optics in the pump beam path, we estimate a total group delay dispersion on the order of $5000\,\mathrm{fs}^2$. To compensate for the dispersion, my colleagues *Felix Schiegl* and *Svenja Nerreter* implemented a prism compressor, reducing the pulse duration to $\sim 70$ fs.

## 5.4 Experimental setup for ultrafast pump-probe near-field optical tunnelling emission microscopy

Figure 5.11 depicts the entire setup for ultrafast NOTE, including the optical pump path. The THz generation, the microscope and EOS remain as described in chapter 3. The optical pump path consists of the two-stage NOPA, the novel pump modulation scheme and a prism compressor. The pump-probe delay time is adjusted with a motorised stage. THz and pump pulses are overlapped with a quartz window coated with a thin layer of indium tin oxide. This window is transparent for visible and NIR light but reflects THz radiation. The co-propagating THz and pump pulses are focused to the apex of the tungsten tip. The pump-polarisation is set perpendicular to the tip to minimise tip-coupling and thereby reduce pump-induced thermal effects. Light coherently scattered from the tip is detected via EOS. Any residual pump light is filtered out with a germanium wafer, which transmits THz radiation while absorbing visible light.
Owing to the long pump-propagation path ($\sim 10$ m), astigmatism in the pump beam profile, originating from the noncollinear geometry in the parametric amplification, must be corrected. To achieve this, we employ a spatial filter consisting of a pinhole (diameter 30 µm) placed at the focal plane between two lenses, each with a focal

length of $f = 50\,\mathrm{mm}$. Due to this mode clean-up and multiple reflection losses along the optical path, the pump power at the entrance window of the microscope is reduced to $\sim 5\,\mathrm{mW}$ ($\sim 0.6\,\mathrm{nJ}$ pulse energy).
With the high-NA parabolic mirrors in the microscope, we can achieve beam waists with a $1/e^2$ intensity radius of $\sim 1.5\,\mu\mathrm{m}$ at the tip's apex. Thus an average power of $\sim 0.6\,\mathrm{mW}$ would suffice to reach a pump fluence of $1\,\mathrm{mJ\,cm^{-2}}$. Typical pump fluences in previous ultrafast THz-SNOM experiments were on the order of $100\,\mu\mathrm{J\,cm^{-2}}$ [Pla21, Sid22]. For excitons in TMDCs, pump fluences below $30\,\mu\mathrm{J\,cm^{-2}}$ have already been shown to generate exciton densities high enough for excitons to dissociate into a plasma of electrons and holes [Sid22]. Thus, even taking into account the reflection loss at the diamond entrance window ($\sim 30\%$), the remaining pump power is more than sufficient for our planned experiments.

With the development of the optical setup complete, we have established the foundation for ultrafast optical pump—NOTE probe microscopy across a wide range of material systems. This opens an entirely new avenue for exploring ultrafast dynamics at the atomic scale and paves the way for deeper insights into light–matter interaction on its intrinsic time and length scales. I am truly excited to see the groundbreaking physical discoveries that will be made with this unique setup, and I sincerely hope it will bring to life the vision of directly observing the formation of moiré excitons in space and time.

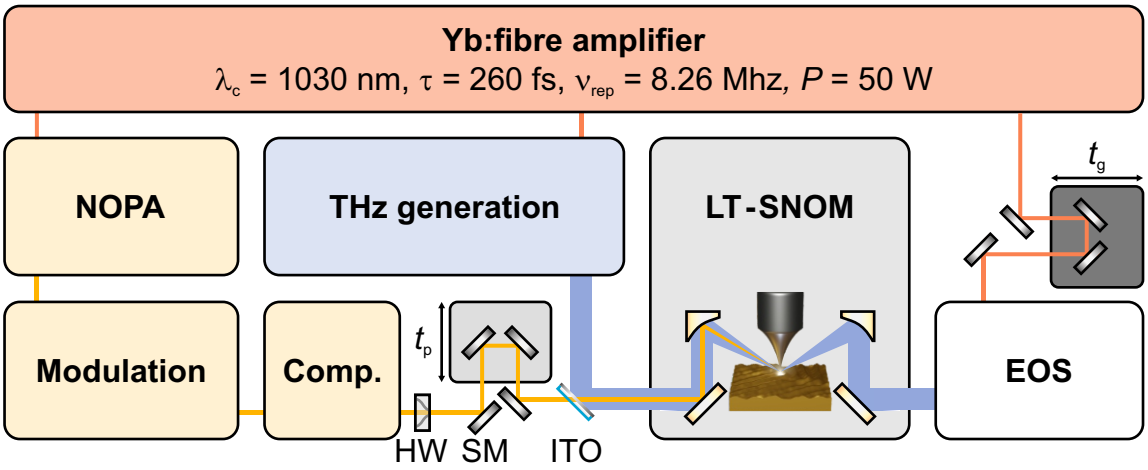


**Figure 5.11 |** Full setup schematic, including the optical pump path. Pulses from the ytterbium-fibre amplifier serve as seed pulses for the pump and THz generation and as the gate pulses for electro-optic sampling (EOS). The optical pump path (yellow boxes) consists of the two-stage NOPA, the shaken-pulse-pair pump-modulation scheme and a prism compressor (Comp.). The pump-delay stage sets the pump-probe delay time $t_p$. After THz generation, THz and pump pulses are spatially overlapped with a quartz window coated with a thin layer of indium tin oxide (ITO) and both are coupled to the low-temperature SNOM (LT-SNOM) tip's apex. To reduce the effect of pump-induced tip heating, a half-wave plate (HW) sets the pump polarisation orthogonal to the tip. Light scattered from the tip coherently is detected via EOS. SM: Silver mirror.

Chapter 6

# Conclusion

In this thesis, I have shown how we can leverage light emission from atomically confined lightwave-driven tunnelling currents to bring all-optical microscopy to simultaneous atomic-scale spatial and subcycle time resolution.

In chapter 2, I introduced two cornerstones of ultrafast nanoscopy – lightwave-STM and ultrafast SNOM – which both offer unique advantages. While SNOM enables subcycle time resolution via electro-optic sampling, the extreme stability of low-temperature UHV lightwave-STM allows for atomic spatial resolution.

Aiming to combine the strengths of both techniques, we set out to establish subcycle THz-SNOM under the stable conditions of low-temperature UHV STM. To this end, we developed an entirely new state-of-the-art experimental setup. The optical setup consists of a high-power, phase-locked terahertz source operating at MHz pulse repetition rates based on tilted-pulse-front optical rectification in lithium niobate. We merged the optical setup with a combined STM/AFM which features custom high-NA optical access, and operates at cryogenic temperatures in UHV. The microscope is equipped with a stiff qPlus sensor – allowing for picometric tapping amplitudes – with an atomically sharp tungsten tip. We focus the THz pulses onto the apex of this tip and detect the coherently scattered radiation with subcycle resolution via EOS.

I explained how we harnessed novel atomic-scale near-field signals originating from subcycle tunnelling currents to perform all-optical subcycle atomic-scale microscopy and spectroscopy, granting access to subcycle tunnelling dynamics. Using our unique

setup, we explored the near-field interaction at atomic-scale tip-sample separations. We observed that, as the tip approaches the sample, the scattered light undergoes a phase-shift of $\sim\pi/2$ and the signal amplitude increases significantly at atomic tip-sample separations. Moreover, when employing picometric tip-tapping amplitudes, we found that this phase-shifted signal decays on the same length scale as lightwave-driven tunnelling currents.

Using a semiclassical dipole model, we successfully reproduced the hallmark features of this signal. We attribute this novel short-ranged signal to a transient dipole in the tip formed by tunnelling electrons driven by the ultrafast lightwave bias. Since charge accumulation follows the integral over the tunnelling current, this dipole is phase-shifted by $\pi/2$ with respect to both the driving field and the conventional near field, which oscillates in phase with the driving field. This picture was further supported by *ab initio* TDDFT simulations performed by *Jan Wilhelm*. Having recognised that this novel optical signal is emitted from ultrafast tunnelling currents driven by the near fields, we termed it **N**ear-field **O**ptical **T**unnelling **E**mission (NOTE).

We showcased the capabilities of this new technique by imaging a nanometre-sized defect in a Au(111) surface, revealing that the spatial resolution of NOTE follows that of lightwave-STM. By sweeping the THz electric field strength and tracking the peak of the NOTE signal in EOS, we traced out the onset of the valence band of a monolayer of $WSe_2$ on Au(111), demonstrating the first atomic-scale subcycle spectroscopy. A key advantage of NOTE is its all-optical nature, enabling subcycle resolution. As it does not require time-averaged rectified tunnelling currents, NOTE is not limited to conductive samples. We demonstrated this on a semiconducting quantum material: a trilayer of $WSe_2$ on Au(111). By tracing the NOTE signal in tunnelling contact, and accounting for the tip-transfer function and detector response, we retrieved the NOTE dipole at the tip apex. Since, according to our model, the NOTE dipole forms as an integral over the ultrafast tunnelling currents, differentiating the dipole allowed us to extract the instantaneous tunnelling currents directly in the time domain. This approach provides a radical new means of probing light-matter interaction on atomic length and subcycle time scales, promising to unravel the inner workings of condensed matter.

To enable the investigation of pump-induced dynamics – such as moiré exciton formation – via NOTE, we expanded the capabilities of our experimental setup by developing a tunable optical pump source. Building on optical parametric amplification, we designed a two-stage noncollinear optical parametric amplifier, which can be operated at pulse repetition rates as high as 8.26 MHz. This system allows for tuning the centre wavelength of the pump pulses between 650 nm and 900 nm. To prevent measurement artefacts caused by changing the thermal load on the tip when modulating the pump pulses, we developed a new modulation scheme. There, instead of simply turning the pump pulses on and off, we periodically shift the timing of the pump pulses so that they alternately interact with the sample before the probe pulse arrives or too late to have any influence on the measurement.

**Outlook: Unravelling the quantum world in motion.** With the unprecedented subcycle temporal and atomic-scale spatial resolution of NOTE, we are now in an ideal position to unravel many of the pressing questions in condensed matter physics. With tunable ultrafast optical excitation, we can now investigate the formation dynamics and lifetimes of excitons directly in space and time. Moiré heterostructures of TMDCs provide a periodically modulated potential landscape for excitons [Kar22, Sch22], and we may be able to observe excitons becoming trapped in potential minima or at atomic-scale defects.

Exploiting the temperature tunability of our microscope, we can also explore a wide range of phase transitions. Phase transitions in correlated electron systems – such as in charge-density-wave materials [Por14, Ger19, Che20], or insulator-to-metal transitions [Hub16] – are often driven by the interplay of many-body interactions. Our approach offers direct access to the microscopic dynamics underlying such phase transitions in both space and time. We could also investigate the ultrafast melting and formation of Wigner crystals [Zho21], where strong Coulomb correlations drive electrons into an ordered lattice-like structure.

Many more fascinating quantum phases can be obtained in twisted van der Waals heterostructures [Ken21]. With our approach, we can now access these phenomena on their intrinsic time and length scales.

**Outlook: Towards attosecond resolution.** We expect NOTE to be frequency-scalable, potentially even reaching attosecond resolution. EOS has already been demonstrated across the infrared spectral range [Sel08, Kei16] and was recently extended into the visible domain [Rid22]. Moreover, the emission intensity of a dipole follows an $\omega^4$ dependence [Jac62], where $\omega$ is the angular frequency, making an extension of NOTE into the near-infrared regime particularly promising.
Crucially, attosecond pulses are not a prerequisite for attosecond precision, as demonstrated in a recent experiment [Fre22]. In this study, the authors used phase-locked mid-infrared waveforms to force coherent electron-hole pairs along closed quantum trajectories, and clocked their dynamics with attosecond precision. A similar strategy could be feasible for NOTE, where the relatively low centre frequencies in the mid-infrared spectral range would ensure operation in a field-driven regime.
Ultimately, increasing the driving frequency while simultaneously broadening the EOS bandwidth could unlock access to previously unattainable ultrafast dynamics.

**Outlook: NOTE from continuous-wave-driven tunnelling currents.** Since NOTE does not require net currents, it does not require an asymmetric tunnelling conductance within the lightwave-bias window. Thus, even with a relatively small a.c. lightwave bias – as from a continuous-wave source – a subcycle a.c. tunnelling current may flow if the tip is sufficiently close to the sample, potentially leading to light emission. In fact, initial indications of this effect have already appeared in earlier experiments where we used a mid-infrared quantum-cascade laser as the light source. In these experiments, the phase of the scattered signal – obtained in continuous-wave SNOM via interferometric pseudo-heterodyne detection [Oce06] – shifted at atomic tip-sample separations and the signal decayed on the length scale of tunnelling currents. Now, with a deeper understanding of NOTE, we are actively investigating this phenomenon further.

# Scientific record

## Publications in peer-reviewed journals

- Thomas Siday*, Johannes Hayes*, Felix Schiegl*, Fabian Sandner, Peter Menden, Valentin Bergbauer, Martin Zizlsperger, Svenja Nerreter, Sonja Lingl, Jascha Repp, Jan Wilhelm, Markus A. Huber, Yaroslav A. Gerasimenko & Rupert Huber
  * equal contributions
  **All-optical subcycle microscopy on atomic length scales**
  *Nature* **629**, 329-334 (2024) | DOI: 10.1038/s41586-024-07355-7

  This paper was featured in a research briefing
  **Quantum tunnelling of electrons brings ultrafast optical microscopy to the atomic scale**
  *Nature* | DOI: 10.1038/d41586-024-01294-z

- Christian Meineke*, Michael Prager*, Johannes Hayes, Qiannan Wen*, Lukas Z. Kastner, Dieter Schuh, Kilian Fritsch, Oleg Pronin, Markus Stein, Felix Schäfer, Sangam Chatterjee, Mackillo Kira, Rupert Huber & Dominique Bougeard
  * equal contributions
  **Scalable high-repetition-rate sub-half-cycle terahertz pulses from spatially indirect interband transitions**
  *Light: Science & Applications* **11**, 151 (2022) |
  DOI: 10.1038/s41377-022-00824-6

- Dominik Peller*, Carmen Roelcke, Lukas Z. Kastner, Thomas Buchner, Alexander Neef, Johannes Hayes, Franco Bonafé*, Dominik Sidler, Michael Ruggenthaler, Angel Rubio, Rupert Huber & Jascha Repp
  * equal contributions
  **Quantitative sampling of atomic-scale electromagnetic waveforms**
  *Nature Photonics* **15**, 143-147 (2021) | DOI: 10.1038/s41566-020-00720-8

- Sebastian Smyk, Vitali Telezki, Josef Riepl, Johannes Hayes & Stefan Klumpp
  **Orientation fluctuations in magnetotactic swimming**
  *The European Physical Journal Special Topics* **230**, 1099-1103 (2021) |
  DOI: 10.1140/epjs/s11734-021-00078-0

# Patent applications

- Rupert Huber, Thomas Siday, Iaroslav Gerasimenko, Felix Schiegl, Johannes Martin Hayes, Markus Andreas Huber & Jan Wilhelm
  **Optische Nahfeld-Tunnelemissions-Mikroskopie**
  DE 10 2024 108 203.8
  EP 25 163 001.8

# Publications in international conference proceedings

- Felix Schiegl, Thomas Siday, Johannes Hayes, Fabian Sandner, Peter Menden, Valentin Bergbauer, Martin Zizlsperger, Svenja Nerreter, Sonja Lingl, Jascha Repp, Jan Wilhelm, Markus A. Huber, Yaroslav A. Gerasimenko & Rupert Huber
  **All-optical microscopy with combined subcycle temporal and atomic-scale spatial resolution**
  *SPIE OPTO, 2025*
  DOI: 10.1117/12.3051117

- Johannes Hayes, Thomas Siday, Felix Schiegl, Fabian Sandner, Peter Menden, Valentin Bergbauer, Martin Zizlsperger, Svenja Nerreter, Sonja Lingl, Jascha Repp, Jan Wilhelm, Markus A. Huber, Yaroslav A. Gerasimenko & Rupert Huber
  **Subcycle scanning near-field terahertz microscopy reaching atomic resolution**
  *49th International Conference on Infrared, Millimeter, and Terahertz Waves*
  DOI: 10.1109/IRMMW-THz60956.2024.10697787

- Johannes Hayes, Thomas Siday, Felix Schiegl, Fabian Sandner, Peter Menden, Valentin Bergbauer, Martin Zizlsperger, Svenja Nerreter, Sonja Lingl, Jascha Repp, Jan Wilhelm, Markus A. Huber, Yaroslav A. Gerasimenko & Rupert Huber
  **All-Optical Subcycle Microscopy at the Atomic Scale**
  *2024 Conference on Lasers and Electro-Optics (CLEO)*
  DOI: 10.1364/CLEO_FS.2024.FTh5B.6

- Felix Schiegl, Thomas Siday, Johannes Hayes, Peter Menden, Valentin Bergbauer, Svenja Nerreter, Sonja Lingl, Jan Wilhelm, Markus A. Huber, Yaroslav A. Gerasimenko & Rupert Huber
  **Subcycle optical microscopy with Angstrom-scale resolution**

*Optical Engineering + Applications, 2024*
DOI: 10.1117/12.3029407

- Christian Meineke, Michael Prager, Johannes Hayes, Qiannan Wen, Lukas Z. Kastner, Dominique Bougeard, Mackillo Kira & Rupert Huber
  **Intense Sub-Half-Cycle Terahertz Waveforms for Lightwave-Driven Scanning Tunnelling Microscopy**
  *23rd International Conference on Transparent Optical Networks (ICTON 2023)*
  DOI: 10.1109/ICTON59386.2023.10207294

- Qiannan Wen, Christian Meineke, Michael Prager, Johannes Hayes, Lukas Z. Kastner, Dieter Schuh, Kilian Fritsch, Oleg Pronin, Markus Stein, Felix Schäfer, Sangam Chatterjee, Dominique Bougeard, Rupert Huber & Mackillo Kira
  **Unipolar pulse generation from heterostructure charging dynamics**
  *2023 Conference on Lasers and Electro-Optics (CLEO)*
  DOI: 10.1364/CLEO_FS.2023.FF3B.6

- Carmen Roelcke, Dominik Peller, Lukas Z. Kastner, Thomas Buchner, Alexander Neef, Johannes Hayes, Franco Bonafé, Dominik Sidler, Michael Ruggenthaler, Angel Rubio, Jascha Repp & Rupert Huber
  **Quantitative Sampling of Atom-Scale Terahertz Waveforms**
  *47th International Conference on Infrared, Millimeter and Terahertz Waves*
  DOI: 10.1109/IRMMW-THz50927.2022.9895809

- Christian Meineke, Michael Prager, Johannes Hayes, Qiannan Wen, Lukas Z. Kastner, Dieter Schuh, Kilian Fritsch, Oleg Pronin, Markus Stein, Felix Schäfer, Sangam Chatterjee, Mackillo Kira, Dominique Bougeard & Rupert Huber
  **A flexible high-repetition-rate source of sub-half-cycle terahertz pulses based on spatially indirect interband transitions**
  *47th International Conference on Infrared, Millimeter and Terahertz Waves*
  DOI: 10.1109/IRMMW-THz50927.2022.9895658

- Carmen Roelcke, Dominik Peller, Lukas Z. Kastner, Thomas Buchner, Alexander Neef, Johannes Hayes, Franco Bonafé, Dominik Sidler, Michael Ruggenthaler, Angel Rubio, Jascha Repp & Rupert Huber
  **Quantitative Waveform Sampling on Atomic Scales**
  *2021 Conference on Lasers and Electro-Optics (CLEO)*
  DOI: 10.1364/CLEO_QELS.2021.FTh1K.6

# Contributions at conferences as presenting author

- **49th International Conference on Infrared, Millimeter, and Terahertz Waves**
  1 – 6 September 2024 | Perth, Australia
  *Keynote talk*
  Johannes Hayes, Thomas Siday, Felix Schiegl, Fabian Sandner, Peter Menden, Valentin Bergbauer, Martin Zizlsperger, Svenja Nerreter, Sonja Lingl, Jascha Repp, Jan Wilhelm, Markus A. Huber, Yaroslav A. Gerasimenko & Rupert Huber
  **Subcycle scanning near-field terahertz microscopy reaching atomic resolution**
  This contribution was awarded second place in the Best Student Presentation Award competition, selected from over 100 applications.

- **23rd International Conference on Ultrafast Phenomena**
  14 – 19 July 2024 | Barcelona, Spain
  *Contributed talk*
  Johannes Hayes, Thomas Siday, Felix Schiegl, Fabian Sandner, Peter Menden, Valentin Bergbauer, Martin Zizlsperger, Svenja Nerreter, Sonja Lingl, Jascha Repp, Jan Wilhelm, Markus A. Huber, Yaroslav A. Gerasimenko & Rupert Huber
  **All-Optical Subcycle Microscopy with Atomic-Scale Resolution**

- **XI International Symposium on Ultrafast Dynamics & Ultrafast Bandgap Photonics**
  16 – 22 June 2024 | Hersonissos, Crete, Greece
  *Invited talk*
  Johannes Hayes, Thomas Siday, Felix Schiegl, Fabian Sandner, Peter Menden, Valentin Bergbauer, Martin Zizlsperger, Svenja Nerreter, Sonja Lingl, Jascha Repp, Jan Wilhelm, Markus A. Huber, Yaroslav A. Gerasimenko & Rupert Huber
  **Clocking the subcycle dynamics of atomically confined tunnelling currents**

- **2024 Conference on Lasers and Electro-Optics (CLEO)**
  5 – 10 May 2024 | Charlotte, North Carolina, USA
  *Post-deadline talk*
  Johannes Hayes, Thomas Siday, Felix Schiegl, Fabian Sandner, Peter Menden, Valentin Bergbauer, Martin Zizlsperger, Svenja Nerreter, Sonja Lingl, Jascha Repp, Jan Wilhelm, Markus A. Huber, Yaroslav A. Gerasimenko & Rupert Huber
  **All-Optical Subcycle Microscopy at the Atomic Scale**

- **Internal workshop of SFB 1277 – Emergent Relativistic Effects in Condensed Matter**
  26 – 27 October 2020 | Virtual conference
  *Contributed talk*
  Johannes Hayes, Dominik Peller, Carmen Roelcke, Lukas Z. Kastner, Thomas Buchner, Alexander Neef, Dominik Sidler, Franco Bonafé, Michael Ruggenthaler, Angel Rubio, Christian Meineke, Michael Prager, Dieter Schuh, Dominique Bougeard, Rupert Huber & Jascha Repp
  **Generation and atomic-scale quantitative sampling of intense half-cycle terahertz transients**

# Bibliography

[Abb73] E. Abbe, *Beiträge zur Theorie des Mikroskops und der mikroskopischen Wahrnehmung*, Archiv für Mikroskopische Anatomie **9**, 413–468 (1873).

[Amm21] S. E. Ammerman, V. Jelic, Y. Wei, V. N. Breslin, M. Hassan, N. Everett, S. Lee, Q. Sun, C. A. Pignedoli, P. Ruffieux, R. Fasel, and T. L. Cocker, *Lightwave-driven scanning tunnelling spectroscopy of atomically precise graphene nanoribbons*, Nature Communications **12**, 6794 (2021).

[Amm22] S. E. Ammerman, Y. Wei, N. Everett, V. Jelic, and T. L. Cocker, *Algorithm for subcycle terahertz scanning tunneling spectroscopy*, Physical Review B **105**, 115427 (2022).

[Ang25] S. Anglhuber, M. Zizlsperger, E. A. A. Pogna, Y. A. Gerasimenko, A. D. Koulouklidis, I. Gronwald, S. Nerreter, L. Viti, M. S. Vitiello, R. Huber, and M. A. Huber, *Spacetime Imaging of Group and Phase Velocities of Terahertz Surface Plasmon Polaritons in Graphene*, Nano Letters **25**, 2125–2132 (2025).

[Ara22] Y. Arashida, H. Mogi, M. Ishikawa, I. Igarashi, A. Hatanaka, N. Umeda, J. Peng, S. Yoshida, O. Takeuchi, and H. Shigekawa, *Subcycle Mid-Infrared Electric-Field-Driven Scanning Tunneling Microscopy with a Time Resolution Higher Than 30 fs*, ACS Photonics **9**, 3156–3164 (2022).

[Ash72] E. A. Ash and G. Nicholls, *Super-resolution Aperture Scanning Microscope*, Nature **237**, 510–512 (1972).

[Aza24] H. Azazoglu, R. Möller, and M. Gruber, *Thermal expansion in photo-assisted tunneling: Visible light versus free-space terahertz pulses*, Surface Science **743**, 122465 (2024).

[Bak07] M. I. Bakunov, S. B. Bodrov, A. V. Maslov, and M. Hangyo, *Theory of terahertz generation in a slab of electro-optic material using an ultrashort laser pulse focused to a line*, Physical Review B **76**, 085346 (2007).

[Bal20] L. Balents, C. R. Dean, D. K. Efetov, and A. F. Young, *Superconductivity and strong correlations in moiré flat bands*, Nature Physics **16**, 725–733 (2020).

[Bar57] J. Bardeen, L. N. Cooper, and J. R. Schrieffer, *Theory of Superconductivity*, Physical Review **108**, 1175–1204 (1957).

[Bas11] D. N. Basov, R. D. Averitt, D. van der Marel, M. Dressel, and K. Haule, *Electrodynamics of correlated electron materials*, Reviews of Modern Physics **83**, 471–541 (2011).

[Bas16] D. N. Basov, M. M. Fogler, and F. J. García de Abajo, *Polaritons in van der Waals materials*, Science **354**, aag1992 (2016).

[Bas21] D. N. Basov, A. Asenjo-Garcia, P. J. Schuck, X. Zhu, and A. Rubio, *Polariton panorama*, Nanophotonics **10**, 549–577 (2021).

[BC19] I. C. Benea-Chelmus, F. F. Settembrini, G. Scalari, and J. Faist, *Electric field correlation measurements on the electromagnetic vacuum state*, Nature **568**, 202–206 (2019).

[Ber07] L. Bergé, S. Skupin, R. Nuter, J. Kasparian, and J.-P. Wolf, *Ultrashort filaments of light in weakly ionized, optically transparent media*, Reports on Progress in Physics **70**, 1633–1713 (2007).

[Bet92] E. Betzig and J. K. Trautman, *Near-Field Optics: Microscopy, Spectroscopy, and Surface Modification Beyond the Diffraction Limit*, Science **257**, 189–195 (1992).

[Bin82] G. Binnig, H. Rohrer, C. Gerber, and E. Weibel, *Surface Studies by Scanning Tunneling Microscopy*, Physical Review Letters **49**, 57–61 (1982).

[Bin83] G. Binnig, H. Rohrer, C. Gerber, and E. Weibel, *7 × 7 Reconstruction on Si(111) Resolved in Real Space*, Physical Review Letters **50**, 120–123 (1983).

[Bin86] G. Binnig, C. F. Quate, and C. Gerber, *Atomic Force Microscope*, Physical Review Letters **56**, 930–933 (1986).

[Bio21] M. R. Bionta, F. Ritzkowsky, M. Turchetti, Y. Yang, D. Cattozzo Mor, W. P. Putnam, F. X. Kärtner, K. K. Berggren, and P. D. Keathley, *On-chip sampling of optical fields with attosecond resolution*, Nature Photonics **15**, 456–460 (2021).

[Bla07] F. Blanchard, L. Razzari, H. Bandulet, G. Sharma, R. Morandotti, J. C. Kieffer, T. Ozaki, M. Reid, H. F. Tiedje, H. K. Haugen, and F. A. Hegmann, *Generation of 1.5 μJ single-cycle terahertz pulses by optical rectification from a large aperture ZnTe crystal*, Optics Express **15**, 13212–13220 (2007).

[Boo22] T. Boolakee, C. Heide, A. Garzón-Ramírez, H. B. Weber, I. Franco, and P. Hommelhoff, *Light-field control of real and virtual charge carriers*, Nature **605**, 251–255 (2022).

[Bor20] M. Borsch, C. P. Schmid, L. Weigl, S. Schlauderer, N. Hofmann, C. Lange, J. T. Steiner, S. W. Koch, R. Huber, and M. Kira, *Super-resolution lightwave tomography of electronic bands in quantum materials*, Science **370**, 1204–1207 (2020).

[Bor23] M. Borsch, M. Meierhofer, R. Huber, and M. Kira, *Lightwave electronics in condensed matter*, Nature Reviews Materials **8**, 668–687 (2023).

[Boy08] R. W. Boyd, *Nonlinear Optics*, 3rd ed., Academic Press, Inc., 2008.

[Bre05] J. Breidbach and L. S. Cederbaum, *Universal Attosecond Response to the Removal of an Electron*, Physical Review Letters **94**, 033901 (2005).

[Cao18] Y. Cao, V. Fatemi, S. Fang, K. Watanabe, T. Taniguchi, E. Kaxiras, and

P. Jarillo-Herrero, *Unconventional superconductivity in magic-angle graphene superlattices*, Nature **556**, 43–50 (2018).

[Cer03] G. Cerullo and S. De Silvestri, *Ultrafast optical parametric amplifiers*, Review of Scientific Instruments **74**, 1–18 (2003).

[Che12] J. Chen, M. Badioli, P. Alonso-González, S. Thongrattanasiri, F. Huth, J. Osmond, M. Spasenović, A. Centeno, A. Pesquera, P. Godignon, A. Zurutuza Elorza, N. Camara, F. J. García, R. Hillenbrand, and F. H. Koppens, *Optical nano-imaging of gate-tunable graphene plasmons*, Nature **487**, 77–81 (2012).

[Che14] A. Chernikov, T. C. Berkelbach, H. M. Hill, A. Rigosi, Y. Li, B. Aslan, D. R. Reichman, M. S. Hybertsen, and T. F. Heinz, *Exciton Binding Energy and Nonhydrogenic Rydberg Series in Monolayer $WS_2$*, Physical Review Letters **113**, 076802 (2014).

[Che19a] G. Chen, L. Jiang, S. Wu, B. Lyu, H. Li, B. L. Chittari, K. Watanabe, T. Taniguchi, Z. Shi, J. Jung, Y. Zhang, and F. Wang, *Evidence of a gate-tunable Mott insulator in a trilayer graphene moiré superlattice*, Nature Physics **15**, 237–241 (2019).

[Che19b] X. Chen, D. Hu, R. Mescall, G. You, D. N. Basov, Q. Dai, and M. Liu, *Modern Scattering-Type Scanning Near-Field Optical Microscopy for Advanced Material Research*, Advanced Materials **31**, 1804774 (2019).

[Che20] Y. Chen, W. Ruan, M. Wu, S. Tang, H. Ryu, H.-Z. Tsai, R. L. Lee, S. Kahn, F. Liou, C. Jia, O. R. Albertini, H. Xiong, T. Jia, Z. Liu, J. A. Sobota, A. Y. Liu, J. E. Moore, Z.-X. Shen, S. G. Louie, S.-K. Mo, and M. F. Crommie, *Strong correlations and orbital texture in single-layer 1T-$TaSe_2$*, Nature Physics **16**, 218–224 (2020).

[Che21] C. J. Chen, *Introduction to Scanning Tunneling Microscopy*, 3rd ed., Oxford University Press, 2021.

[Coc13] T. L. Cocker, V. Jelic, M. Gupta, S. J. Molesky, J. A. Burgess, G. D. L. Reyes, L. V. Titova, Y. Y. Tsui, M. R. Freeman, and F. A. Hegmann,

*An ultrafast terahertz scanning tunnelling microscope*, Nature Photonics **7**, 620–625 (2013).

[Coc16] T. L. Cocker, D. Peller, P. Yu, J. Repp, and R. Huber, *Tracking the ultrafast motion of a single molecule by femtosecond orbital imaging*, Nature **539**, 263–267 (2016).

[Cor07] P. B. Corkum and F. Krausz, *Attosecond science*, Nature Physics **3**, 381–387 (2007).

[Cos16] J. C. Costa, R. J. Taveira, C. F. Lima, A. Mendes, and L. M. Santos, *Optical band gaps of organic semiconductor materials*, Optical Materials **58**, 51–60 (2016).

[Cou07] A. Couairon and A. Mysyrowicz, *Femtosecond filamentation in transparent media*, Physics Reports **441**, 47–189 (2007).

[Cur22] D. Curcio, K. Volckaert, D. Kutnyakhov, S. Y. Agustsson, K. Bühlmann, F. Pressacco, M. Heber, S. Dziarzhytski, Y. Acremann, J. Demsar, W. Wurth, C. E. Sanders, and P. Hofmann, *Tracking the surface atomic motion in a coherent phonon oscillation*, Physical Review B **106**, L201409 (2022).

[Dah12] J. M. Dahlström, A. L'Huillier, and A. Maquet, *Introduction to attosecond delays in photoionization*, Journal of Physics B: Atomic, Molecular and Optical Physics **45**, 183001 (2012).

[Dan24] M. Dantus, *Ultrafast studies of elusive chemical reactions in the gas phase*, Science **385**, eadk1833 (2024).

[Dar02] S. B. Darling, A. W. Rosenbaum, Y. Wang, and S. J. Sibener, *Coexistence of the (23 × √3) Au(111) Reconstruction and a Striped Phase Self-Assembled Monolayer*, Langmuir **18**, 7462–7468 (2002).

[Dhi17] S. S. Dhillon, M. S. Vitiello, E. H. Linfield, A. G. Davies, M. C. Hoffmann, J. Booske, C. Paoloni, M. Gensch, P. Weightman, G. P. Williams, E. Castro-Camus, D. R. S. Cumming, F. Simoens, I. Escorcia-Carranza, J. Grant, S. Lucyszyn, M. Kuwata-Gonokami, K. Konishi, M. Koch, C. A.

Schmuttenmaer, T. L. Cocker, R. Huber, A. G. Markelz, Z. D. Taylor, V. P. Wallace, J. Axel Zeitler, J. Sibik, T. M. Korter, B. Ellison, S. Rea, P. Goldsmith, K. B. Cooper, R. Appleby, D. Pardo, P. G. Huggard, V. Krozer, H. Shams, M. Fice, C. Renaud, A. Seeds, A. Stöhr, M. Naftaly, N. Ridler, R. Clarke, J. E. Cunningham, and M. B. Johnston, *The 2017 terahertz science and technology roadmap*, Journal of Physics D: Applied Physics **50**, 043001 (2017).

[Don21] Y. Dong, L. Xiong, I. Y. Phinney, Z. Sun, R. Jing, A. S. McLeod, S. Zhang, S. Liu, F. L. Ruta, H. Gao, Z. Dong, R. Pan, J. H. Edgar, P. Jarillo-Herrero, L. S. Levitov, A. J. Millis, M. M. Fogler, D. A. Bandurin, and D. N. Basov, *Fizeau drag in graphene plasmonics*, Nature **594**, 513–516 (2021).

[Dub17] A. Dubietis, G. Tamošauskas, R. Šuminas, V. Jukna, and A. Couairon, *Ultrafast Supercontinuum Generation in Bulk*, Lithuanian Journal of Physics **57**, 113–157 (2017).

[Eim87] D. Eimerl, L. Davis, S. Velsko, E. K. Graham, and A. Zalkin, *Optical, mechanical, and thermal properties of barium borate*, Journal of Applied Physics **62**, 1968–1983 (1987).

[Eis14] M. Eisele, T. L. Cocker, M. A. Huber, M. Plankl, L. Viti, D. Ercolani, L. Sorba, M. S. Vitiello, and R. Huber, *Ultrafast multi-terahertz nano-spectroscopy with sub-cycle temporal resolution*, Nature Photonics **8**, 841–845 (2014).

[Esm19] M. Esmann, S. F. Becker, J. Witt, J. Zhan, A. Chimeh, A. Korte, J. Zhong, R. Vogelgesang, G. Wittstock, and C. Lienau, *Vectorial near-field coupling*, Nature Nanotechnology **14**, 698–704 (2019).

[Fal11] R. Falcone, C. Jacobsen, J. Kirz, S. Marchesini, D. Shapiro, and J. Spence, *New directions in X-ray microscopy*, Contemporary Physics **52**, 293–318 (2011).

[Fat12] H. Fattahi, C. Y. Teisset, O. Pronin, A. Sugita, R. Graf, V. Pervak, X. Gu,

T. Metzger, Z. Major, F. Krausz, and A. Apolonski, *Pump-seed synchronization for MHz repetition rate, high-power optical parametric chirped pulse amplification*, Optics Express **20**, 9833–9840 (2012).

[Fei12] Z. Fei, A. S. Rodin, G. O. Andreev, W. Bao, A. S. McLeod, M. Wagner, L. M. Zhang, Z. Zhao, M. Thiemens, G. Dominguez, M. M. Fogler, A. H. C. Neto, C. N. Lau, F. Keilmann, and D. N. Basov, *Gate-tuning of graphene plasmons revealed by infrared nano-imaging*, Nature **487**, 82–85 (2012).

[Fre22] J. Freudenstein, M. Borsch, M. Meierhofer, D. Afanasiev, C. P. Schmid, F. Sandner, M. Liebich, A. Girnghuber, M. Knorr, M. Kira, and R. Huber, *Attosecond clocking of correlations between Bloch electrons*, Nature **610**, 290–295 (2022).

[Fül20] J. A. Fülöp, S. Tzortzakis, and T. Kampfrath, *Laser-Driven Strong-Field Terahertz Sources*, Advanced Optical Materials **8**, 1900681 (2020).

[Gar22] M. Garg, A. Martin-Jimenez, M. Pisarra, Y. Luo, F. Martín, and K. Kern, *Real-space subfemtosecond imaging of quantum electronic coherences in molecules*, Nature Photonics **16**, 196–202 (2022).

[Gei13] A. K. Geim and I. V. Grigorieva, *Van der Waals heterostructures*, Nature **499**, 419–425 (2013).

[Ger00] V. Gerstner, A. Thon, and W. Pfeiffer, *Thermal effects in pulsed laser assisted scanning tunneling microscopy*, Journal of Applied Physics **87**, 2574–2580 (2000).

[Ger19] Y. A. Gerasimenko, P. Karpov, I. Vaskivskyi, S. Brazovskii, and D. Mihailovic, *Intertwined chiral charge orders and topological stabilization of the light-induced state of a prototypical transition metal dichalcogenide*, npj Quantum Materials **4**, 32 (2019).

[Ges04] H. Gest, *The discovery of microorganisms by Robert Hooke and Antoni van Leeuwenhoek, Fellows of The Royal Society*, Notes and Records of the Royal Society of London **58**, 187–201 (2004).

[Gie03] F. J. Giessibl, *Advances in atomic force microscopy*, Reviews of Modern Physics **75**, 949–983 (2003).

[Gie19] F. J. Giessibl, *The qPlus sensor, a powerful core for the atomic force microscope*, Review of Scientific Instruments **90**, 011101 (2019).

[Gra98] S. Grafström, P. Schuller, J. Kowalski, and R. Neumann, *Thermal expansion of scanning tunneling microscopy tips under laser illumination*, Journal of Applied Physics **83**, 3453–3460 (1998).

[Gre14] M. A. Green, A. Ho-Baillie, and H. J. Snaith, *The emergence of perovskite solar cells*, Nature Photonics **8**, 506–514 (2014).

[Gri20] R. Grigutis, G. Tamošauskas, V. Jukna, A. Risos, and A. Dubietis, *Supercontinuum generation and optical damage of sapphire and YAG at high repetition rates*, Optics Letters **45**, 4507–4510 (2020).

[Gro11] L. Gross, N. Moll, F. Mohn, A. Curioni, G. Meyer, F. Hanke, and M. Persson, *High-Resolution Molecular Orbital Imaging Using a p-Wave STM Tip*, Physical Review Letters **107**, 086101 (2011).

[Heb96] J. Hebling, *Derivation of the pulse front tilt caused by angular dispersion*, Optical and Quantum Electronics **28**, 1759–1763 (1996).

[Heb02] J. Hebling, G. Almasi, I. Kozma, and J. Kuhl, *Velocity matching by pulse front tilting for large area THz-pulse generation*, Optics Express **10**, 1161–1166 (2002).

[Heb04] J. Hebling, A. Stepanov, G. Almási, B. Bartal, and J. Kuhl, *Tunable THz pulse generation by optical rectification of ultrashort laser pulses with tilted pulse fronts*, Applied Physics B: Lasers and Optics **78**, 593–599 (2004).

[Hek20] N. Hekmat, T. Vogel, Y. Wang, S. Mansourzadeh, F. Aslani, A. Omar, M. Hoffmann, F. Meyer, and C. J. Saraceno, *Cryogenically cooled GaP for optical rectification at high excitation average powers*, Optical Materials Express **10**, 2768–2782 (2020).

[Hel07] S. W. Hell, *Far-Field Optical Nanoscopy*, Science **316**, 1153–1158 (2007).

[Hil25] R. Hillenbrand, Y. Abate, M. Liu, X. Chen, and D. N. Basov, *Visible-to-THz near-field nanoscopy*, Nature Reviews Materials **10**, 285–310 (2025).

[Hoh15] M. Hohenleutner, F. Langer, O. Schubert, M. Knorr, U. Huttner, S. W. Koch, M. Kira, and R. Huber, *Real-time observation of interfering crystal electrons in high-harmonic generation*, Nature **523**, 572–575 (2015).

[Hoo65] R. Hooke, *Micrographia: or some Physiological Descriptions of Minute Bodies made by Magnifying Glasses with Observations and Inquiries thereupon*, Jo. Martyn and Ja. Allestry, Printers to the Royal Society, London, 1665.

[Hu20] G. Hu, Q. Ou, G. Si, Y. Wu, J. Wu, Z. Dai, A. Krasnok, Y. Mazor, Q. Zhang, Q. Bao, C. W. Qiu, and A. Alù, *Topological polaritons and photonic magic angles in twisted $\alpha$-$MoO_3$ bilayers*, Nature **582**, 209–213 (2020).

[Hua13] S.-W. Huang, E. Granados, W. R. Huang, K.-H. Hong, L. E. Zapata, and F. X. Kärtner, *High conversion efficiency, high energy terahertz pulses by optical rectification in cryogenically cooled lithium niobate*, Optics Letters **38**, 796–798 (2013).

[Hua22] D. Huang, J. Choi, C.-K. Shih, and X. Li, *Excitons in semiconductor moiré superlattices*, Nature Nanotechnology **17**, 227–238 (2022).

[Hub98] R. Huber, M. Koch, and J. Feldmann, *Laser-induced thermal expansion of a scanning tunneling microscope tip measured with an atomic force microscope cantilever*, Applied Physics Letters **73**, 2521–2523 (1998).

[Hub00] R. Huber, A. Brodschelm, F. Tauser, and A. Leitenstorfer, *Generation and field-resolved detection of femtosecond electromagnetic pulses tunable up to 41 THz*, Applied Physics Letters **76**, 3191–3193 (2000).

[Hub01] R. Huber, F. Tauser, A. Brodschelm, M. Bichler, G. Abstreiter, and A. Leitenstorfer, *How many-particle interactions develop after ultrafast excitation of an electron-hole plasma*, Nature **414**, 286–289 (2001).

[Hub16] M. A. Huber, M. Plankl, M. Eisele, R. E. Marvel, F. Sandner, T. Korn,

C. Schüller, R. F. Haglund, R. Huber, and T. L. Cocker, *Ultrafast Mid-Infrared Nanoscopy of Strained Vanadium Dioxide Nanobeams*, Nano Letters **16**, 1421–1427 (2016).

[Hub17] M. A. Huber, F. Mooshammer, M. Plankl, L. Viti, F. Sandner, L. Z. Kastner, T. Frank, J. Fabian, M. S. Vitiello, T. L. Cocker, and R. Huber, *Femtosecond photo-switching of interface polaritons in black phosphorus heterostructures*, Nature Nanotechnology **12**, 207–211 (2017).

[Jac62] J. D. Jackson, *Classical Electrodynamics*, John Wiley & Sons, Inc., 1962.

[Jel17] V. Jelic, K. Iwaszczuk, P. H. Nguyen, C. Rathje, G. J. Hornig, H. M. Sharum, J. R. Hoffman, M. R. Freeman, and F. A. Hegmann, *Ultrafast terahertz control of extreme tunnel currents through single atoms on a silicon surface*, Nature Physics **13**, 591–598 (2017).

[Jel24] V. Jelic, S. Adams, M. Hassan, K. Cleland-Host, S. E. Ammerman, and T. L. Cocker, *Atomic-scale terahertz time-domain spectroscopy*, Nature Photonics **18**, 898–904 (2024).

[Jia19] T. Jiang, V. Kravtsov, M. Tokman, A. Belyanin, and M. B. Raschke, *Ultrafast coherent nonlinear nanooptics and nanoimaging of graphene*, Nature Nanotechnology **14**, 838–843 (2019).

[Jin21] R. Jing, Y. Shao, Z. Fei, C. F. B. Lo, R. A. Vitalone, F. L. Ruta, J. Staunton, W. J. Zheng, A. S. Mcleod, Z. Sun, B. Jiang, X. Chen, M. M. Fogler, A. J. Millis, M. Liu, D. H. Cobden, X. Xu, and D. N. Basov, *Terahertz response of monolayer and few-layer $WTe_2$ at the nanoscale*, Nature Communications **12**, 5594 (2021).

[Kam07] T. Kampfrath, J. Nötzold, and M. Wolf, *Sampling of broadband terahertz pulses with thick electro-optic crystals*, Applied Physics Letters **90**, 231113 (2007).

[Kar22] O. Karni, E. Barré, V. Pareek, J. D. Georgaras, M. K. L. Man, C. Sahoo, D. R. Bacon, X. Zhu, H. B. Ribeiro, A. L. O'Beirne, J. Hu, A. Al-Mahboob, M. M. M. Abdelrasoul, N. S. Chan, A. Karmakar, A. J. Winchester, B. Kim,

K. Watanabe, T. Taniguchi, K. Barmak, J. Madéo, F. H. da Jornada, T. F. Heinz, and K. M. Dani, *Structure of the moiré exciton captured by imaging its electron and hole*, Nature **603**, 247–252 (2022).

[Kei16] S. Keiber, S. Sederberg, A. Schwarz, M. Trubetskov, V. Pervak, F. Krausz, and N. Karpowicz, *Electro-optic sampling of near-infrared waveforms*, Nature Photonics **10**, 159–162 (2016).

[Kel65] L. Keldysh, *Ionization in the Field of a Strong Electromagnetic Wave*, Soviet Physics JETP **20**, 1307–1314 (1965).

[Ken21] D. M. Kennes, M. Claassen, L. Xian, A. Georges, A. J. Millis, J. Hone, C. R. Dean, D. N. Basov, A. N. Pasupathy, and A. Rubio, *Moiré heterostructures as a condensed-matter quantum simulator*, Nature Physics **17**, 155–163 (2021).

[Kie04] R. Kienberger, E. Goulielmakis, M. Uiberacker, A. Baltuska, V. Yakovlev, F. Bammer, A. Scrinzi, T. Westerwalbesloh, U. Kleineberg, U. Heinzmann, M. Drescher, and F. Krausz, *Atomic transient recorder*, Nature **427**, 817–821 (2004).

[Kim22] R. H. J. Kim, Z. Liu, C. Huang, J.-M. Park, S. J. Haeuser, Z. Song, Y. Yan, Y. Yao, L. Luo, and J. Wang, *Terahertz Nanoimaging of Perovskite Solar Cell Materials*, ACS Photonics **9**, 3550–3556 (2022).

[Kim23] R. H. J. Kim, J.-M. Park, S. J. Haeuser, L. Luo, and J. Wang, *A sub-2 Kelvin cryogenic magneto-terahertz scattering-type scanning near-field optical microscope (cm-THz-sSNOM)*, Review of Scientific Instruments **94**, 043702 (2023).

[Kir25] M. Kira and R. Huber, *Unlocking Lightwave Electronics*, Optics and Photonics News **36**, 28–37 (2025).

[Kno99] B. Knoll and F. Keilmann, *Near-field probing of vibrational absorption for chemical microscopy*, Nature **399**, 134–137 (1999).

[Kno00] B. Knoll and F. Keilmann, *Enhanced dielectric contrast in scattering-type scanning near-field optical microscopy*, Optics Communications **182**, 321–328 (2000).

[Kno18] M. Knorr, P. Steinleitner, J. Raab, I. Gronwald, P. Merkl, C. Lange, and R. Huber, *Ultrabroadband etalon-free detection of infrared transients by van-der-Waals contacted sub-10-μm GaSe detectors*, Optics Express **26**, 19059–19066 (2018).

[Kra09] F. Krausz and M. Ivanov, *Attosecond physics*, Reviews of Modern Physics **81**, 163–234 (2009).

[Küb04] C. Kübler, R. Huber, S. Tübel, and A. Leitenstorfer, *Ultrabroadband detection of multi-terahertz field transients with GaSe electro-optic sensors: Approaching the near infrared*, Applied Physics Letters **85**, 3360–3362 (2004).

[Kul03] M. Kulawik, M. Nowicki, G. Thielsch, L. Cramer, H.-P. Rust, H.-J. Freund, T. P. Pearl, and P. S. Weiss, *A double lamellae dropoff etching procedure for tungsten tips attached to tuning fork atomic force microscopy/scanning tunneling microscopy sensors*, Review of Scientific Instruments **74**, 1027–1030 (2003).

[Lan16] F. Langer, M. Hohenleutner, C. P. Schmid, C. Poellmann, P. Nagler, T. Korn, C. Schüller, M. S. Sherwin, U. Huttner, J. T. Steiner, S. W. Koch, M. Kira, and R. Huber, *Lightwave-driven quasiparticle collisions on a subcycle timescale*, Nature **533**, 225–229 (2016).

[Lei23] A. Leitenstorfer, A. S. Moskalenko, T. Kampfrath, J. Kono, E. Castro-Camus, K. Peng, N. Qureshi, D. Turchinovich, K. Tanaka, A. G. Markelz, M. Havenith, C. Hough, H. J. Joyce, W. J. Padilla, B. Zhou, K.-Y. Kim, X.-C. Zhang, P. U. Jepsen, S. Dhillon, M. Vitiello, E. Linfield, A. G. Davies, M. C. Hoffmann, R. Lewis, M. Tonouchi, P. Klarskov, T. S. Seifert, Y. A. Gerasimenko, D. Mihailovic, R. Huber, J. L. Boland, O. Mitrofanov, P. Dean, B. N. Ellison, P. G. Huggard, S. P. Rea, C. Walker, D. T. Leisawitz, J. R. Gao, C. Li, Q. Chen, G. Valušis, V. P. Wallace, E. Pickwell-MacPherson, X. Shang, J. Hesler, N. Ridler, C. C. Renaud, I. Kallfass, T. Nagatsuma,

J. A. Zeitler, D. Arnone, M. B. Johnston, and J. Cunningham, *The 2023 terahertz science and technology roadmap*, Journal of Physics D: Applied Physics **56**, 223001 (2023).

[Lew84] A. Lewis, M. Isaacson, A. Harootunian, and A. Muray, *Development of a 500 Å spatial resolution light microscope*, Ultramicroscopy **13**, 227–231 (1984).

[L'h07a] J. L'huillier, G. Torosyan, M. Theuer, Y. Avetisyan, and R. Beigang, *Generation of THz radiation using bulk, periodically and aperiodically poled lithium niobate – Part 1: Theory*, Applied Physics B **86**, 185–196 (2007).

[L'h07b] J. L'huillier, G. Torosyan, M. Theuer, C. Rau, Y. Avetisyan, and R. Beigang, *Generation of THz radiation using bulk, periodically and aperiodically poled lithium niobate – Part 2: Experiments*, Applied Physics B **86**, 197–208 (2007).

[LH21] J. Lloyd-Hughes, P. M. Oppeneer, T. Pereira dos Santos, A. Schleife, S. Meng, M. A. Sentef, M. Ruggenthaler, A. Rubio, I. Radu, M. Murnane, X. Shi, H. Kapteyn, B. Stadtmüller, K. M. Dani, F. H. da Jornada, E. Prinz, M. Aeschlimann, R. L. Milot, M. Burdanova, J. Boland, T. Cocker, and F. Hegmann, *The 2021 ultrafast spectroscopic probes of condensed matter roadmap*, Journal of Physics: Condensed Matter **33**, 353001 (2021).

[Lil07] P. Liljeroth, J. Repp, and G. Meyer, *Current-Induced Hydrogen Tautomerization and Conductance Switching of Naphthalocyanine Molecules*, Science **317**, 1203–1206 (2007).

[Lun17] M. B. Lundeberg, Y. Gao, R. Asgari, C. Tan, B. V. Duppen, M. Autore, P. Alonso-González, A. Woessner, K. Watanabe, T. Taniguchi, R. Hillenbrand, J. Hone, M. Polini, and F. H. Koppens, *Tuning quantum nonlocal effects in graphene plasmonics*, Science **357**, 187–191 (2017).

[Luo20] Y. Luo, V. Jelic, G. Chen, P. H. Nguyen, Y. J. R. Liu, J. A. Calzada, D. J. Mildenberger, and F. A. Hegmann, *Nanoscale terahertz STM imaging of a metal surface*, Physical Review B **102**, 205417 (2020).

[Mal23] P. K. Mallick, *Fundamentals of Molecular Spectroscopy*, Springer Nature Singapore Pte Ltd., 2023.

[Man16] C. Manzoni and G. Cerullo, *Design criteria for ultrafast optical parametric amplifiers*, Journal of Optics **18**, 103501 (2016).

[Mei23] E. Meirzadeh, A. M. Evans, M. Rezaee, M. Milich, C. J. Dionne, T. P. Darlington, S. T. Bao, A. K. Bartholomew, T. Handa, D. J. Rizzo, R. A. Wiscons, M. Reza, A. Zangiabadi, N. Fardian-Melamed, A. C. Crowther, P. J. Schuck, D. N. Basov, X. Zhu, A. Giri, P. E. Hopkins, P. Kim, M. L. Steigerwald, J. Yang, C. Nuckolls, and X. Roy, *A few-layer covalent network of fullerenes*, Nature **613**, 71–76 (2023).

[Mei24] C. Meineke, J. Schlosser, M. Zizlsperger, M. Liebich, N. Nilforoushan, K. Mosina, S. Terres, A. Chernikov, Z. Sofer, M. A. Huber, M. Florian, M. Kira, F. Dirnberger, and R. Huber, *Ultrafast Exciton Dynamics in the Atomically Thin van der Waals Magnet CrSBr*, Nano Letters **24**, 4101–4107 (2024).

[Mey20] F. Meyer, T. Vogel, S. Ahmed, and C. J. Saraceno, *Single-cycle, MHz repetition rate THz source with 66 mW of average power*, Optics Letters **45**, 2494–2497 (2020).

[Moo12] K. Moon, Y. Do, M. Lim, G. Lee, H. Kang, K.-S. Park, and H. Han, *Quantitative coherent scattering spectra in apertureless terahertz pulse near-field microscopes*, Applied Physics Letters **101**, 011109 (2012).

[Moo20] F. Mooshammer, M. A. Huber, F. Sandner, M. Plankl, M. Zizlsperger, and R. Huber, *Quantifying Nanoscale Electromagnetic Fields in Near-Field Microscopy by Fourier Demodulation Analysis*, ACS Photonics **7**, 344–351 (2020).

[Mül20] M. Müller, N. Martín Sabanés, T. Kampfrath, and M. Wolf, *Phase-Resolved Detection of Ultrabroadband THz Pulses inside a Scanning Tunneling Microscope Junction*, ACS Photonics **7**, 2046–2055 (2020).

[Muy29] E. Muybridge, *Classics of Science: Muybridge on Attitudes of Animals*, The Science News-Letter **16**, 183–184 (1929).

[Neg11] J.-P. Negel, R. Hegenbarth, A. Steinmann, B. Metzger, F. Hoos, and H. Giessen, *Compact and cost-effective scheme for THz generation via optical rectification in GaP and GaAs using novel fs laser oscillators*, Applied Physics B **103**, 45–50 (2011).

[Ni16] G. X. Ni, L. Wang, M. D. Goldflam, M. Wagner, Z. Fei, A. S. McLeod, M. K. Liu, F. Keilmann, B. Özyilmaz, A. H. Castro Neto, J. Hone, M. M. Fogler, and D. N. Basov, *Ultrafast optical switching of infrared plasmon polaritons in high-mobility graphene*, Nature Photonics **10**, 244–247 (2016).

[Nil14] J. Nillon, O. Crégut, C. Bressler, and S. Haacke, *Two MHz tunable non collinear optical parametric amplifiers with pulse durations down to 6 fs*, Optics Express **22**, 14964–14974 (2014).

[Nov12] L. Novotny and B. Hecht, *Principles of Nano-Optics*, 2nd ed., Cambridge University Press, 2012.

[Noz58] P. Nozières and D. Pines, *Electron Interaction in Solids. General Formulation*, Physical Review **109**, 741–761 (1958).

[Oce06] N. Ocelic, A. Huber, and R. Hillenbrand, *Pseudoheterodyne detection for background-free near-field spectroscopy*, Applied Physics Letters **89**, 101124 (2006).

[Ord87] M. A. Ordal, R. J. Bell, R. W. Alexander, L. L. Long, and M. R. Querry, *Optical properties of Au, Ni, and Pb at submillimeter wavelengths*, Applied Optics **26**, 744–752 (1987).

[Ord88] M. A. Ordal, R. J. Bell, R. W. Alexander, L. A. Newquist, and M. R. Querry, *Optical properties of Al, Fe, Ti, Ta, W, and Mo at submillimeter wavelengths*, Applied Optics **27**, 1203–1209 (1988).

[Pál04] L. Pálfalvi, J. Hebling, G. Almási, Á. Péter, K. Polgár, K. Lengyel, and R. Szipöcs, *Nonlinear refraction and absorption of Mg doped stoichiometric and congruent $LiNbO_3$*, Journal of Applied Physics **95**, 902–908 (2004).

[Pál05] L. Pálfalvi, J. Hebling, J. Kuhl, Á. Péter, and K. Polgár, *Temperature dependence of the absorption and refraction of Mg-doped congruent and stoichiometric $LiNbO_3$ in the THz range*, Journal of Applied Physics **97**, 123505 (2005).

[Pat19] L. L. Patera, F. Queck, P. Scheuerer, and J. Repp, *Mapping orbital changes upon electron transfer with tunnelling microscopy on insulators*, Nature **566**, 245–248 (2019).

[Pel20] D. Peller, L. Z. Kastner, T. Buchner, C. Roelcke, F. Albrecht, N. Moll, R. Huber, and J. Repp, *Sub-cycle atomic-scale forces coherently control a single-molecule switch*, Nature **585**, 58–62 (2020).

[Pel21] D. Peller, C. Roelcke, L. Z. Kastner, T. Buchner, A. Neef, J. Hayes, F. Bonafé, D. Sidler, M. Ruggenthaler, A. Rubio, R. Huber, and J. Repp, *Quantitative sampling of atomic-scale electromagnetic waveforms*, Nature Photonics **15**, 143–147 (2021).

[Pla21] M. Plankl, P. E. Faria Junior, F. Mooshammer, T. Siday, M. Zizlsperger, F. Sandner, F. Schiegl, S. Maier, M. A. Huber, M. Gmitra, J. Fabian, J. L. Boland, T. L. Cocker, and R. Huber, *Subcycle contact-free nanoscopy of ultrafast interlayer transport in atomically thin heterostructures*, Nature Photonics **15**, 594–600 (2021).

[Poh84] D. W. Pohl, W. Denk, and M. Lanz, *Optical stethoscopy: Image recording with resolution $\lambda/20$*, Applied Physics Letters **44**, 651–653 (1984).

[Por14] M. Porer, U. Leierseder, J.-M. Ménard, H. Dachraoui, L. Mouchliadis, I. E. Perakis, U. Heinzmann, J. Demsar, K. Rossnagel, and R. Huber, *Non-thermal separation of electronic and structural orders in a persisting charge density wave*, Nature Materials **13**, 857–861 (2014).

[Qaz07] M. M. Qazilbash, M. Brehm, B.-G. Chae, P.-C. Ho, G. O. Andreev, B.-J. Kim, S. J. Yun, A. V. Balatsky, M. B. Maple, F. Keilmann, H.-T. Kim, and D. N. Basov, *Mott Transition in $VO_2$ Revealed by Infrared Spectroscopy and Nano-Imaging*, Science **318**, 1750–1753 (2007).

[Rei18] J. Reimann, S. Schlauderer, C. P. Schmid, F. Langer, S. Baierl, K. A. Kokh, O. E. Tereshchenko, A. Kimura, C. Lange, J. Güdde, U. Höfer, and R. Huber, *Subcycle observation of lightwave-driven Dirac currents in a topological surface band*, Nature **562**, 396–400 (2018).

[Rep05] J. Repp, G. Meyer, S. M. Stojković, A. Gourdon, and C. Joachim, *Molecules on Insulating Films: Scanning-Tunneling Microscopy Imaging of Individual Molecular Orbitals*, Physical Review Letters **94**, 026803 (2005).

[Rid22] E. Ridente, M. Mamaikin, N. Altwaijry, D. Zimin, M. F. Kling, V. Pervak, M. Weidman, F. Krausz, and N. Karpowicz, *Electro-optic characterization of synthesized infrared-visible light fields*, Nature Communications **13**, 1111 (2022).

[Rie00] E. Riedle, M. Beutter, S. Lochbrunner, J. Piel, S. Schenkl, S. Spörlein, and W. Zinth, *Generation of 10 to 50 fs pulses tunable through all of the visible and the NIR*, Applied Physics B: Lasers and Optics **71**, 457–465 (2000).

[Rie15] C. Riek, D. V. Seletskiy, A. S. Moskalenko, J. F. Schmidt, P. Krauspe, S. Eckart, S. Eggert, G. Burkard, and A. Leitenstorfer, *Direct sampling of electric-field vacuum fluctuations*, Science **350**, 420–423 (2015).

[Roe24] C. Roelcke, L. Z. Kastner, M. Graml, A. Biereder, J. Wilhelm, J. Repp, R. Huber, and Y. A. Gerasimenko, *Ultrafast atomic-scale scanning tunnelling spectroscopy of a single vacancy in a monolayer crystal*, Nature Photonics **18**, 595–602 (2024).

[Ron18] Y. Rong, Y. Hu, A. Mei, H. Tan, M. I. Saidaminov, S. I. Seok, M. D. McGehee, E. H. Sargent, and H. Han, *Challenges for commercializing perovskite solar cells*, Science **361**, eaat8235 (2018).

[Sai19] U. S. Sainadh, H. Xu, X. Wang, A. Atia-Tul-Noor, W. C. Wallace, N. Douguet, A. Bray, I. Ivanov, K. Bartschat, A. Kheifets, R. T. Sang, and I. V. Litvinyuk, *Attosecond angular streaking and tunnelling time in atomic hydrogen*, Nature **568**, 75–77 (2019).

[Sal07] B. E. A. Saleh and M. C. Teich, *Fundamentals of Photonics*, 2nd ed., John Wiley & Sons, Inc., 2007.

[Sch07] D. N. Schimpf, J. Rothhardt, J. Limpert, A. Tünnermann, and D. C. Hanna, *Theoretical analysis of the gain bandwidth for noncollinear parametric amplification of ultrafast pulses*, Journal of the Optical Society of America B **24**, 2837–2846 (2007).

[Sch14] O. Schubert, M. Hohenleutner, F. Langer, B. Urbanek, C. Lange, U. Huttner, D. Golde, T. Meier, M. Kira, S. W. Koch, and R. Huber, *Sub-cycle control of terahertz high-harmonic generation by dynamical Bloch oscillations*, Nature Photonics **8**, 119–123 (2014).

[Sch17] Z. Schumacher, A. Spielhofer, Y. Miyahara, and P. Grutter, *The limit of time resolution in frequency modulation atomic force microscopy by a pump-probe approach*, Applied Physics Letters **110**, 053111 (2017).

[Sch21] C. P. Schmid, L. Weigl, P. Grössing, V. Junk, C. Gorini, S. Schlauderer, S. Ito, M. Meierhofer, N. Hofmann, D. Afanasiev, J. Crewse, K. A. Kokh, O. E. Tereshchenko, J. Güdde, F. Evers, J. Wilhelm, K. Richter, U. Höfer, and R. Huber, *Tunable non-integer high-harmonic generation in a topological insulator*, Nature **593**, 385–390 (2021).

[Sch22] D. Schmitt, J. P. Bange, W. Bennecke, A. AlMutairi, G. Meneghini, K. Watanabe, T. Taniguchi, D. Steil, D. R. Luke, R. T. Weitz, S. Steil, G. S. M. Jansen, S. Brem, E. Malic, S. Hofmann, M. Reutzel, and S. Mathias, *Formation of moiré interlayer excitons in space and time*, Nature **608**, 499–503 (2022).

[Sel08] A. Sell, A. Leitenstorfer, and R. Huber, *Phase-locked generation and field-resolved detection of widely tunable terahertz pulses with amplitudes exceeding 100 MV/cm*, Optics Letters **33**, 2767–2769 (2008).

[Sha12] D. Shafir, H. Soifer, B. D. Bruner, M. Dagan, Y. Mairesse, S. Patchkovskii, M. Y. Ivanov, O. Smirnova, and N. Dudovich, *Resolving the time when an electron exits a tunnelling barrier*, Nature **485**, 343–346 (2012).

[Sid22] T. Siday, F. Sandner, S. Brem, M. Zizlsperger, R. Perea-Causin, F. Schiegl, S. Nerreter, M. Plankl, P. Merkl, F. Mooshammer, M. A. Huber, E. Malic, and R. Huber, *Ultrafast Nanoscopy of High-Density Exciton Phases in $WSe_2$*, Nano Letters **22**, 2561–2568 (2022).

[Sid24] T. Siday, J. Hayes, F. Schiegl, F. Sandner, P. Menden, V. Bergbauer, M. Zizlsperger, S. Nerreter, S. Lingl, J. Repp, J. Wilhelm, M. A. Huber, Y. A. Gerasimenko, and R. Huber, *All-optical subcycle microscopy on atomic length scales*, Nature **629**, 329–334 (2024).

[Ste03] A. G. Stepanov, J. Hebling, and J. Kuhl, *Efficient generation of subpicosecond terahertz radiation by phase-matched optical rectification using ultrashort laser pulses with tilted pulse fronts*, Applied Physics Letters **83**, 3000–3002 (2003).

[Ste05] A. G. Stepanov, J. Hebling, and J. Kuhl, *THz generation via optical rectification with ultrashort laser pulse focused to a line*, Applied Physics B: Lasers and Optics **81**, 23–26 (2005).

[Ste21] A. J. Sternbach, S. H. Chae, S. Latini, A. A. Rikhter, Y. Shao, B. Li, D. Rhodes, B. Kim, P. J. Schuck, X. Xu, X.-Y. Zhu, R. D. Averitt, J. Hone, M. M. Fogler, A. Rubio, and D. N. Basov, *Programmable hyperbolic polaritons in van der Waals semiconductors*, Science **371**, 617–620 (2021).

[Sti98] B. C. Stipe, M. A. Rezaei, and W. Ho, *Single-Molecule Vibrational Spectroscopy and Microscopy*, Science **280**, 1732–1735 (1998).

[Sti18] H. T. Stinson, A. Sternbach, O. Najera, R. Jing, A. S. Mcleod, T. V. Slusar, A. Mueller, L. Anderegg, H. T. Kim, M. Rozenberg, and D. N. Basov, *Imaging the nanoscale phase separation in vanadium dioxide thin films at terahertz frequencies*, Nature Communications **9**, 3604 (2018).

[Sun18] S. S. Sunku, G. X. Ni, B. Y. Jiang, H. Yoo, A. Sternbach, A. S. McLeod, T. Stauber, L. Xiong, T. Taniguchi, K. Watanabe, P. Kim, M. M. Fogler, and D. N. Basov, *Photonic crystals for nano-light in moiré graphene superlattices*, Science **362**, 1153–1156 (2018).

[Syn28] E. Synge, *XXXVIII. A suggested method for extending microscopic resolution into the ultra-microscopic region*, The London, Edinburgh, and Dublin Philosophical Magazine and Journal of Science **6**, 356–362 (1928).

[Tak02] O. Takeuchi, R. Morita, M. Yamashita, and H. Shigekawa, *Development of Time-Resolved Scanning Tunneling Microscopy in Femtosecond Range*, Japanese Journal of Applied Physics **41**, 4994–4997 (2002).

[Tak05] O. Takeuchi, M. Aoyama, and H. Shigekawa, *Analysis of Time-Resolved Tunnel Current Signal in Sub-Picosecond Range Observed by Shaken-Pulse-Pair-Excited Scanning Tunneling Miscroscopy*, Japanese Journal of Applied Physics **44**, 5354–5357 (2005).

[Tót23] G. Tóth, G. Polónyi, and J. Hebling, *Tilted pulse front pumping techniques for efficient terahertz pulse generation*, Light: Science & Applications **12**, 256 (2023).

[Tra19] K. Tran, G. Moody, F. Wu, X. Lu, J. Choi, K. Kim, A. Rai, D. A. Sanchez, J. Quan, A. Singh, J. Embley, A. Zepeda, M. Campbell, T. Autry, T. Taniguchi, K. Watanabe, N. Lu, S. K. Banerjee, K. L. Silverman, S. Kim, E. Tutuc, L. Yang, A. H. MacDonald, and X. Li, *Evidence for moiré excitons in van der Waals heterostructures*, Nature **567**, 71–75 (2019).

[Ulb11] R. Ulbricht, E. Hendry, J. Shan, T. F. Heinz, and M. Bonn, *Carrier dynamics in semiconductors studied with time-resolved terahertz spectroscopy*, Reviews of Modern Physics **83**, 543–586 (2011).

[Van12] G. Van Tendeloo, S. Bals, S. Van Aert, J. Verbeeck, and D. Van Dyck, *Advanced Electron Microscopy for Advanced Materials*, Advanced Materials **24**, 5655–5675 (2012).

[Wag14] M. Wagner, Z. Fei, A. S. McLeod, A. S. Rodin, W. Bao, E. G. Iwinski, Z. Zhao, M. Goldflam, M. Liu, G. Dominguez, M. Thiemens, M. M. Fogler, A. H. Castro Neto, C. N. Lau, S. Amarie, F. Keilmann, and D. N. Basov, *Ultrafast and Nanoscale Plasmonic Phenomena in Exfoliated Graphene Revealed by Infrared Pump–Probe Nanoscopy*, Nano Letters **14**, 894–900 (2014).

[Wan18] G. Wang, A. Chernikov, M. M. Glazov, T. F. Heinz, X. Marie, T. Amand, and B. Urbaszek, *Colloquium: Excitons in atomically thin transition metal dichalcogenides*, Reviews of Modern Physics **90**, 021001 (2018).

[Wan22] L. Wang, Y. Xia, and W. Ho, *Atomic-scale quantum sensing based on the ultrafast coherence of an $H_2$ molecule in an STM cavity*, Science **376**, 401–405 (2022).

[Wim14] L. Wimmer, G. Herink, D. R. Solli, S. V. Yalunin, K. E. Echternkamp, and C. Ropers, *Terahertz control of nanotip photoemission*, Nature Physics **10**, 432–436 (2014).

[Wu95] Q. Wu and X.-C. Zhang, *Free-space electro-optic sampling of terahertz beams*, Applied Physics Letters **67**, 3523–3525 (1995).

[Xia21] L. Xian, M. Claassen, D. Kiese, M. M. Scherer, S. Trebst, D. M. Kennes, and A. Rubio, *Realization of nearly dispersionless bands with strong orbital anisotropy from destructive interference in twisted bilayer $MoS_2$*, Nature Communications **12**, 5644 (2021).

[Xu22] Q. Xu, Y. Guo, and L. Xian, *Moiré flat bands in twisted 2D hexagonal vdW materials*, 2D Materials **9**, 014005 (2022).

[Yos21] S. Yoshida, Y. Arashida, H. Hirori, T. Tachizaki, A. Taninaka, H. Ueno, O. Takeuchi, and H. Shigekawa, *Terahertz Scanning Tunneling Microscopy for Visualizing Ultrafast Electron Motion in Nanoscale Potential Variations*, ACS Photonics **8**, 315–323 (2021).

[Yu17] H. Yu, G.-B. Liu, J. Tang, X. Xu, and W. Yao, *Moiré excitons: From programmable quantum emitter arrays to spin-orbit–coupled artificial lattices*, Science Advances **3**, e1701696 (2017).

[Zen95] F. Zenhausern, Y. Martin, and H. K. Wickramasinghe, *Scanning Interferometric Apertureless Microscopy: Optical Imaging at 10 Angstrom Resolution*, Science **269**, 1083–1085 (1995).

[Zew00] A. H. Zewail, *Femtochemistry: Atomic-Scale Dynamics of the Chemical Bond*, The Journal of Physical Chemistry A **104**, 5660–5694 (2000).

[Zha21a] Q. Zhang, G. Hu, W. Ma, P. Li, A. Krasnok, R. Hillenbrand, A. Alù, and C. W. Qiu, *Interface nano-optics with van der Waals polaritons*, Nature **597**, 187–195 (2021).

[Zha21b] W. Zhao, S. Zhao, H. Li, S. Wang, S. Wang, M. I. B. Utama, S. Kahn, Y. Jiang, X. Xiao, S. J. Yoo, K. Watanabe, T. Taniguchi, A. Zettl, and F. Wang, *Efficient Fizeau drag from Dirac electrons in monolayer graphene*, Nature **594**, 517–521 (2021).

[Zha25] Z. Zhao, V. Kravtsov, Z. Wang, Z. Zhou, L. Dou, D. Huang, Z. Wang, X. Cheng, M. B. Raschke, and T. Jiang, *Applications of ultrafast nano-spectroscopy and nano-imaging with tip-based microscopy*, eLight **5**, 1 (2025).

[Zho21] Y. Zhou, J. Sung, E. Brutschea, I. Esterlis, Y. Wang, G. Scuri, R. J. Gelly, H. Heo, T. Taniguchi, K. Watanabe, G. Zaránd, M. D. Lukin, P. Kim, E. Demler, and H. Park, *Bilayer Wigner crystals in a transition metal dichalcogenide heterostructure*, Nature **595**, 48–52 (2021).

[Ziz24] M. Zizlsperger, S. Nerreter, Q. Yuan, K. B. Lohmann, F. Sandner, F. Schiegl, C. Meineke, Y. A. Gerasimenko, L. M. Herz, T. Siday, M. A. Huber, M. B. Johnston, and R. Huber, *In situ nanoscopy of single-grain nanomorphology and ultrafast carrier dynamics in metal halide perovskites*, Nature Photonics **18**, 975–981 (2024).

[Zuo16] C. Zuo, H. J. Bolink, H. Han, J. Huang, D. Cahen, and L. Ding, *Advances in Perovskite Solar Cells*, Advanced Science **3**, 1500324 (2016).

# Acknowledgements

Completing a PhD is a challenging and rewarding journey, and I am deeply grateful to those who have supported me along the way. Science is never a solitary endeavour, and this work would not have been possible without the guidance, collaboration, and encouragement of many people. I would like to take this opportunity to express my heartfelt thanks to everyone who has contributed to this thesis, both professionally and personally.

I would like to sincerely thank my supervisor, **Rupert Huber**, for his guidance and support throughout my PhD. A phrase he often repeats – and that has stuck with me ever since – is: "Science is a team sport." Rupert has managed to build and lead an absolutely magnificent team that embodies this sentiment. His curiosity and deep fascination with science are truly inspiring. I am immensely grateful for the trust Rupert placed in me, teaching me grit and determination and always encouraging me to push forward, even when things seemed impossible. His ability to explain complex physical concepts in an intuitive and accessible way has helped me see physics from new perspectives. I also deeply appreciate the opportunities he gave me to share our work with the scientific community.

Throughout my Master's and PhD journey, I have always enjoyed fruitful discussions with **Jascha Repp**, whose input has been greatly appreciated. I am particularly thankful for the time he invested in reviewing my thesis, as well as for the continued interest he has shown in my work.

I would also like to express my sincere gratitude to the entire board of examiners — **Prof. Dr. Vladimir Braun**, **Prof. Dr. Rupert Huber**, **Prof. Dr. Jascha Repp**, and **Prof. Dr. Ulrich Höfer** — for taking the time to evaluate my work and for conducting the oral examination.

I am also thankful to **Jan Wilhelm** for our successful collaboration. I am excited to see what new avenues his theoretical efforts, combined with our experiments, will open.

Throughout my PhD, I had the privilege of closely working with and learning from more experienced scientists. **Thomas Siday** is an incredibly driven personality – his deep, intuitive understanding of physics make him a brilliant teacher. I would also like to acknowledge **Yaroslav Gerasimenko**, whose remarkable breadth of knowledge – especially on everything materials science or scanning probe microscopy – never ceased to impress me. A special thanks to **Markus Huber** for his wise insights and for setting new standards in Blender-rendered conference slides.

Throughout my scientific career, I have had the pleasure of learning from my predecessors, who turned into friends. **Christian Meineke** has been by my side since my Bachelor's project, teaching me everything from basic lab skills to navigating the jungle of science. From the start of my Master's project, **Lukas Kastner** also took me under his wing – I admire his work ethic and his genuinely positive, welcoming nature. **Carmen Roelcke**, though only a couple of years senior to me, always had wise advice. **Dominik Peller** made me feel like an important part of the team even when I had just started. **Simon Maier**, who was never officially supervising me, was always around the gang. I truly cherish the personal connections I made with all of you. I sincerely hope we will stay in touch.

Working closely with the other cryoSNOM PhD students has been an incredibly rewarding experience. I want to thank **Fabian Sandner** for his enthusiastic introduction to the low-temperature scanning probe microscope and all the groundwork he has done, which laid a solid foundation for much of our work. For the majority of my PhD, I was fortunate to work closely with **Felix Schiegl**, whose support,

friendship, and shared dedication not only had a significant impact on my research but also made our time in the lab and office truly enjoyable. Last year, **Svenja Nerreter** also joined our team, and she has been an amazing addition to the group, bringing new energy, insight and a lot of laughter.

I had the pleasure of supervising several young scientists in the early stages of their careers. **Peter Menden** was the first student I mentored during his bachelor's project, and I learned a lot from answering his insightful questions. As a master's student, he proved to be an exceptionally skilled and valuable team member. **Sonja Lingl** took on the demanding challenge of managing her own project during her master's degree – something she mastered impressively. It was a privilege to support her and witness her growth. **Valentin Bergbauer**, seamlessly integrated into the team during the busiest phase of my PhD. Though still early in his career, he contributed with the confidence and skill of a much more senior scientist.

Our group would not be as successful without the incredible permanent staff and their invaluable expertise and dedication. Every waveform in this thesis owes its existence to **Ignaz Laepple**'s exceptional electrical engineering expertise. **Martin Furthmeier** was always ready to assist with mechanical components, from designing stage adapters to building complex cryostats. We are fortunate to now have **Matthias Heinl** as Martin's successor, who approaches every challenge with a smile on his face. Not a single tip would have been fabricated if we didn't have **Imke Gronwald** keeping us safe. And keeping everything running in the background: **Ulla Franzke**, who made sure everything ran smoothly, handling the many administrative challenges that came our way, allowing us to focus on our research. Thank you all for your dedication and support!

A sincere thanks goes out to **Josef Freudenstein** & **Josef Riepl**. I can't believe how long we have been friends – meeting you at the very start of our university journey and now finishing our PhDs together. I am so grateful for all the fun we had and the memories we made along the way.

I am also grateful for the fun breaks and scientific discussions with the **Chemistry Gang** – often valuable, always entertaining!

Of course, my gratitude extends to the entire **Huber group**. Working in an environment filled with like-minded, passionate scientists who support each other has been an absolute pleasure. I know that such a dynamic and collaborative group is rare, and I am deeply grateful for the time I spent with all of you.

I would also like to thank **Felix Schiegl**, **Valentin Bergbauer**, **Peter Menden** and **Yaroslav Gerasimenko** for proofreading my thesis.

I also want to thank **my parents**, without whom I would never be where I am today, for their continuous support.

Finally, I want to thank my wife **Lena**. Without her, I would never have mastered the ups and downs of a PhD. She is the constant in my life that I can always depend on, and gives me the steadiness to take on whatever life throws at me. This journey would not have been the same without you.